

ABSTRACT

Title of Dissertation: UNDERSTANDING THE EFFECT OF
FABRICATION CONDITIONS ON THE
STRUCTURAL, ELECTRICAL, AND
MECHANICAL PROPERTIES OF
COMPOSITE MATERIALS
CONTAINING CARBON FILLERS

Madeline Antonia Morales,
Doctor of Philosophy, 2022

Dissertation directed by: Professor Lourdes G. Salamanca-Riba,
Department of Materials Science and
Engineering

Carbon structures are commonly used as the reinforcement phase in composite materials to improve the electrical, mechanical, and/or thermal properties of the matrix material. The structural diversity of carbon in its various forms (graphene, carbon nanotubes, graphite fibers, for example) makes it a useful reinforcement phase, as the properties of the composite material can be tailored for a specific application depending on the structure and properties of the carbon structure used. In this work, the incorporation of graphene/graphitic carbon into an aluminum metal matrix by an electrocharging assisted process (EAP) was investigated to create a composite material with enhanced electrical conductivity and yield strength. The increased electrical conductivity makes the composite suitable for application in more efficient power transmission lines. The increased strength makes it useful as a lightweight structural material in aerospace applications. The EAP involves applying a direct current to a mixture of molten

aluminum and activated carbon to induce the crystallization of graphitic sheets/ribbons that extend throughout the matrix. The effect of processing conditions (current density, in particular) on the graphitic carbon structure, electrical properties, and mechanical properties of the composite material was investigated. The effect of porosity/voids and oxide formation was discussed with respect to the measured properties, and updates to the EAP system were made to mitigate their detrimental effects. It was found that the application of current results in some increase in graphitic carbon crystallite size calculated from Raman spectra, but many areas show the same crystallite size as the activated carbon starting material. It is likely that the current density used during processing was too low to see significant crystallization of graphitic carbon. There was no increase in electrical conductivity compared to a baseline sample with no added carbon, most likely due to porosity/voids in the samples. The mechanical characterization results indicated that the graphitic carbon clusters formed by the process did not act as an effective reinforcement phase, with no improvement in hardness and a decrease in elastic modulus measured by nanoindentation. The decreased elastic modulus was a result of compliant carbon clusters and porosity in the covetic samples. The porosity/voids were not entirely eliminated by the updates to the system, thus the electrical conductivity still did not improve.

Additionally, a multifunctional composite structure consisting of a carbon-fiber reinforced polymer (CFRP) laminate with added copper mesh layers was investigated for use in aerospace applications as a structural and electromagnetic interference (EMI) shielding component. The CFRP provides primarily a structural function, while the copper mesh layers were added to increase EMI shielding effectiveness (SE). Nanoindentation was used to study the interfacial mechanical properties of the fiber/polymer and Cu/polymer interfaces, as the interfacial strength dictates the overall mechanical performance of the composite. Further, a finite element model of

EMI SE was made to predict SE in the radiofrequency to microwave range for different geometry and configurations of the multifunctional composite structure. The model was used to help determine the optimum design of the multifunctional composite structure for effective shielding of EM radiation. It was found from nanoindentation near the fiber/polymer and Cu/polymer interfaces that the carbon fibers act as an effective reinforcement phase with hardness in the matrix increasing in the interphase region near the carbon fibers due to strong interfacial adhesion. In contrast, the Cu/polymer interface did not exhibit an increase in hardness, indicating poor interfacial adhesion. The EMI SE model indicated that the combination of CFRP layers, which primarily shields EMI by absorption, and Cu mesh, which predominantly shields by reflection, provided adequate SE over a wider frequency range than the individual components alone. Further, it was found that the SE of the CFRP layers were improved by including multiple plies with different relative fiber orientations.

UNDERSTANDING THE EFFECT OF FABRICATION CONDITIONS ON THE
STRUCTURAL, ELECTRICAL, AND MECHANICAL PROPERTIES OF
COMPOSITE MATERIALS CONTAINING CARBON FILLERS

by

Madeline Antonia Morales

Dissertation submitted to the Faculty of the Graduate School of the
University of Maryland, College Park, in partial fulfillment
of the requirements for the degree of
Doctor of Philosophy
2022

Advisory Committee:
Professor Lourdes G. Salamanca-Riba, Chair
Dr. Todd C. Henry
Professor Oded Rabin
Professor Taylor Woehl
Professor You Zhou

© Copyright by
Madeline Antonia Morales
2022

Acknowledgements

I want to thank my advisor, Professor Lourdes Salamanca-Riba, for her guidance and support during my time in graduate school, both as a research advisor and as a teacher in the classroom. I also want to thank my undergraduate research advisor, Professor Elizabeth Opila, for giving me the opportunity to work in her lab and gain crucial experience while at the University of Virginia. I am grateful for the support of my colleagues at the University of Maryland, Dr. Xiaoxiao Ge and Dr. Christopher Klingshirn. Additionally, I am grateful for the support I received from Dr. Daniel Cole, Dr. Todd Henry, Dr. Christopher Shumeyko, and Dr. Asha Hall at the Army Research Laboratory, and the opportunity to use the nanoindenter and other instruments at the Army Research Laboratory. I am appreciative of the characterization advice from Dr. Jiancun Rao, Dr. Sz-Chian Liou and Dr. Karen Gaskell from the UMD NanoCenter AIMLab and Surface Analysis Center. Finally, I want to acknowledge my funding sources: the Department of Energy under DOE-EERE grant DE-EE0008313 and the Army Research Laboratory under Cooperative Agreement W911NF-19-2-0291.

Table of Contents

Acknowledgements.....	ii
Table of Contents.....	iii
List of Tables.....	vi
List of Figures.....	vii
List of Abbreviations.....	xiii
Chapter 1: Introduction.....	1
1.1. Composite Materials with Carbon Nanostructure Fillers.....	1
1.2. Covetics: in-situ Formation of Graphene-Metal Matrix Composites.....	4
1.3. Characterization Challenges for Covetic Materials.....	7
1.4. Recent Work on 3 wt% AA-1350 and 6061 Covetics Made at the University of Maryland.....	9
1.5. Multifunctional Composite Materials and Structures.....	11
1.6. Mechanical Properties of Multifunctional Composites.....	12
1.7. Electromagnetic Shielding Theory.....	13
1.7.1. Absorption Loss and the Skin Effect.....	14
1.7.2. Reflection Loss to Plane Waves.....	15
1.7.3. Summary.....	16
1.8. Composite Materials for Electromagnetic Shielding.....	16
1.9. Summary of Chapters.....	18
Chapter 2: Experimental Methods and Characterization Techniques.....	19
2.1. Covetic Sample Fabrication.....	19
2.2. Machining Samples for Characterization.....	22
2.3. COMSOL Multiphysics Software.....	24
2.4. Raman Spectroscopy.....	25
2.5. Scanning Electron Microscopy (SEM), Energy Dispersive Spectroscopy (EDS) and Electron Backscatter Diffraction (EBSD).....	25
2.6. Transmission Electron Microscopy (TEM).....	26
2.7. Four Point Probe Electrical Conductivity.....	26
2.8. Nanoindentation and Electrical Contact Resistance.....	27
Chapter 3: Covetics Critical Current Density Investigation.....	29
3.1. Motivation and Objectives.....	29
3.2. Sample Fabrication.....	30
3.3. COMSOL Model of Current Density, Voltage, and Electric Field in the Covetics System.....	32
3.4. Sample Sectioning.....	34
3.5. Raman Spectroscopy.....	36
3.6. Four Point Probe Electrical Conductivity.....	40
3.7. Discussion.....	42
3.7.1. AA-1350 Metallurgy.....	42
3.7.2. Carbon Nanostructure Assembly Process.....	44
3.8. Conclusions and Future Work.....	45

Chapter 4: Micromechanics of AA-1350 3 wt. % C Covetics.....	47
4.1. Motivation and Objectives.....	47
4.2. Description of Covetic Samples and Identification of Regions of Interest (ROI).....	48
4.3. SEM/EDS Analysis of the ROIs.....	49
4.4. Transmission Electron Microscopy.....	50
4.5. Nanoindentation.....	52
4.5.1. Nanoindentation Near Carbon Aggregates Within Grain/Near Void.....	54
4.5.2. Electrical Contact Resistance (ECR).....	56
4.5.3. Nanoindentation Near Carbon at Grain Boundaries.....	58
4.5.4. High-Load Transducer/Stage Around ROIs.....	60
4.6. Discussion.....	67
4.6.1. Contact Area Function: Pile-up and Sink-in Behavior.....	67
4.6.2. Microstructural Strengthening Mechanisms.....	68
4.7. Conclusions and Future Work.....	69
Chapter 5: Updates to the Covetics Processing System.....	71
5.1. Motivation and Objective.....	71
5.2. Updates to the Covetics Processing System and Procedure.....	71
5.2.1. Dehydrate Activated Carbon Starting Material.....	71
5.2.2. Updated Stirring System with Argon Flow.....	72
5.3. Experimental Methods.....	74
5.3.1. Sample Processing Conditions and Sectioning for Characterization.....	74
5.3.2. Raman Spectroscopy, Graphitic Carbon Crystallite Size.....	75
5.3.3. Four Point Probe Electrical Conductivity Measurement.....	75
5.4. Results and Discussion.....	76
5.4.1. Raman Spectroscopy.....	76
5.4.2. Electrical Conductivity.....	76
5.5. Conclusions and Future Work.....	79
Chapter 6: Micromechanics of an IM7/PEEK Laminate with Added Copper Mesh Layers.....	81
6.1. Motivation and Objectives.....	81
6.2. SEM and X-ray CT of CFRP laminate with Cu Mesh.....	82
6.3. Annealing Effects on Raman Spectra of PEEK.....	84
6.4. Nanoindentation Results as a Function of Distance from Fiber/Cu.....	85
6.4.1. Histograms of Nanoindentation Results.....	85
6.4.2. Measurement of Distance from Fiber/Cu Edge from SPM.....	87
6.4.3 Nanoindentation: Comparison of CFRP Interface Region Before and After Annealing.....	89
6.4.4. Nanoindentation: Comparison of CFRP to Copper Interface Region.....	92
6.5. Conclusions and Future Work.....	94
Chapter 7: Model of Electromagnetic Interference Shielding Effectiveness for the Multifunctional Composite Containing CFRP and Copper Mesh Layers.....	96
7.1. Motivation and Objectives.....	96
7.2. Calculation of Shielding Effectiveness from the COMSOL Model.....	97
7.3. Shielding Effectiveness of CFRP Laminate.....	101
7.3.1. Homogenization of Material Properties.....	101
7.3.3. Effect of Material Property Values on Shielding Effectiveness.....	106
7.3.4. Effect of Ply Thickness on Shielding Effectiveness.....	106

7.3.5. Effect of Fiber Orientation on Shielding Effectiveness	108
7.3.6. Effect of Fiber Orientation on Shielding Effectiveness	111
7.4. Shielding Effectiveness of Cu Mesh.....	112
7.4.1. Analytical Sheet Impedance Expression.....	112
7.4.2. Comparison of Different Metals	115
7.5. Shielding Effectiveness of Multifunctional Composite with CFRP and Cu Mesh Layers	118
7.6. Limitations of the SE Model, Overestimation of CFRP SE	121
7.7. Conclusions and Future Work	124
Chapter 8: Summary of Conclusions and Future Work.....	126
Bibliography	135

List of Tables

Table 5.1. Processing conditions for the three covetic samples made with the redesigned impeller	75
Table 7.1. Summary of the material properties used for each CFRP ply	102
Table 7.2. Summary of the material properties and mesh geometries used in the calculation of equivalent sheet impedance for the metal wire meshes.....	116

List of Figures

Figure 1.1 TEM images and selected area diffraction pattern of Al-6061. a) (111) electron diffraction pattern of Al-6061 cv 3% from the left region in b). The hexagonal bright spots correspond to the Al <220> spots. The weak spots, labeled 1 and 2, in the inner circle are due to the <1010> reflections on the (0001) plane of crystalline graphite. b) Bright field TEM image of the sample. c) and d) dark field (DF) TEM images using the weak spots 1 and 2 in a), respectively. e) Diffraction pattern from the upper right area in b) showing a broad ring corresponding to amorphous carbon. Reproduced from Jaim, H. M. I. et al. Sp² carbon embedded in Al-6061 and Al-7075 alloys in the form of crystalline graphene nanoribbons. Carbon, 107, 56–66 (2016). 6

Figure 1.2. Schematic showing the epitaxial relationship between graphite and the (111) plane of Al corresponding to the pattern observed in Fig 1a). Reproduced from Jaim, H. M. I. et al. Sp² carbon embedded in Al-6061 and Al-7075 alloys in the form of crystalline graphene nanoribbons. Carbon, 107, 56–66 (2016). 7

Figure 1.3. Concept of shielding effectiveness (SE) for a slab of conductive material, wave absorption, reflection, re-reflection, and transmission mechanism. Reproduced from Munalli, D., Dimitrakis, G., Chronopoulos, D., Greedy, S., & Long, A. (2019). Electromagnetic shielding effectiveness of carbon fibre reinforced composites. Composites Part B: Engineering, 173. <https://doi.org/10.1016/j.compositesb.2019.106906>..... 14

Figure 2.1. Schematic of processing system enclosed in an AA-6061 box. A hole is cut in the top of the box where the stirrer and graphite cathode are inserted. The stirrer is mounted to an AA-6061 frame on the front of the enclosure and the graphite cathode is connected to a robotic arm on the back of the enclosure, similar to how the IR thermometer is mounted to a frame on the left side of the enclosure. The induction coils wrap around the graphite crucible that contains the molten starting materials. The Ar inlet is connected to the Ar tank (not pictured) by PVC tubing, and the gas outlet is connected to the room’s vent by metal exhaust tubing. 20

Figure 2.2. AA-1350 and activated carbon starting material arrangement inside the graphite crucible. 21

Figure 2.3. Top-down view of the cast covetics sample showing where microscopy and electrical conductivity samples were sectioned from..... 23

Figure 3.1.A) Voltage and current during covetics processing. The DC power supply was operated in current-control mode. B) Temperature during the application of current 31

Figure 3.2. Diagram of the covetics processing apparatus with r=0 cm indicated the radial axis of symmetry. The orange area represents the copper electrode, the black areas indicate the graphite electrode tip and crucible, and the gray area indicates the molten mixture of AA-1350 and activated carbon. 31

Figure 3.3.A) COMSOL model of the current density distribution for the Cu-C electrode throughout the covetics system, B) Current density as a function of radial distance at z=3.5 cm, C) 2D slice showing the current density through a cross-section of the covetics system 33

Figure 3.4.A) COMSOL model of the electric potential for the Cu-C electrode, B) voltage as a function of radius at z=3.5 cm, C) voltage as a function of z at r=3 cm, D) electric field distribution showing a high field region confined to the graphite tip of the electrode, E)

radial and z component of electric field as a function of radius at z=3.5 cm, and F) radial and z component of the electric field as a function of z at r=3 cm.....	34
Figure 3.5. COMSOL model of the pointed graphite electrode showing A) current density through the system, B) current density as a function of radius at z=3.5 cm C) electric potential, D) voltage as a function of radius at z=3.5 cm, E) electric field distribution and F) Radial and z component of electric field as a function of radius at z=3.5 cm.....	35
Figure 3.6. Diagram of where in the cast covetic samples for Raman spectroscopy and electrical conductivity were taken in the critical current density investigation. R=0 cm is in the high current density region (25 A/cm ²) near the electrode and r=1 cm is in a lower current density region (5 A/cm ²) away from the electrode.....	36
Figure 3.8. Left: Raman spectra collected from r=0 cm section that showed an increase in crystallite size of the carbon, and Right: Optical images showing the regions where the Raman spectra were obtained.	39
Figure 3.9. Raman spectra (right) collected from an area at r=0 cm (left) with crystallite size comparable to activated carbon	40
Figure 3.10. Histogram of crystallite size of the nanocarbon calculated for all 10 maps for the r=0 cm covetic sample	40
Figure 3.11. Raman spectra (right) from areas of the r=1 cm (left) that do not show the G and D peaks characteristic of graphitic carbon	41
Figure 3.12. Electrical conductivity at r=0 cm and r=1 cm for the covetic and baseline samples	42
Figure 4.1. Vickers Hardness vs. porosity estimated from density measurements for AA-1350 3 wt% C samples. There is a trend that the hardness increases with decreased porosity in the sample. Reproduced from Ge, X., Klingshirn, C., Morales, M., Wuttig, M., Rabin, O., Zhang, S., & Salamanca-Riba, L. G. (2021). Electrical and structural characterization of nano-carbon–aluminum composites fabricated by electro-charging-assisted process. Carbon, 173, 115–125. https://doi.org/10.1016/j.carbon.2020.10.063	49
Figure 4.2. Scanning electron micrographs showing the presence of voids near carbon ROIs. The areas circled in red indicate the regions that showed increased graphitic carbon crystallite size by Raman. The small arrows etched into the sample surface, highlighted by the white dashed circles, were milled by FIB for easy identification of the ROIs in the various characterization instruments.	50
Figure 4.3.A) SEM micrograph of the area analyzed by EDS where precipitates were visible at a grain boundary. B) Fe element map C) Al element map and D) O element map. The precipitates mainly consist of Fe. O was observed in the precipitates and throughout the aluminum in lower concentrations.....	51
Figure 4.4.A) TEM micrograph showing a large carbon cluster connected to an Al grain with an interfacial oxide layer. The strong spots in the upper right diffraction pattern corresponds to the c-axis of graphite and the lower left diffraction pattern corresponds to the (110) crystallographic orientation of Al. B) HRTEM micrograph showing many graphite layers with some misalignment of layers.	52
Figure 4.5.A) Optical micrograph from where the indent on the carbon inclusion was collected, shown by the crosshairs at the center of the micrograph. B) Optical micrograph showing where the indent on the matrix was collected. C) Load-displacement curve showing that the carbon inclusion has much lower hardness and reduced elastic modulus than the matrix indent, shown by the lower load needed to indent to the same depth and the decreased slope of the unloading curve	55

Figure 4.6.A) Optical micrograph with a diagram showing the areas where Raman spectroscopy (red circles) and nanoindentation (red square) were performed. B) Load-displacement curves for the indentation array showing variation in mechanical response. C) Bar chart of reduced elastic modulus and D) hardness showing that there is significant point-to-point variation in properties for the different indents in the array. 57

Figure 4.7. nanoECR measurements with a 5 V bias comparing current flow through the indenter tip when on the carbon inclusion and the aluminum matrix..... 58

Figure 4.8. EBSD maps showing that the graphitic carbon ROI in Figure 4.9, occurs at the boundary between two grains with different orientations. 59

Figure 4.9. Left: Raman spectra and map of graphitic carbon crystallite size for the carbon ROI that occurs at a grain boundary in the SEM image at right. 60

Figure 4.10.A) SEM micrograph showing the area of the covetic sample where the nanoindentation array was placed. B) Topography SPM micrograph prior to indenting showing the placement of the array and C) Gradient SPM micrograph after indentation showing the placement of indents..... 61

Figure 4.11.A) Optical micrograph showing the location of the indentation array on a grain boundary of the baseline sample. B) SPM topography micrograph showing the position of the indentation array relative to the precipitates visible at the grain boundary. The indents were performed in load control mode..... 62

Figure 4.12. Summary of reduced elastic modulus and hardness calculated from the nanoindentation arrays performed on/around the grain boundaries in the baseline and covetic samples. The covetic showed no difference in reduced elastic modulus and hardness at the grain boundary from the baseline sample. 62

Figure 4.13. A) Optical micrograph showing a representative area of the baseline sample where an indentation array was placed. B) Load-displacement curves for all indents into the baseline sample, showing minimal variation. C) Optical micrograph showing a representative area of the covetic sample where indentation arrays were placed. There is considerably more microstructural heterogeneity than the baseline sample. D) Load-displacement curves for indents on the covetic sample. Consistent with the microstructural heterogeneity, there is more heterogeneity in the mechanical response than for the baseline. 63

Figure 4.14. Summary of reduced elastic modulus and hardness measured from the indentation arrays placed near the three covetic ROIs, a random area of the covetic sample, and the baseline sample. 64

Figure 4.15. Hardness plotted vs. reduced elastic modulus showing that the modulus was reduced in all covetic sample compared to the baseline. The covetic sample also showed more variation in hardness than the baseline sample. 65

Figure 4.16. Total Euclidian distance vs. number of clusters used to evaluate the optimum number of clusters by the elbow method. The optimum number of clusters is chosen as the point where the decrease in distance for each additional becomes linear, which for this dataset is $k=5$ 65

Figure 4.17.A) H vs. E_r data grouped into five clusters using the k-means clustering method. The two clusters with the lowest modulus, k_3 and k_5 , were assumed to be influenced by voids in the covetic sample and were excluded from B) the statistical summary. 66

Figure 5.1. The stirrer mounted on an aluminum frame above the aluminum enclosure that contains the induction furnace. The black cylinder indicates the position of the crucible in the enclosure box.	72
Figure 5.2. Diagram of the stirrer that consists of a graphite impeller attached to a hollow stainless-steel shaft shown from the A) side view and B) bottom view. The red arrows indicate the direction of argon flow through the shaft and out into the melt through holes in the graphite impeller	74
Figure 5.3. Histograms showing the crystallite size for each sample calculated from the Raman spectra. A) Sample A, B) sample A with the y-axis maximum changed to ten counts so that the lower counts at higher crystallite size are visible, C) Sample B, D) Sample B with y-axis maximum of 10 counts, E) Sample C and F) Sample C with y-axis maximum of 10 counts	77
Figure 5.4. Electrical conductivity measured from the two baseline samples and three covetic samples.	78
Figure 5.5. Photographs of the interior cross-sections of A) the baseline sample B) Sample A and C) Sample B. All three samples show voids, with the covetics showing higher porosity.....	78
Figure 6.1.A) Cross-sectional SEM micrograph of the multifunctional composite showing three CFRP layers and two copper (bright areas) mesh layers. B) Three CFRP layers with different relative fiber orientations showing normal to the page in the top and bottom layer and fibers parallel to the page in the center layer. C) Schematic of fiber orientations in the micrograph. D) X-ray CT image showing the two copper layers with 45° relative orientation between the layers.....	83
Figure 6.2.A) Representative Raman spectrum collected from the PEEK matrix. The red asterisk indicates the 1651 cm ⁻¹ peak used to calculate percent crystallinity of PEEK. B) PEEK crystallinity calculated from the Raman data before and after the annealing procedure.....	85
Figure 6.3 Histograms of nanoindentation results from the three areas, A) Reduced elastic modulus pre-anneal near fiber, B) Hardness pre-anneal near fiber, C) Reduced elastic modulus post-anneal near fiber, D) Hardness post-anneal near fiber, E) Reduced elastic modulus pre-anneal near Cu and F) Hardness pre-anneal near Cu.	86
Figure 6.4 Scanning probe micrographs collected using the nanoindentation piezo-scanner showing the indentation arrays. A) Topography image near carbon fibers B) Gradient image near carbon fibers, C) Topography image near Cu, and D) Gradient image near Cu.	88
Figure 6.5. Nanoindentation results as a function of distance from the carbon fiber edge before and after annealing. A) Reduced elastic modulus for all data points, B) Reduced elastic modulus in the region <5 μm from the fiber edge, C) Hardness for all data points, and D) Hardness in the region <5 μm from the fiber edge.....	89
Figure 6.6. Average reduced elastic modulus and hardness in the matrix and interface regions. The interface region was defined as data points < 5 μm from the fiber edge and the matrix region was defined as data points > 5 μm from the fiber edge.....	90
Figure 6.7 Power law fits for A) reduced elastic modulus and B) hardness as a function of distance from the fiber edge before and after annealing.....	91
Figure 6.8. Nanoindentation results as a function of distance from the Cu edge before and after annealing. A) Hardness for all data points, B) Hardness s in the region <5 μm from the fiber edge, C) Reduced Elastic Modulus for all data points, and D) Reduced Elastic Modulus in the region <5 μm from the fiber edge.....	93
Figure 6.9. Power law fits for A) reduced elastic modulus and B) hardness as a function of distance from the Cu.....	94

Figure 7.1. Geometry of the EM shielding model where Port 1 is the transmitter generating the EM wave and Port 2 is the receiver. The shield is placed between the two ports. Periodic boundary conditions were applied to the remaining four faces of the model to generate a semi-infinite shield in the x and y directions.....	99
Figure 7.2. Plot of wavelength at a given frequency in the range A) 10 MHz to 1000 MHz (1 GHz) and B) 1 GHz to 10 GHz.	101
Figure 7.3. Evaluation of the validity of the lossy conductor approximation for permittivity in A) the longitudinal direction parallel to the fibers and B) the transverse direction perpendicular to the fibers.	105
Figure 7.4. The effect of varying A) longitudinal electrical conductivity, B) transverse conductivity and C) real part of the imaginary permittivity on the SE in the range 1-16 GHz for a lay-up of $[90^\circ, 0^\circ, +45^\circ, -45^\circ, 0^\circ, 90^\circ]$	107
Figure 7.5. The effect of ply thickness on SE in the range 2-10 GHz for the lay-up $[90^\circ, 0^\circ, +45^\circ, -45^\circ, 0^\circ, 90^\circ]$. In A) the ply thickness is 0.125 mm, and in B) the ply thickness is 0.0625 mm.	108
Figure 7.6.A) Electric field magnitude and B) current density magnitude distribution through the model for the lay-up $[90^\circ, 0^\circ, +45^\circ, -45^\circ, 0^\circ, 90^\circ]$ at 2 GHz. The thickness of each ply was 0.125 mm.	109
Figure 7.7.A) EM power loss and B) current density as a function of z through the center of the shield at 2 GHz for the model shown in Figure 7.6 with a lay-up of $[90^\circ, 0^\circ, +45^\circ, -45^\circ, 0^\circ, 90^\circ]$	110
Figure 7.8. SE in the range 50 MHz to 10 GHz for A) the lay-up $[90^\circ, 0^\circ, +45^\circ, -45^\circ, 0^\circ, 90^\circ]$ and B) the lay-up $[90^\circ, 0^\circ, +45^\circ, -45^\circ]$ with reduced number of plies/overall laminate thickness.	111
Figure 7.9. SE in the range 50 MHz to 10 GHz for A) the lay-up $[90^\circ, 0^\circ, +45^\circ, -45^\circ]$ and B) the lay-up $[90^\circ, 90^\circ, 90^\circ, 90^\circ]$ with the same thickness but with fibers oriented in only one direction, the y-direction.....	112
Figure 7.10. Geometry of the wire mesh. The individual meshes are square and the wire junctions are assumed to be bonded. Reproduced from Casey, K. F. (1988). Electromagnetic Shielding Behavior of Wire-Mesh Screens. IEEE Transactions on Electromagnetic Compatibility, 30(3), 298–306. https://doi.org/10.1109/15.3309	114
Figure 7.11. Comparison of A) SE experimentally measured by the manufacturer of the Cu mesh used in the multifunctional composite, DexMet and B) the SE of the Cu mesh calculated using the equivalent sheet impedance, indicating that the results are equivalent.....	115
Figure 7.12.A) SE calculation using the equivalent sheet impedance approximation for different metals with different electrical conductivities and B) SE calculated for each metal normalized to density of the metal.....	117
Figure 7.13. SE calculated using the equivalent sheet impedance approximation for the Cu mesh with different open mesh dimension, a_s	118
Figure 7.14. Calculated SE in the range 50 MHz-10 GHz for A) the baseline CFRP with the lay-up $[90^\circ, 0^\circ]$, B) the baseline Cu mesh with $a_s=474$, C) the lay-up $[Cu, 90^\circ, 0^\circ]$, D) the lay-up $[90^\circ, Cu, 0^\circ]$, and E) the lay-up $[90^\circ, 0^\circ, Cu]$	120
Figure 7.15.A) Current density x, y, and z components through the shield in the z-direction at 11 GHz. The layer thickness is 0.125 mm. Current flow changes direction within a single ply, however the skin effect, where the induced current should be confined to the surface of the	

ply, is not accurately reflected by the model. B) Plot of skin depth vs. frequency indicating that at 11 GHz the skin depth should be smaller than the ply thickness. 123

List of Abbreviations

AA	Aluminum alloy
AC	Alternating current
CFRP	Carbon fiber reinforced polymer
CNT	Carbon nanotube
CVD	Chemical vapor deposition
DC	Direct current
DFT	Density functional theory
EBSD	Electron backscatter diffraction
ECR	Electrical contact resistance
EDS	Energy dispersive spectroscopy
E_{eff}	Effective elastic modulus
EELS	Electron energy loss spectroscopy
EM	Electromagnetic
EMI	Electromagnetic interference
E_r	Reduced elastic modulus
FEA	Finite element analysis
FIB	Focused ion beam
GDMS	Glow discharge mass spectroscopy
H	Hardness
HAADF	High angular annular dark field
HRTEM	High-resolution transmission electron microscopy
IACS	International annealed copper standard
LiPo	Lithium ion polymer
MMC	Metal matrix composites
PEEK	Polyether ether ketone
PLD	Pulsed laser deposition
ROI	Region of interest
SE	Shielding effectiveness
SEM	Scanning electron microscopy
SIMS	Secondary ion mass spectroscopy
SPM	Scanning probe microscopy
SPS	Spark plasma sintering
STEM	Scanning transmission electron microscopy
TEM	Transmission electron microscopy
TGA	Thermogravimetric analysis
XPS	X-ray photoelectron spectroscopy

Chapter 1: Introduction

1.1. Composite Materials with Carbon Nanostructure Fillers

Carbon nanostructures such as graphene and carbon nanotubes (CNTs) have superior electrical, thermal, and mechanical properties that make them excellent candidates for reinforcement phases in composite materials. Graphene has been shown to have a high electron mobility of $20 \text{ m}^2/\text{Vs}$ at room temperature¹⁻³. Graphene also has an extremely high intrinsic strength of 130 GPa and elastic modulus of 1 TPa, which is notable for its balance of high strength and ductility⁴. For carbon nanotubes, the electrical properties can vary depending on structure and chirality (they can be metallic or semiconducting), but they possess similar high strength and elasticity to graphene with ~ 100 GPa strength and ~ 1 TPa elastic modulus⁵. Graphene, CNTs and other graphitic carbon have all been studied as reinforcement phases in polymer, ceramic, and metal matrix composites (MMCs) to improve electrical, thermal and mechanical properties^{6,7}. One system of interest is the incorporation of carbon nanostructures into high conductivity metals, such as copper or aluminum, that are used for electrical applications such as power generation and transmission due to their balance of conductivity, mechanical properties, and cost. Further improving their conductivity and/or mechanical strength through the addition of carbon nanostructures could result in more efficient energy systems and billions of dollars in energy savings; however, there are several processing challenges currently limiting commercial viability^{7,8}.

The improvement of electrical and mechanical properties in nanocarbon-MMCs relies on efficient transfer of electrons and load, respectively, between carbon and the metal matrix. It is believed that the electrical conductivity is enhanced by a doping effect, where the metal donates

charge carriers to the nanocarbon that has higher electron mobility but lower charge carrier density, providing a high-speed conduction path throughout the matrix that enhances electrical conductivity of the composite⁹. A strongly bonded, defect-free interface between carbon and metal is required for this doping effect to occur⁹. With regards to mechanical properties, interfacial shear strength via bonding between carbon and the metal matrix dictates the strengthening effects. It is desirable to have strong bonding between carbon and the metal matrix so that efficient load transfer can take place^{6,10}. Thus, the nature of the carbon-metal interface dictates both the electrical and mechanical properties of the composite¹¹. A successful fabrication method would distribute nanocarbon homogeneously throughout the metal matrix while forming strongly bonded, low defect interfaces to produce a composite with improved electrical and mechanical properties.

The primary processing challenge is the high surface energy of carbon when in contact with most metals, leading to low solubility in metals such as copper and aluminum⁷. This causes carbon to aggregate during processing and makes it difficult to form an adequate interface^{6,7,11-13}. Ultimately, this limits performance, which is why electrical and mechanical properties have sometimes been observed to degrade at higher carbon concentrations^{9,11,14-16}. Additionally, the high surface area of nanocarbon structures exacerbates the issue of surface tension and low solubility. On the other hand, if the issue of surface tension could be resolved, the high aspect ratio of carbon nanostructures would provide an increased ability to improve properties relative to fillers with lower aspect ratio, like spherical particles, due to the increased surface area where electron/load transfer occurs. Potentially, that contributes to the instances where improvements in electrical and mechanical properties have been measured, as mentioned below. Thus, a key

development in graphene-MMC fabrication technology would be a successful method of addressing the issue of aggregation and poor interfacial bonding.

A secondary issue is the reactivity of metal with carbon and oxygen leading to metal carbide or oxide formation, such as Al_4C_3 or Al_2O_3 for Al matrix composites. There are conflicting reports about the effect of Al_4C_3 and Al_2O_3 on the mechanical properties of aluminum/carbon composites, where some authors saw an improvement in strength¹⁷ and some saw a reduction¹⁸; however, it has been shown that these brittle phases reduce ductility, so the overall toughness would be compromised¹⁹⁻²¹. Also, Al_4C_3 and Al_2O_3 are insulating materials so they would cause the electrical conductivity to decrease²². Therefore, it is best to prevent the formation of oxides and carbides during processing.

Many processing techniques have been used to fabricate nanocarbon-MMCs, but powder metallurgy techniques have been used most widely^{6,15,16,18,19,21-23}. Some other methods that have been used are chemical vapor deposition (CVD), thermal spraying, cold spraying, melt processing, spark plasma sintering (SPS), electrodeposition, etc.^{9,12,14,17,20,24,25}. Most authors report a decrease in electrical conductivity due to inadequate nanocarbon dispersion and/or interfacial bonding⁷. There are, however, some notable achievements. An electrical conductivity of 117% IACS was measured for a Cu/Graphene composite made by CVD⁹. Additionally, a 22.5% increase in tensile strength with no decrease in elongation and 17.4% increase in electrical conductivity was achieved in an AA-6063/Graphene composite made by ball milling with pressure infiltration and hot extrusion²². In both cases, the improvement was attributed to adequate dispersion of graphene throughout the metal matrix with a strong, defect-free interfacial bond between carbon and the metal.

1.2. Covetics: *in-situ* Formation of Graphene-Metal Matrix Composites

An *in-situ* method of forming carbon nanostructures within the matrix material could address some of the issues with homogeneity, interfacial strength, and carbide/oxide formation. These methods would also address the issue of the high cost of graphene and the difficulty in obtaining high quality graphene in large quantities for scalable manufacturing. The covetics process, an *in-situ* method of forming graphitic carbon within a molten metal, was patented by Third Millennium Materials, LLC^{26,27}. The process involves applying a direct current (DC) to a mixture of molten metal and a carbon starting material (usually activated carbon,) which is believed to induce crystallization of the carbon into graphitic carbon nanostructures that are then incorporated in the metal matrix. The process was originally developed for copper and later extended to additional metals (gold, zinc, lead, aluminum, tin, etc.), with extensive characterization performed on copper, silver, and aluminum alloy covetics reviewed in reference²⁸. Density-functional theory (DFT) predicts that a covalent bond forms between carbon and metal atoms, which produces an increase in electrical conductivity, thermal conductivity, and mechanical properties^{29,30}. Early reports on covetics that showed improved properties have generated much interest in further studying this process, but there is still limited understanding of the DC current-driven process and the carbon structures that form.

Brown et al. characterized an AA-6061 3 wt% C covetic sample, made by Third Millennium Materials LLC, that showed an improvement in both electrical and mechanical properties³¹. An electrical conductivity of 67.3% IACS was measured in the as-extruded condition, a notable achievement considering that electrical grade Al has a conductivity of 62% IACS, but after T6 heat treatment, the conductivity dropped to 47.8% IACS, comparable to the reference specimen with no added carbon. There was also a similar effect in the mechanical

properties, where the yield strength and ultimate tensile strength in the as-extruded condition improved by 23.4% and 29%, respectively, but the improvement was negligible after T6 heat treatment^{8,31,32}. T6 heat treatment involves solutionizing at 530°C and quenching followed by artificial aging at 150-180°C³³, and it is not fully understood how the carbon nanostructure transforms during this process and why it resulted in a decrease in electrical and mechanical properties.

Structural characterization techniques were used to investigate the nanocarbon structure and its bonding behavior in Ag, AA-6061 and AA-7075 covetic samples made by Third Millennium Materials^{29,30}. Transmission electron microscopy (TEM) diffraction patterns indicated that the (111) zone axis of the metal also contained weak diffraction spots that corresponded with the basal plane of sp² graphitic carbon. Dark field images were collected by selectively using only the signal of one of the weak spots in the diffraction pattern during imaging, which indicate that graphene nanoribbons form that extend throughout the metal grain, shown in Figure 1.1, with a schematic of the epitaxial arrangement in Fig. 1.2. Electron energy loss spectroscopy (EELS), Raman and X-ray photoelectron spectroscopy (XPS) gave further evidence that the carbon in covetics is sp² in nature. This structural imaging and characterization gave insight into the mechanism that led to an increase in electrical and mechanical properties. The application of current during the covetics process leads to *in-situ* formation of sp² graphene nanoribbons in the molten metal that, when solidified, extend through the metal grains in high-aspect ratio structures. It has also been noted that covetic samples show non-uniformity of carbon throughout the sample and contain porosity and voids³⁴.

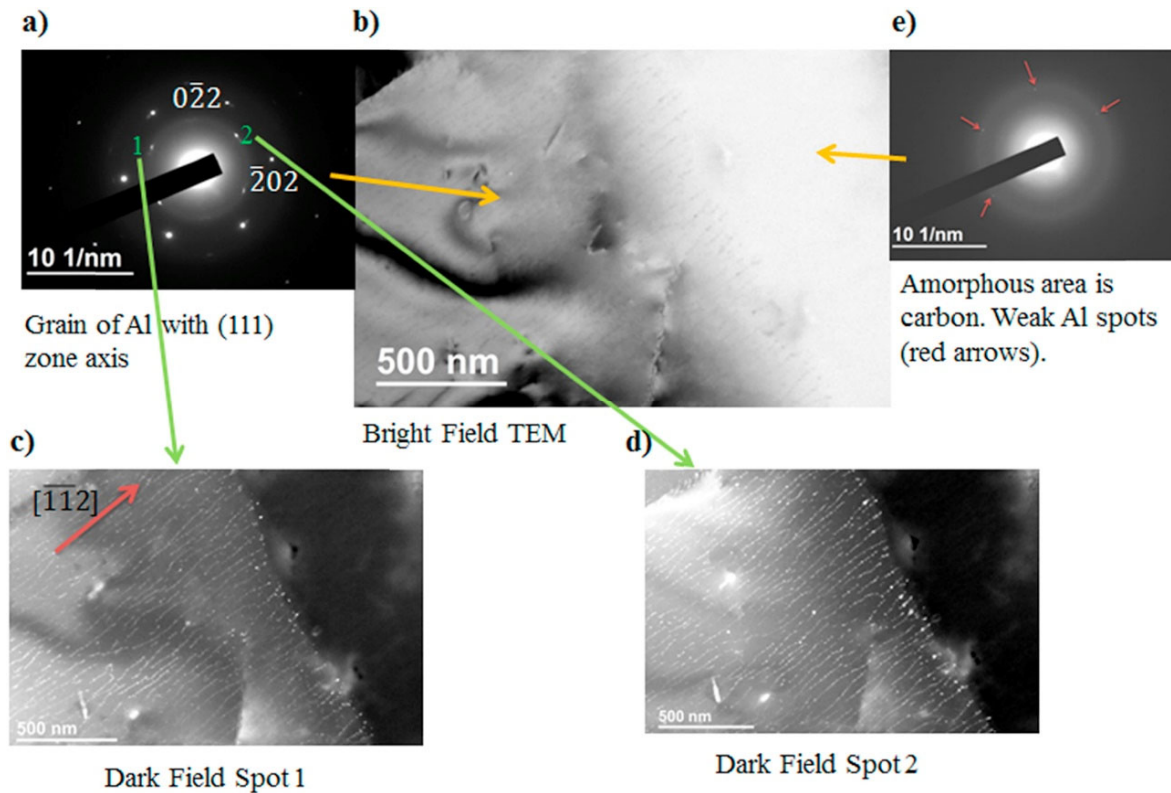


Figure 1.1 TEM images and selected area diffraction pattern of Al-6061. a) (111) electron diffraction pattern of Al-6061 cv 3% from the left region in b). The hexagonal bright spots correspond to the Al <220> spots. The weak spots, labeled 1 and 2, in the inner circle are due to the <10 $\bar{1}$ 0> reflections on the (0001) plane of crystalline graphite. b) Bright field TEM image of the sample. c) and d) dark field (DF) TEM images using the weak spots 1 and 2 in a), respectively. e) Diffraction pattern from the upper right area in b) showing a broad ring corresponding to amorphous carbon. Reproduced from Jaim, H. M. I. et al. Sp² carbon embedded in Al-6061 and Al-7075 alloys in the form of crystalline graphene nanoribbons. *Carbon*, 107, 56–66 (2016).

To summarize the work done on copper coveotics, there have been three groups who have fabricated and characterized copper coveotics. Knych et al.^{35,36} created a batch reactor to make copper coveotics by a similar process to Third Millennium Materials, LLC. In one sample, the electrical conductivity improved to 102.4% IACS compared to 101.4% IACS for the baseline, but secondary ion mass spectroscopy (SIMS) showed little carbon³⁵. Additionally, wires were drawn from several copper coveotic specimens for electrical and mechanical testing, but there was negligible improvement in either³⁶. Isaacs et al. used electron beam deposition and pulsed laser deposition (PLD) with a 5 wt% copper coveotic target made by Third Millennium, LLC to deposit

covetic thin films^{37,38}. These films showed up to 4 wt% C, measured by XPS, and showed higher transmittance to light, lower sheet resistance, and greater resistance to oxidation than films of the same thickness made with a pure copper target^{37,38}. Ma et al. used an

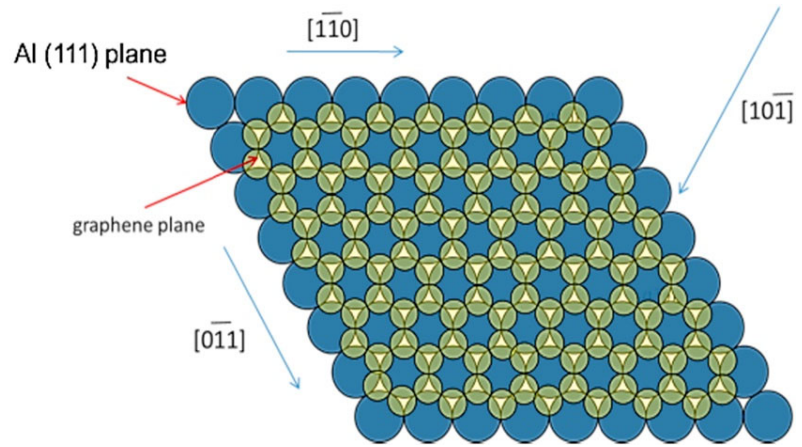


Figure 1.2. Schematic showing the epitaxial relationship between graphite and the (111) plane of Al corresponding to the pattern observed in Fig 1a). Reproduced from Jaim, H. M. I. et al. *Sp² carbon embedded in Al-6061 and Al-7075 alloys in the form of crystalline graphene nanoribbons*. *Carbon*, 107, 56–66 (2016).

electron beam melting process to make copper covetic samples, which showed an improvement in electrical conductivity, 107.4% IACS (107.4 MS/m) compared to 100.5% IACS (58.29 MS/m) for the baseline³⁹. Scanning TEM-high angle annular dark field (STEM-HAADF) revealed carbon-rich networks extending throughout the metal grains⁴⁰. The results from these three groups indicate that copper covetics show potential for use in electronic components with increased oxidation resistance.

1.3. Characterization Challenges for Covetic Materials

Presently, there are still issues with characterization of covetic materials. There is a lack of a standardized method for quantifying the carbon content in covetics. For the same Cu-5 wt% covetic sample, four carbon quantification methods yielded different results, ranging from trace amounts for LECO combustion analysis and glow discharge mass spectroscopy (GDMS) to 3.5 and 3.78 wt% for EDS and XPS, respectively^{8,28}. Most samples are described by the nominal weight of carbon precursor added, but it is likely that the actual carbon content incorporated into covetics as a graphitic structure is lower than full yield due to carbon precursor aggregation and

segregation to the surface, and oxidation of carbon with air at the elevated temperatures used during processing (~700-1100°C). The biggest challenge in carbon quantification is the trade-off between resolution and amount of material sampled. EDS and XPS sample small volumes of material (on the order of cubic μm), so the results are not necessarily generalizable to the entire bulk sample (on the order of cubic cm). Additionally, hydrocarbon contamination in the vacuum chamber and adventitious carbon on the sample surface can make accurate carbon quantification difficult when using these methods. XPS depth profiling by sputtering the covetic sample surface with Ar ions has been used to mitigate the influence of hydrocarbon contamination on the carbon concentration and measure the carbon concentration in the interior of the sample. LECO and GDMS sample larger volumes of material, but the authors attributed the low C concentration detected to “strong bonding between the carbon and metal” that prevented the carbon from reaching the analyzer^{8,28}. If an accurate method of quantifying the carbon content of covetics could be standardized, it would aid in developing structure-process-property relations to understand the role of process parameters, such as applied current and duration, on amount of carbon incorporated. Additionally, it would enable determination of electrical and mechanical properties as a function of carbon content in covetics.

For mechanical characterization, it must be considered that strengthening of a material can be a result of multiple underlying mechanisms. In covetics, as well as other studies on carbon nanostructure-MMCs, it has been noted that the addition of carbon pins grain boundaries, leading to smaller grains^{18,22,31,41,42}. Decreased grain size is known to strengthen a material by the Hall-Petch effect, so it is necessary to assess whether strengthening in carbon-MMCs can be explained by grain size alone, or if the carbon structure is providing an additional mechanism by which the material is strengthened. Molecular dynamics simulations of a nanoindentation test

into a single Al grain containing a graphene nanoribbon predicts a 15-25% increase in hardness by addition of the graphene nanoribbon, due to graphene blocking dislocation motion⁴³. Future work validating this finding with experimental nanoindentation testing could help more accurately assess the role of the carbon structure acting to reinforce the material in covetics.

1.4. Recent Work on 3 wt% AA-1350 and 6061 Covetics Made at the University of Maryland

Recently, work on covetics has focused on understanding the role of the covetics process parameters. In particular, understanding the current necessary to drive the process and crystallize graphene or graphitic carbon from activated carbon precursor in the molten metal. Ge et al.⁴¹ studied AA-6061 and AA-1350 3 wt% C covetics made using 100 and 150 A at <10 V. It was found by dark field TEM that graphitic networks extend through Al grains, and Raman and XPS further indicated sp² carbon. By testing different areas of the sample that experienced relatively higher and lower current densities, it was determined that the high current density region surrounding the electrode contains the graphitic carbon networks. These samples showed comparable electrical conductivity to the base alloy, although hardness and elastic modulus measured by nanoindentation increased for the AA-1350 covetic samples. A follow-up study by Ge et al⁴⁴. fabricated AA-1350 3 wt% C covetic samples using 100-200 A for different times. It was found that electrical conductivity and graphitic carbon crystallite size measured by Raman increased for increased duration of current application. There was a 5.6% increase in electrical conductivity and an 8.2% increase in hardness reported, and it was estimated that a current density of 100 A/cm² is necessary to crystallize graphitic carbon and enhance properties. Future work studying the reaction process to quantify the current density threshold more precisely would aid in optimizing reactor design and improving sample quality.

The primary challenge is that there have been notable electrical and mechanical property improvements recorded for AA-6061 covetics, but there has been an inability to reproduce the result due to an incomplete understanding of the fabrication process and the structure that forms³¹. Structural characterization techniques have determined that there is graphitic carbon and graphene nanoribbons present in covetic samples that are believed to be responsible for property improvement, but it has also been noted that there is porosity and aggregation of the carbon precursor, and properties are not always improved. As a result, more recent work has focused on studying the reaction process itself to understand the role of current density in crystallizing graphitic carbon, with the goal of improving sample quality and batch-to-batch consistency^{41,44}.

It has been hypothesized that a current density of around 100 A/cm^2 is necessary to crystallize graphitic carbon from the activated carbon precursor when using a tapered graphite cathode, and more precisely determining this value would give insight into a key process parameter that would allow more efficient design of the covetics reactor⁴⁴. Ensuring that a maximal volume of material experiences the current density necessary for crystallization of the carbon is essential to addressing sample quality issues. The effects of parameters such as applied current, time and temperature must be evaluated with respect to the amount of carbon incorporated, its structure, and the resulting electrical, thermal, and mechanical properties.

The objective of this work is to gain a better understanding of how reaction parameters, such as current density, influence the carbon structure that is formed in covetics and understand how that carbon structure gives rise to an increase in electrical and/or mechanical properties. AA-1350 3 wt% C covetic samples were characterized structurally, electrically, and mechanically to give insight into what conditions produced the optimal result: graphene nanoribbons homogeneously distributed throughout the sample, forming a strongly bonded

interface with the metal matrix so that electrical conductivity and mechanical properties are improved. Particular attention is given to addressing issues with porosity and homogeneity of carbon.

1.5. Multifunctional Composite Materials and Structures

A multifunctional composite is a structure that performs a structural function and at least one additional non-structural function. The advantage of utilizing a multifunctional composite is that weight can be reduced by combining materials with different properties and functions into a single component, which is especially important for aerospace applications⁴⁵. For the structural, load-bearing function, mechanical properties such as stiffness, strength, fracture toughness, ductility, etc. of the composite are relevant. For aerospace applications, carbon fiber reinforced polymers (CFRPs) are typically used for structural components due to their attractive mechanical properties and low weight⁴⁶. The non-structural component most often provides some function related to the electrical and/or thermal properties, such as thermal insulation, energy harvesting/storage, electrical conductivity, lightning strike protection or electromagnetic shielding^{45,47-52}.

In this work, the mechanical and electrical properties of a multifunctional composite consisting of a structural material and an electrically conductive material with shielding function in the radiofrequency and microwave regime were investigated. The structural function is primarily provided by an IM7/polyether-ether ketone (PEEK unidirectional CFRP laminate, and the electromagnetic shielding function is primarily provided by the incorporation of copper mesh layers between CFRP plies. However, the CFRP laminate also contributes to electromagnetic shielding. The interfacial mechanical properties of the carbon fibers and copper mesh with the matrix (PEEK) were characterized and related to the manufacturing process. Additionally, a

finite element analysis (FEA) model to predict electromagnetic shielding effectiveness (SE) for different geometry and laminate lay-ups was developed in an attempt to determine the optimum configuration of copper mesh layers within the CFRP lay-up. The overall goal of both efforts was to assist in development of a multifunctional composite structure that provides a balance of mechanical properties and shielding effectiveness while minimizing weight.

1.6. Mechanical Properties of Multifunctional Composites

With regards to the structural function, it is important to understand the extent to which the addition of a Cu layer into the carbon fiber laminate may degrade the mechanical performance of the composite. The geometric discontinuity introduced into the system by the additional functional component typically degrades the mechanical performance of the multifunctional structure⁵². However, this effect can be mitigated if the structure is designed to integrate the functional component with adequate bonding to the matrix material of the structural component. For example, Pattarakunnan et al.⁵¹ incorporated lithium ion polymer (LiPo) batteries into a carbon fiber sandwich composite and observed that the tensile modulus and failure stress of the composite material were reduced, but when the LiPo batteries were embedded into the core of the composite so that the load-bearing face-skins of the composite sandwich structure were not affected, there was no observed decrease in tensile modulus. Similarly, Xiao et al.⁵³ integrated a stainless steel device into a unidirectional carbon fiber laminate and found that the tensile properties decreased due to delamination at the device-CFRP interface; however, damage propagation in delamination depended on the ply orientation at the device-CFRP interface. These results demonstrate that the successful design of a multifunctional composite structure requires consideration of the microscale interaction between functional and load-bearing components so that overall structural integrity is preserved. Thus, both the

placement of the copper mesh layers in the CFRP laminate lay-up and the microscale interaction at the Cu/PEEK interface could potentially have an effect on the structural performance of the multifunctional composite structure.

1.7. Electromagnetic Shielding Theory

This section gives a general overview of how a material acts as a shield to an electromagnetic (EM) wave. Schelkunoff's theory of EM shielding represents the shield material's attenuation of the EM field as a loss on a transmission line⁵⁴. When an EM wave encounters the shield, there are three mechanisms of shielding. First, backwards reflection of the EM wave at the air-shield interface occurs due to a difference in impedance and index of refraction of the material compared to air^{55,56}. Second, absorption of the signal by the shield decreases the EM field amplitude as it travels through the shield material due to ohmic loss (heat generation in the material as the induced current meets a resistance) and polarization loss (due to electrical and magnetic dipole interactions)^{55,57}. Finally, multiple reflections can occur if there are additional interfaces with impedance differences in the shield material, which can reduce the shielding effectiveness (SE); however, when absorption loss is high (> 15 dB), the effect of multiple reflections can typically be neglected because the amplitude of the re-reflected wave is small^{55,56}. A diagram of the three mechanisms as the EM wave propagates through a homogeneous, isotropic slab of conductive material is given in Figure 1.3. The shielding effective (SE) in dB is defined as

$$SE = 20\log\left(\frac{E_{initial}}{E_{transmitted}}\right) = 20\log\left(\frac{H_{initial}}{H_{transmitted}}\right) = 10\log\left(\frac{P_{initial}}{P_{transmitted}}\right) = R + A + B \text{ [dB]} \quad (1. 1)$$

where E, H, and P indicate the electric field amplitude, magnetic field amplitude, and EM power, respectively. R, A, and B indicate the reflection loss, absorption loss, and multiple reflection correction factor, respectively.

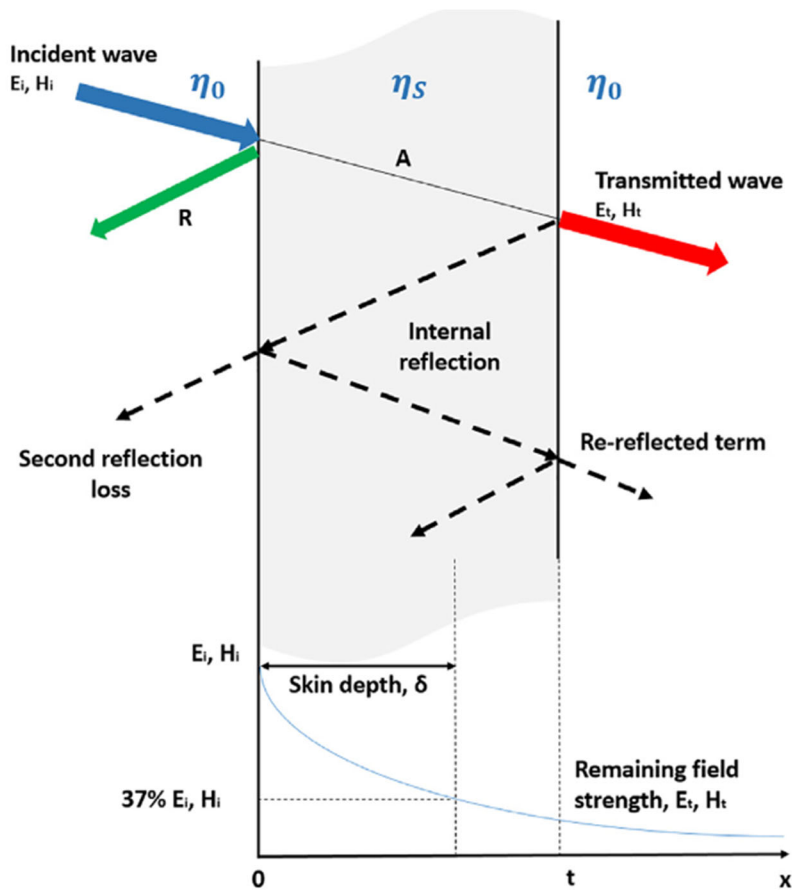


Figure 1.3. Concept of shielding effectiveness (SE) for a slab of conductive material, wave absorption, reflection, re-reflection, and transmission mechanism. Reproduced from Munalli, D., Dimitrakis, G., Chronopoulos, D., Greedy, S., & Long, A. (2019). *Electromagnetic shielding effectiveness of carbon fibre reinforced composites. Composites Part B: Engineering*, 173. <https://doi.org/10.1016/j.compositesb.2019.106906>

The following sections describe the calculation of shielding effectiveness for the simplified case of a homogeneous, isotropic slab of a non-magnetic “good conductor” to demonstrate the physical principles and material properties involved in electromagnetic shielding.

A good conductor is a lossy material for which the electrical conductivity is

much greater than the real part of the permittivity, such that ohmic loss is the dominant absorption mechanism^{58–60}. Additionally, it is assumed that the effect of multiple reflections in good electrical conductors can be neglected due to the significant absorption loss by the skin effect⁵⁶.

1.7.1. Absorption Loss and the Skin Effect

The skin effect is caused by a counter-electromotive force from opposing eddy currents induced by the changing magnetic field inside of a material under the influence of an AC current, which restricts the current density to the region at the surface of the material. In the context of

EM shielding applications, this means that most of the EM energy is absorbed near the surface of the material⁵⁹. The skin depth, δ , of the shield material indicates the penetration depth at which the EM field amplitude drops by a factor of $1/e$. For a good conductor, it is given by⁵⁵

$$\delta = \frac{1}{\sqrt{\pi f \mu \sigma}} \quad [m] \quad (1.2)$$

where f is the frequency of the EM wave in Hz, μ is the magnetic permeability in H/m, and σ is the electrical conductivity in S/m. If the skin depth is much smaller than the thickness of the shield, multiple reflections can be neglected⁵⁶. The skin depth decreases with increasing frequency of the EM wave and increasing electrical conductivity of the material, which leads to better SE by absorption loss.

The absorption loss, A , in dB, is related to the skin depth of the shield material and the thickness, t , of the shield by⁵⁵

$$A = 20 \log e^{\frac{t}{\delta}} \quad [dB] \quad (1.3)$$

Thus, absorption loss by ohmic loss increases as shield thickness increases and skin depth decreases. Because the skin depth decreases with increased frequency, the absorption loss increases with frequency.

1.7.2. Reflection Loss to Plane Waves

When an EM plane wave encounters a material of different impedance, a portion of the wave is reflected back from the surface and a portion is transmitted into the material. The reflection loss, R , in dB, is given by⁵⁵

$$R = 20 \log \frac{|Z_{wave}|}{4|Z_{shield}|} \quad [dB] \quad (1.4)$$

Where Z_{wave} and Z_{shield} are the impedance, in ohms, of the initial wave (typically $Z_0=377 \Omega$, the vacuum impedance) and the shield, respectively. It can be seen that the reflection loss increases

as the shield impedance decreases. The impedance of a material decreases with increased electrical conductivity; thus, the reflection loss increases with increased electrical conductivity⁵⁸. Additionally, the reflection loss decreases with increasing frequency because the impedance of the shield material increases with increasing frequency^{55,58}

1.7.3. Summary

The trends of absorption and reflection loss as electrical conductivity of the shield material and frequency are varied are summarized as follows: (1) Absorption loss increases with increasing electrical conductivity because the skin depth decreases, (2) Absorption loss increases with increasing frequency because the skin depth decreases, (3) Reflection loss increases with increasing electrical conductivity because the shield impedance decreases, and (4) Reflection loss decreases with increasing frequency because the shield impedance increases. Thus, increasing electrical conductivity enhances both the absorption and reflection loss. Additionally, for shielding effectiveness over a wide frequency range, a balance of absorption and reflection loss is desirable to offset the opposing trends with frequency.

1.8. Composite Materials for Electromagnetic Shielding

In CFRPs, the polymer matrix is non-conducting and is neither effective at reflection nor absorption of the EM wave; however, it has been shown that CFRPs alone can shield EM radiation because the graphite fibers in the composite are conducting (6.67×10^4 S/m for IM7 fibers)^{56,61}. Additionally, continuous carbon fibers performed better than discontinuous filler due to higher electrical conductivity from unidirectional contact or weaving⁶². However, graphite fibers still exhibit lower electrical conductivity than metals (5.82×10^7 S/m for IACS copper)⁶³. As a result, most efforts at enhancing the shielding effectiveness of CFRPs involve increasing the electrical conductivity in some fashion, for example by using an intrinsically conductive

polymer⁶⁴⁻⁶⁶, doping the polymer matrix with conductive particles⁶⁷⁻⁷⁰, coating the carbon fibers with a metallic coating⁷¹⁻⁷⁸, or using carbon nanostructures^{57,65,79-89}.

It has also been shown that the anisotropic electrical conductivity of unidirectional continuous carbon fiber composites causes anisotropy in the shielding effectiveness^{90,91}. The unidirectional carbon fiber plies have high electrical conductivity in the fiber direction, and ~3 orders of magnitude lower electrical conductivity in the transverse directions⁹². Thus, unidirectional carbon fiber plies are more effective at shielding fields polarized parallel to the fibers, in the high-conductivity direction, and act similar to a grating⁹³. As a result, the lay-up of unidirectional carbon fiber laminates with different orientation of the carbon fiber from layer to layer can greatly affect the shielding effectiveness of the composite.

For the multifunctional composite structure in this work, the combined effect of unidirectional CFRP lay-up and copper mesh layer placement within the lay-up must be considered to understand the predicted shielding effectiveness. By modeling the structure to predict shielding effectiveness, more efficient design of the structure can be achieved by theoretically determining the optimum configuration rather than relying on fabrication and experimental testing of each individual configuration. To simplify the model, the CFRP layers can be modeled as homogenous materials with anisotropic electrical properties^{91,94,95}. The relevant material properties are the electrical conductivity, permittivity, and magnetic permeability, which are used to calculate the electric field by Maxwell's equations, from which the shielding effectiveness can be calculated. The copper mesh layer can be represented in the model using a sheet impedance boundary condition that uses the geometry and material properties of the mesh in the analytical expression for sheet impedance of a wire mesh screen⁹⁶. By combining the SE ability of the CFRP laminate and copper mesh into a unified model, the

effect of CFRP lay-up and copper mesh layer placement can be investigated to determine the optimum configuration for maximum shielding effectiveness while minimizing weight.

1.9. Summary of Chapters

In this dissertation, Chapter 2 describes the experimental methods and characterization techniques used in this work. Chapter 3 describes the investigation of critical current density in covetics processing. Chapter 4 discusses the mechanical properties of AA-1350 3 wt% C covetics using nanoindentation. Chapter 5 presents the updates made to the processing system used to make covetics and results from samples made with the new system. Chapter 6 discusses micro-mechanical properties at the interface of matrix and fillers (carbon fiber, copper mesh) of multifunctional composites and how they relate to the manufacturing process. Chapter 7 describes the creation of a FEA model of SE for the multifunctional composite structure for different lay-ups and copper mesh layer placement. Chapter 8 summarizes the conclusions of the dissertation and discusses future work.

Chapter 2: Experimental Methods and Characterization Techniques

2.1. Covetic Sample Fabrication

To make covetic samples, AA-1350 cable with 1 cm diameter provided by General Cable was used as the metal matrix material, with as-received composition of 0.06 % Si, 0.16% Fe, 0.005% Mg, 0.002 % Cu, 0.004% Mn, 0.003% Cr, 0.002% Zn, balance Al. This alloy was chosen because of the higher purity, 99.764% aluminum. The carbon used was activated carbon nano-powder (US Research Nanomaterials, Inc.) with particle size of 100 nm. The starting materials were arranged in a cylindrical graphite crucible (GraphiteStore.com, Inc.) that was then placed in an induction furnace (RDO Induction LLC). The crucible had a 10 cm diameter and 10 cm height cavity in the center where the starting materials and processed covetic were held. The induction furnace was enclosed in a metal chamber with a hole on the top where the electrodes were inserted into the melt. A schematic of the enclosure is given in Figure 2.1. The furnace chamber was purged with 99% purity argon gas for one hour before starting the reaction, and argon flow was maintained during the reaction to limit carbon oxidation and aluminum oxide formation during processing. Temperature of the metal was monitored using an IR thermometer (OMEGA). A stirrer with a graphite impeller on the end of a stainless-steel rod was used to mix the carbon and aluminum together after the aluminum was melted. The starting material arrangement is depicted in Figure 2.2, where a “sandwich” of AA-1350 was made with activated carbon in the center. This configuration was chosen to limit the amount of carbon segregated to the surface of the sample, as the activated carbon was enclosed on all sides by the aluminum. To make the “sandwich,” first an aluminum disk was made by melting AA-1350 rods in the crucible with the induction furnace so that the disk had the same diameter (10 cm) as the crucible. Before

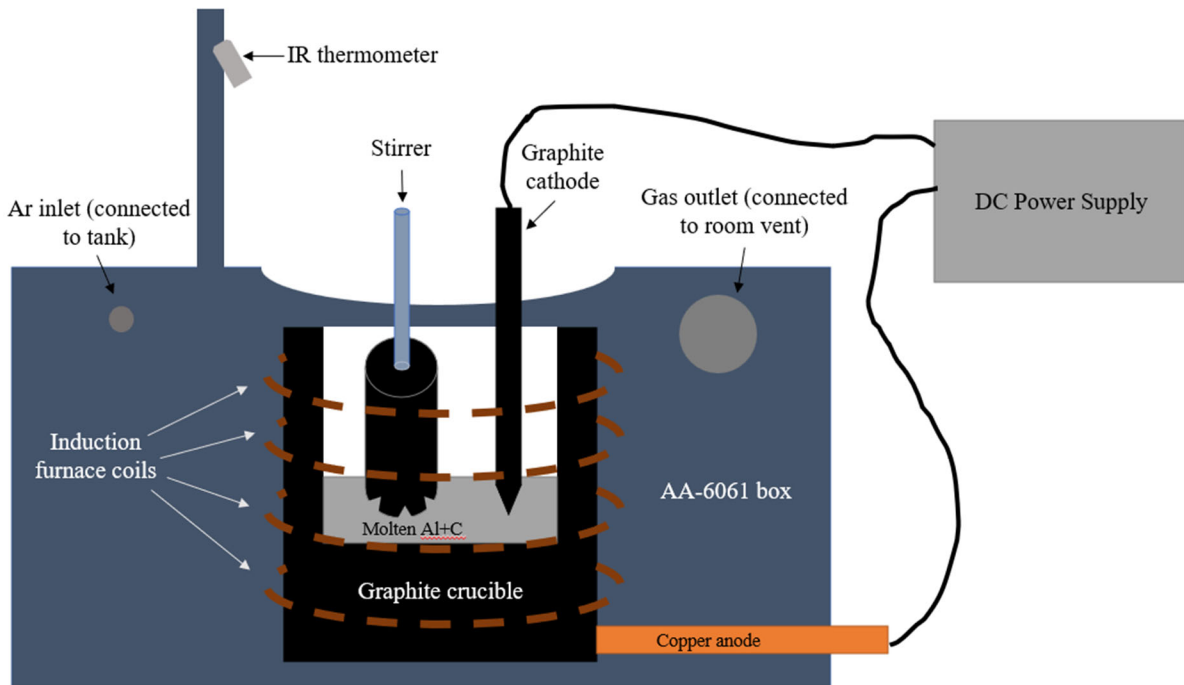


Figure 2.1. Schematic of processing system enclosed in an AA-6061 box. A hole is cut in the top of the box where the stirrer and graphite cathode are inserted. The stirrer is mounted to an AA-6061 frame on the front of the enclosure and the graphite cathode is connected to a robotic arm on the back of the enclosure, similar to how the IR thermometer is mounted to a frame on the left side of the enclosure. The induction coils wrap around the graphite crucible that contains the molten starting materials. The Ar inlet is connected to the Ar tank (not pictured) by PVC tubing, and the gas outlet is connected to the room's vent by metal exhaust tubing.

melting, to remove any potential contamination, the surfaces of the rods were abraded with 180 grit SiC paper followed by sonication in dish detergent and water for 5 minutes followed by sonication in acetone twice for 5 minutes each. After the 10 cm diameter aluminum disk was solidified, it was sawed in half in the transverse direction and the cleaning procedure was repeated. The outer ring of the “sandwich” consisted of short (~2 cm) chopped AA-1350 rods that were lined up adjacent with each other around the edge of the crucible, with the two halves of the aluminum disk on the top and bottom and activated carbon placed in the center (Figure. 2.2). All the aluminum (disks and rods) was weighed, and 3 wt. % activated carbon was nominally added.

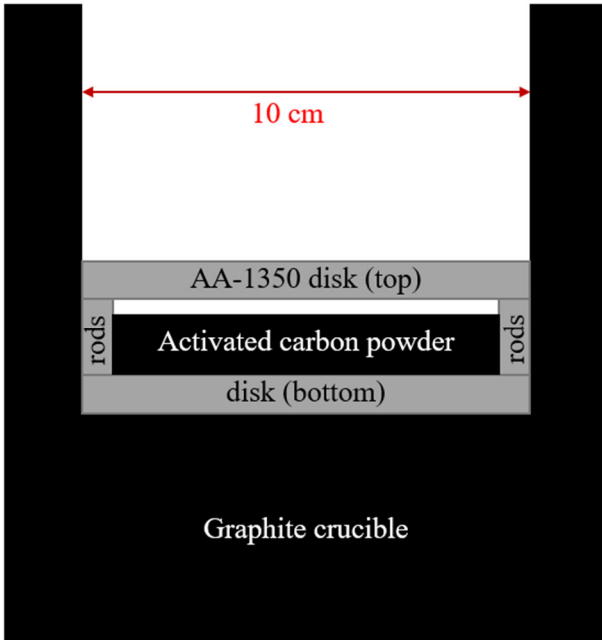


Figure 2.2. AA-1350 and activated carbon starting material arrangement inside the graphite crucible.

The covetics process involves applying a direct current to a mixture of the molten AA-1350 and activated carbon, which is believed to induce crystallization of the carbon into graphitic sheets. The temperature during the reaction was in the range of 730-750°C, above the melting temperature of aluminum but below 900°C, the temperature where formation of Al_4C_3 occurs⁹⁷. The applied current ranged from 100-250A, which resulted in voltages of about 1-10 V,

depending on the electrode used. The direct current (DC) power supply was controlled by LabView with a feedback loop to adjust the voltage in order to keep the current constant. The anode was the graphite crucible with a copper rod screwed into the side of the crucible and connected back to the DC power supply with welding cables, and the cathode was a graphite rod inserted into the melt from above, also connected via a copper rod and welding cables to the DC power supply.

Once the aluminum was completely melted, before applying the current, the mechanical stirrer with a graphite impeller was introduced and the aluminum-carbon mixture was stirred for five minutes to help homogeneously distribute the carbon throughout the molten aluminum. Typically, the stirring was continued during the application of current to maximize homogeneity of carbon throughout the final sample; however, in the critical current density investigation stirring was stopped during application of current to understand the effect of position relative to

the electrode (and subsequently, local current density during processing) on the formation of graphitic carbon. After application of the current for 1000 s, or 16.67 minutes, the furnace was powered off and the sample was allowed to cool in the crucible, typically taking 10-15 minutes to solidify. To make the baseline samples, an equivalent mass of AA-1350 was melted in the crucible and subjected to the same thermal treatment; however, no carbon was added, and no current was applied to the molten mixture.

Two types of cathodes were used, which produced different spatial current density distributions. A solid graphite rod tapered to a point was used in most cases, which produced a higher current density that was localized near the surface of the melt and sharpened tip. For the critical current density investigation, a copper rod with a graphite tip on the end inserted into the melt was used, which produced a lower but more evenly distributed current density along the electrode surface.

2.2. Machining Samples for Characterization

To prepare samples of suitable size for microscopy, small sections (~1x3x0.3 cm) were machined from the larger cast sample that solidified in the graphite crucible after the covetics process. The 10 cm diameter x 3 cm tall cast sample was first cut using a band saw to expose the interior of the covetic sample by making two parallel cuts spaced ~1 cm apart across the diameter of the cast and through the entire thickness. This 1x3x10 cm rectangular specimen was then sliced using a low-speed diamond saw to take a thinner 1 cm x 3 cm x 0.3 cm from the center of the cast sample. A diagram of the sample sectioning is given in Figure 2.3. Sectioned samples were polished using a sequence of progressively finer Al₂O₃ lapping paper (30 μm, 12 μm, 9 μm, 5 μm, 3 μm, 1 μm, 0.3 μm) followed by 0.05 μm colloidal silica suspension to produce a smooth surface for microscopy and further testing. The colloidal silica and any other

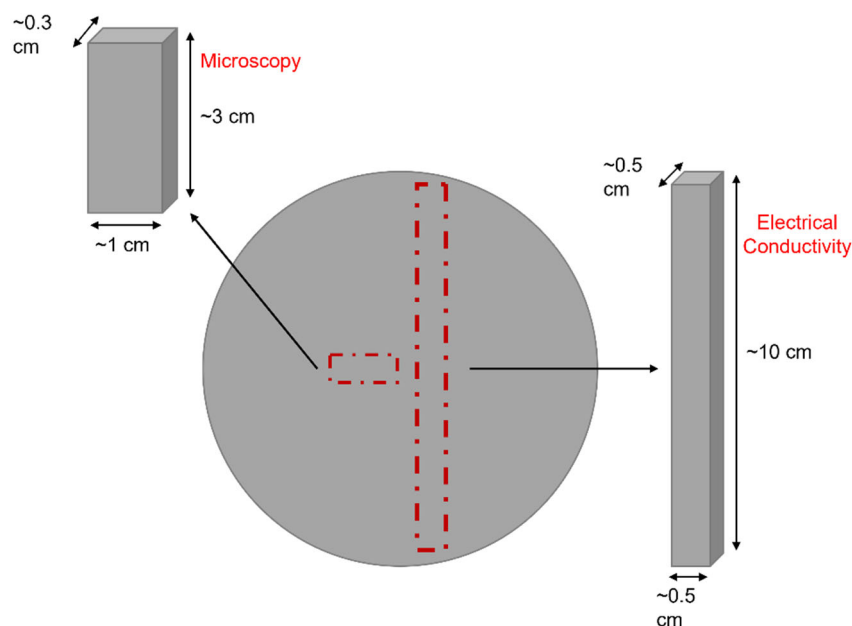


Figure 2.3. Top-down view of the cast covetic sample showing where microscopy and electrical conductivity samples were sectioned from.

polishing residues were cleaned off the sample surface by using Final A polishing pads in the absence of abrasives using a mixture of dish detergent and water as a lubricant/cleaning solution. All polishing materials were obtained from Allied High-Tech Products, Inc.

Samples were then sonicated twice in acetone for 5 minutes to remove any remaining polishing residues or surfactant films.

To prepare samples for electrical conductivity, a cut along the diameter of the 10 cm by 3 cm tall cast sample was made to expose the interior of the specimen. For electrical conductivity measurements, a higher aspect ratio sample gives a more accurate electrical conductivity measurement as the current flows longitudinally through the specimen in the four-point probe measurement used, described in greater detail in Section 2.7. Additionally, increased precision of the cross-sectional area improves precision of the electrical conductivity measurement. Thus, a 10 cm long specimen with a ~0.5 cm x 0.5 cm square cross-sectional area was machined by milling into the face of the exposed interior of the specimen, shown in Figure 2.3. Using a milling technique to machine a rectangular rod for electrical conductivity measurements provides greater dimensional control than using a saw. The cross-sectional area dimensions were

measured at 5 points along the length of the specimen to use in the electrical conductivity calculations.

For the critical current density measurement, the goal was to measure the electrical conductivity in two points: the area close to the electrode where there is a high current density, and an area ~ 1 cm from the electrode where the current density is lower. In this instance, the sample for electrical conductivity were machined so that the long dimension was 3 cm, the height of the cast specimen, and the cross-sectional dimensions were ~ 5 mm x 5 mm.

For the multifunctional CFRP with copper mesh composite samples, a ~ 1.5 cm x 1.5 cm section was cut from the laminate, with thickness of ~ 2 mm. Cross-sectional samples were prepared by mounting the sample in QuickSet Acrylic (Allied High Tech) and grinding with 320 grit SiC paper to expose the sample through-thickness. The sample was polished sequentially with 600 grit SiC paper, 1200 grit SiC paper, 1 μm Al_2O_3 slurry, and 0.05 μm colloidal SiO_2 . . The colloidal silica and any other polishing residues were cleaned off the sample surface by using Final A polishing pads in the absence of abrasives using a mixture of dish detergent and water as a lubricant/cleaning solution. The samples were then cleaned by sonicating in a mixture of dish detergent and water for five minutes, two times.

2.3. COMSOL Multiphysics Software

COMSOL Multiphysics Software V.6.0 was used to model the current density, voltage, and electric field around the two different electrode geometries in the covetics process and the shielding effectiveness of CFRP laminates with an added copper mesh layer. For the covetics project, the electrodes were modeled using the AC/DC module with the Electric Current interface. This interface solves a current conservation problem using Ohm's Law. For the project studying the CFRP with copper mesh multifunctional composite, the shielding effectiveness

model was made using the RF module with the Electromagnetic Waves, Frequency Domain interface. This interface solves the time-harmonic Maxwell's equations to calculate the electric field propagation through the sample.

2.4. Raman Spectroscopy

Raman spectra were collected using a Horiba LabRAM ARAMIS confocal Raman microscope equipped with a 532 nm laser for the covetic samples and a 633 nm HeNe laser for the multifunctional CFRP with Cu mesh composite samples. The mapping feature was used to collect 10 μm x 10 μm maps on the polished covetic sample surface with a step size of 1 μm , giving 121 spectra total per map. Ten maps were taken from ten different areas of each sample, resulting in 1210 spectra collected per sample, corresponding to approximately $10^3 \mu\text{m}^2$ total surface area sampled per specimen. For the CFRP w Cu mesh samples, 30 spectra were collected at various points on the sample surface. The laser spot size was 721 nm, calculated as an airy disk from the expression $1.22\lambda/\text{NA}$ where $\lambda=532$ or 633 nm is the laser wavelength and $\text{NA}=0.9$ is the numerical aperture of the 100X objective lens used in this study.

2.5. Scanning Electron Microscopy (SEM), Energy Dispersive Spectroscopy (EDS) and Electron Backscatter Diffraction (EBSD)

SEM imaging was performed using a Tescan GAIA3 FEG-FIB/SEM with EDAX EDS and EBSD detectors at an accelerating voltage of 10 kV in secondary electron mode. $\sim 15 \mu\text{m}$ x $15 \mu\text{m}$ EDS maps were collected using EDAX TEAM Enhanced V4.4.1 software to measure the elemental distributions around features of interest identified by Raman, usually areas that showed increased graphitic carbon crystallite size or grain boundaries to identify secondary phases, such as Al-Fe-Si. The accelerating voltage was increased to 20 kV during EDS map

collection to increase the depth of the sample area and to excite elements with X-rays at higher energy.

EBSD maps were collected using a 20 kV accelerating voltage and a step size of 0.45 μm . The sample was mounted at an angle of 70° with respect to the electron beam to maximize diffracted electron signal to the detector. EDAX TEAM Enhanced V4.4.1 software was used to obtain results and generate maps of the crystallographic orientation of aluminum grains on the surface of the sample. Post-processing was performed in OIM Analysis V8 software by setting a 15° grain tolerance angle, minimum grain size of 5 pixels and specifying that a grain must contain pixels from more than one row.

2.6. Transmission Electron Microscopy (TEM)

The sample for TEM was prepared using Focused Ion Beam (FIB) in the Tescan GAIA3 FEG-FIB/SEM with an OmniProbe 400 port-mounted piezo nanomanipulator. An area that showed increased graphitic carbon crystallite size by Raman scattering was located with SEM, and FIB was used to extract a small cross-sectional sample from the area, $\sim 5 \mu\text{m}$ along the surface by $5 \mu\text{m}$ deep into the surface. A 2 kV Ga^+ beam was used to reduce the sample thickness to $\sim 100 \text{ nm}$ so that it would be suitable for TEM analysis (electron transparent) with minimal residual damage from the FIB process. Bright field TEM images and electron diffraction patterns were obtained using a JEOL JEM 2100F field emission TEM operated at 200 kV with a spherical aberration coefficient, C_s , of 0.5 mm, lattice resolution of 0.14 nm and point-point resolution of 0.19 nm.

2.7. Four Point Probe Electrical Conductivity

The four-point probe method was used to calculate the electrical conductivity of the samples. In this method, four probes are placed in a line along the length of the sample. A

current is passed through the outer two probes, and the voltage is measured between the inner two probes to calculate the resistance. The conductivity of the sample is given by

$$\sigma = \frac{L}{R \cdot A} \quad (2.1)$$

where R is the resistance measured, A is the cross-sectional area of the material being tested and L is the distance between the two inner probes. The average resistance was calculated from five I-V sweeps, the length and area were measured using digital calipers and the average cross-sectional area was calculated from five measurements along the length of the sample.

The conductivity in S/m is converted to % IACS by normalizing to 5.8×10^7 S/m, the standard value of electrical conductivity for copper⁶³. Electrical grade AA-1350 should have a conductivity of 62% IACS, i.e., 62% of the conductivity of copper³¹.

2.8. Nanoindentation and Electrical Contact Resistance

Local mechanical properties of covetics and CFRP laminates with added Cu mesh layers were measured by nanoindentation using a Hysitron TI 950 TriboIndenter. The instrument indents a small diamond tip into the sample surface while measuring force and displacement, which can be used to calculate reduced elastic modulus, E_r , and hardness, H, of small areas. The instrument uses a three-plate capacitive transducer with a load resolution of 1 nN and 0.04 nm displacement resolution. The diamond tip was assumed to have an elastic modulus of 1140 GPa, a Poisson's ratio of 0.07, and a radius of curvature of 150 nm for modulus and hardness calculations. For nanoindentation on covetics, a Berkovich tip geometry was used, which is a self-similar three-sided pyramid with 142.35° total included angle and 65.35° half angle, ground to a 150 nm radius tip. For nanoindentation on CFRP laminates with added copper mesh layers, the diamond tip geometry was cono-spherical with a total included angle of 60° and radius of curvature of 350 nm.

Scanning probe microscopy (SPM) images can be generated by rastering the tip over the sample surface using the piezo-scanner. This allows for SPM imaging of the sample surface before and after indenting with +/- 20 nm resolution in the x and y directions, and +/- 0.4 nm resolution in the z direction and also for precise positioning of the tip for indentation testing. The Hysitron software can be used to program the instrument to perform arrays of multiple indents with a user-specified number of indents and indent spacing.

To perform indents that tested a larger volume of material, the high load transducer and stage (Bruker) were used on the covetic samples. The maximum normal load of the high load transducer is 2.8 N, compared to 10 mN for the standard transducer and stage which allowed for deeper indents. The diamond tip used had Berkovich geometry.

Electrical contact resistance (ECR) measurements were also performed on covetic samples. In this technique, a boron-doped conductive diamond Berkovich tip was used instead of the standard un-doped diamond tip, and a nanoECR sample stage (Bruker) was used that acts as an electrode. A voltage was applied between the transducer and the sample stage, and the current flow through the tip was measured. The difference in current flow measured is predominantly due to the change in contact resistance at the tip-sample interface, thus the electrical properties of different areas of covetic samples could qualitatively be assessed⁹⁸.

Chapter 3: Covetics Critical Current Density Investigation

3.1. Motivation and Objectives

The covetics process uses a DC current to induce the rearrangement and crystallization of activated carbon, the starting material, into graphitic sheets and/or ribbons within the molten metal. The resulting material has enhanced electrical, thermal, and mechanical properties that are believed to be related to the graphitic carbon structure that forms as a result of the covetics process⁴¹. To measure this, Raman spectroscopy has been used to calculate graphitic carbon crystallite size before and after processing, which provides information about how the carbon structure changes due to the application of current. Prior work by Ge et al. established that there was a positive correlation between the electrical conductivity and graphitic carbon crystallite size; however, there were large standard deviations in crystallite size measured (on the order of ~50% of the mean crystallite size value)⁴⁴. This indicates that there is some rearrangement of the starting activated carbon to locally increase crystallite size in some areas, but to differing extents in different areas of the sample, with some areas showing the same crystallite size as that of activated carbon prior to the application of current (8-10 nm). Consequently, if graphitic carbon crystallite size could be further increased throughout a larger volume of the covetic material, there could be a greater increase in electrical conductivity and other material properties.

Understanding the current density threshold and residence time required for rearrangement and crystallization of graphitic carbon from activated carbon would improve the ability to engineer the reactor such that the entire molten mixture is exposed to sufficient current density for sufficient time during processing. In the prior works by Ge et al.^{41,44}, a graphite electrode in the form of a 1 cm diameter rod with a pointed tip was used, and the molten mixture

was stirred during the application of current with the expectation that the entire volume of the melt was exposed to the high current density region around the electrode during processing. In practice, however, the presence of activated carbon in the final covetic sample that did not show an increase in crystallite size indicates that either the magnitude of current density was insufficient and/or the residence time of carbon in the high current density region was insufficient to cause crystallization and an increase in crystallite size in all areas of the covetic sample. Therefore, if the current density and residence time required to induce crystallization of graphitic carbon from the activated carbon starting material were known and achieved during covetics processing, the graphitic carbon crystallite size in the sample could increase throughout the entire covetic sample and, subsequently, show a greater improvement in the electrical conductivity.

3.2. Sample Fabrication

To understand the relationship between local current density and graphitic carbon structure, a 3 wt.% C AA-1350 covetic sample was made following the procedure outlined in Section 2.1 without stirring during the application of current. A current of 250 A was applied in current control mode for 1000s (16.67 minutes), resulting in a voltage of ~1 V, shown in Figure 3.1.A. The temperature during application of the current was 732-743° C, shown in Figure 3.1.B. The induction furnace power was lowered during the application of current to prevent excessive heating of the melt due to Joule heating of the graphite electrode.

The lack of stirring enabled the evaluation of crystallite size in two distinct regions of the sample: the high current density (25 A/cm²) region around the electrode and the lower current density region (5 A/cm²) away from the electrode. The copper-graphite electrode used was designed so that there was a relatively uniform current density on the electrode surface,

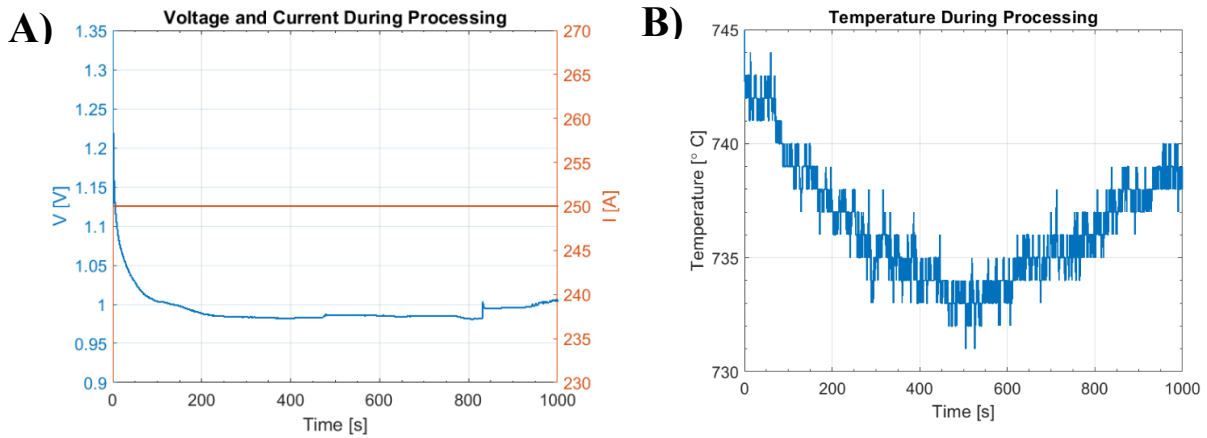


Figure 3.1. A) Voltage and current during covetics processing. The DC power supply was operated in current-control mode. B) Temperature during the application of current

compared to the pointed graphite electrode typically used that showed a higher but more localized current density when modeled in COMSOL (discussed in Section 2.1).

The copper-graphite electrode was a 1 cm diameter copper rod with a graphite tip on the end, shown in Figure 3.2, where $r=0$ cm indicates the radial axis of symmetry. The graphite tip was a hollow

cylinder ~3 cm tall that was screwed onto the end of the copper rod by machining threads onto each component. The inner diameter of the graphite was 1 cm to

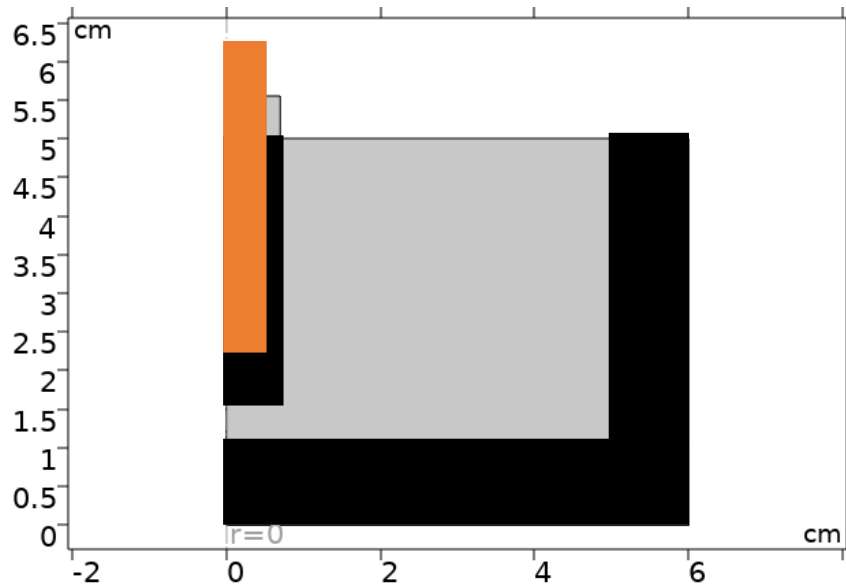


Figure 3.2. Diagram of the covetics processing apparatus with $r=0$ cm indicated the radial axis of symmetry. The orange area represents the copper electrode, the black areas indicate the graphite tip and crucible, and the gray area indicates the molten mixture of AA-1350 and activated carbon.

match the diameter of the copper rod, and the outer diameter was 1.3 cm.

3.3. COMSOL Model of Current Density, Voltage, and Electric Field in the Covetics System

COMSOL Multiphysics Software V.6.0 AC/DC module was used to model a simplified version of the covetics system to estimate the voltage and current density using the Electric Currents physics interface. The electrode (orange region in Figure 3.2) was set as a 250 A terminal in the model, and the graphite crucible was set as the ground. The current density, voltage, and electric field throughout the system were calculated. The results of the simulation for 250 A are shown in Figure 3.3, with Figure 3.3.A. showing the radial symmetry of the current density distribution. The region surrounding the electrode experiences a current density of ~ 25 A/cm² on the surface of the electrode that decreases exponentially as radial distance from the electrode increases, shown in Figure 3.3.B. A 2D slice of the current density model in Figure 3.3.C. shows a higher current density of ~ 40 - 50 A/cm² concentrated at the electrode-molten Al+C-air interface, and a lower current density of ~ 5 A/cm² at the bottom corner of the electrode. However, these regions were considered small relative to the rest of the electrode-molten Al+C interfacial region that had a current density of ~ 25 A/cm². The voltage and electric field throughout the sample are shown in Figure 3.4. It can be seen in Figure 3.4.A, that there is a higher potential in the graphite tip of the electrode (176.5 mV), but that the voltage in the aluminum is much lower (35.5 mV) and fairly constant throughout the aluminum in both the r and z directions, shown in Figure 3.4.B and 3.4.C. The electric field throughout the system is shown in Figure 3.4.D. It is low within the aluminum domain, with a maximum of 4.6 mV/m near the electrode decaying to 0.3 mV/m near the crucible wall, shown in Figure 3.4.E. The electric field through z at a given radius is nearly constant, shown in Figure 3.4.F.

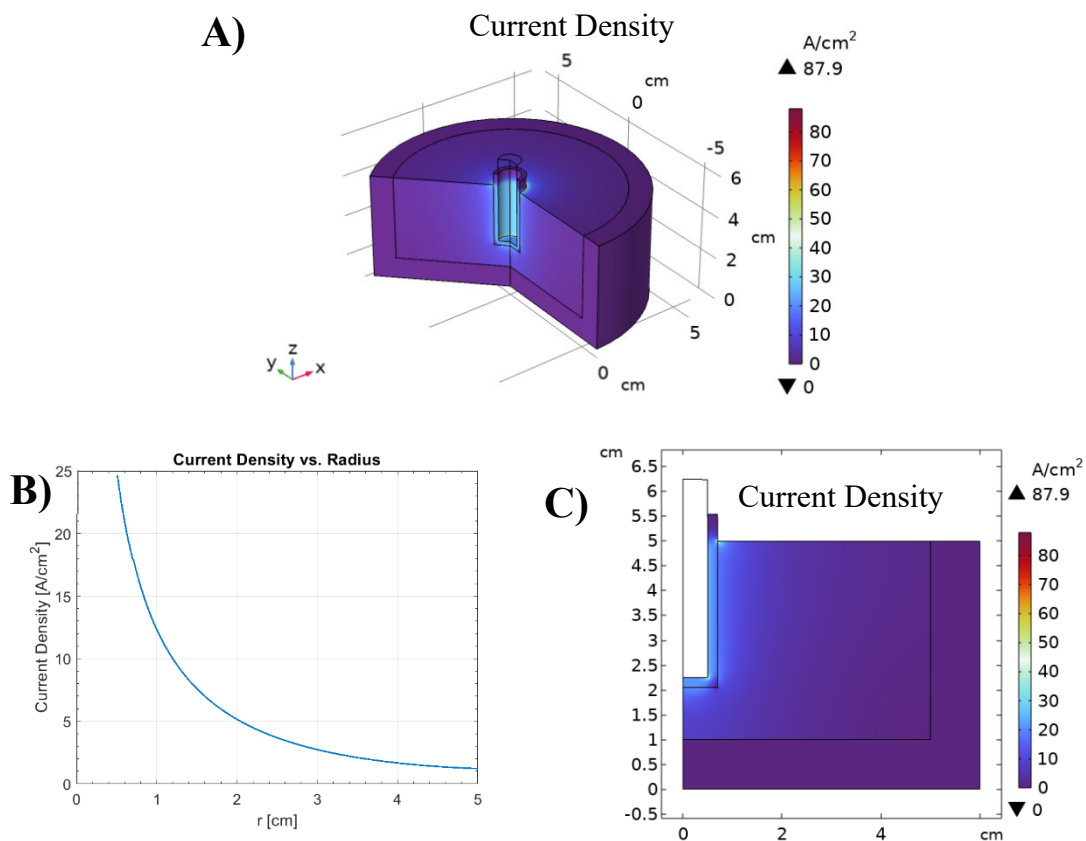


Figure 3.3. A) COMSOL model of the current density distribution for the Cu-C electrode throughout the covetics system, B) Current density as a function of radial distance at $z=3.5$ cm, C) 2D slice showing the current density through a cross-section of the covetics system

In this experiment, the Cu-C electrode was used because it produced a relatively uniform current density on the electrode surface, which allowed for better correlation between local current density and structure/properties. However, in most other covetic samples a pointed graphite electrode was used which produced a higher but less uniform current density on the electrode surface. For comparison, the current density, voltage, and electric field calculated for the pointed graphite electrode are presented in Figure 3.5. It can be seen from the line plots at $z=3.5$ cm for current density, electric potential, and electric field shown in Figure 3.5.B, 3.5.D, and 3.5.F, respectively, that the result is similar to that of the Cu-C electrode. The current density is highest at the electrode-aluminum interface at 24 A/cm^2 and decays with radial distance. The

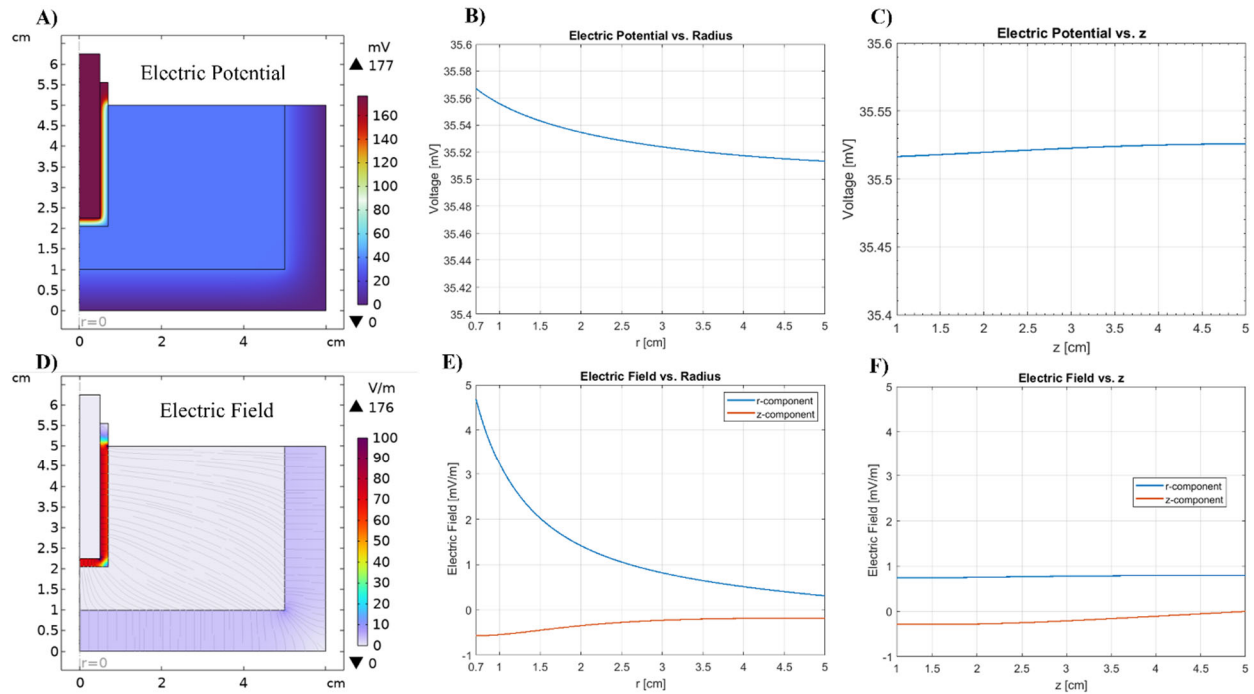


Figure 3.4.A) COMSOL model of the electric potential for the Cu-C electrode, B) voltage as a function of radius at $z=3.5$ cm, C) voltage as a function of z at $r=3$ cm, D) electric field distribution showing a high field region confined to the graphite tip of the electrode, E) radial and z component of electric field as a function of radius at $z=3.5$ cm, and F) radial and z component of the electric field as a function of z at $r=3$ cm.

voltage is fairly constant throughout the aluminum at 35.5 mV. The maximum electric field is only 6.4 mV/m near the electrode, which decays to 0.3 mV/m near the crucible edge. A notable difference is that while the current density trend at $z=3.5$ cm shown in Figure 3.5.B is nearly equal to that of the Cu-C electrode shown in Figure 3.3.B, it can be seen in Figure 3.5.A that there is a region of higher current density at ~ 100 A/cm² localized to the region at the pointed tip and corner of the electrode which does not occur in the Cu-C electrode model.

3.4. Sample Sectioning

A diagram of how specimens for characterization were machined from the cast sample is shown in Figure 3.6. The 10 cm diameter cast covetic was sectioned such that the high current density (25 A/cm²) region at $r=0$ cm, where the electrode was inserted, could be compared to an area of the sample at $\sim r=1$ cm from the electrode where the current density was ~ 5 A/cm².

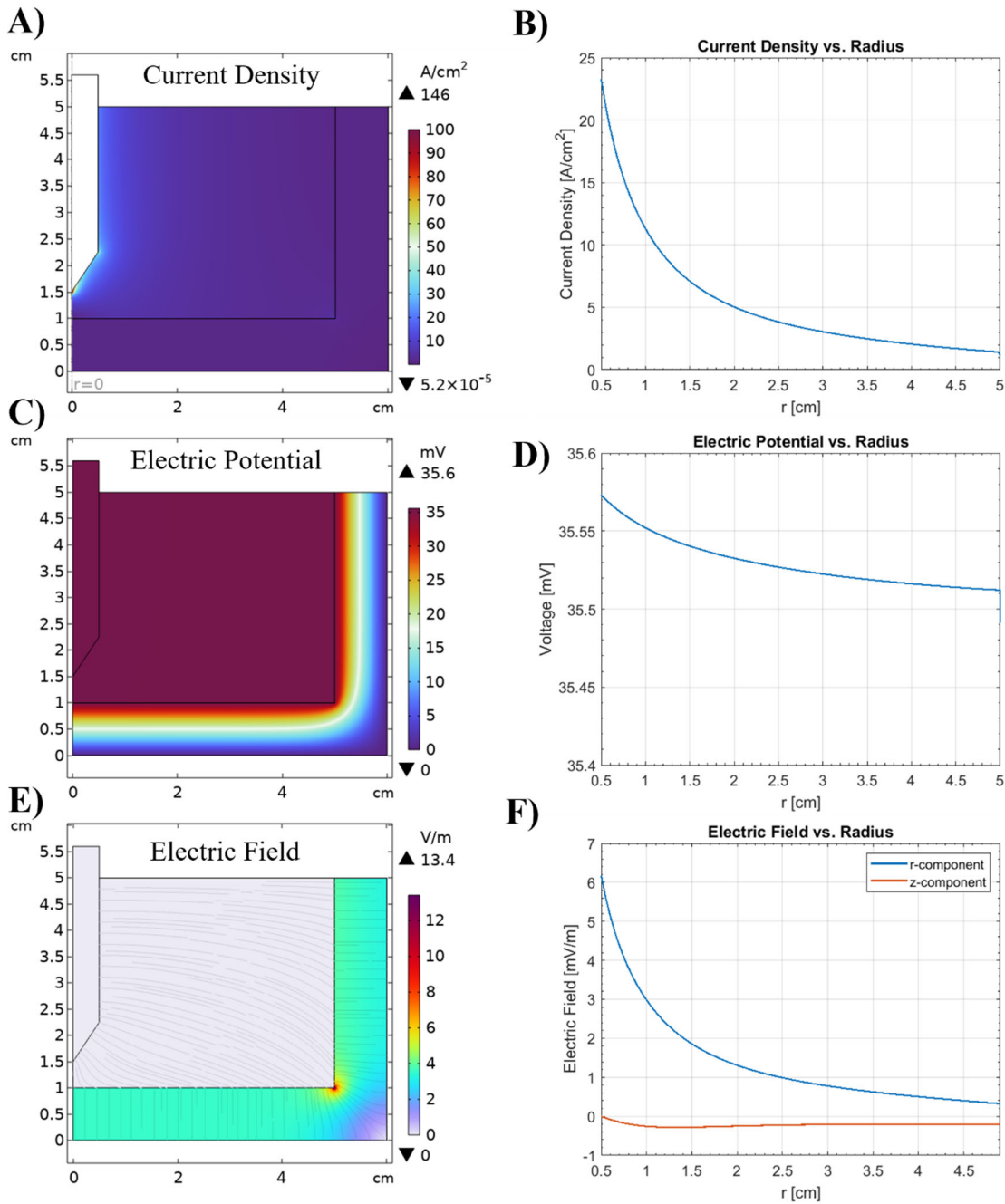


Figure 3.5. COMSOL model of the pointed graphite electrode showing A) current density through the system, B) current density as a function of radius at $z=3.5$ cm C) electric potential, D) voltage as a function of radius at $z=3.5$ cm, E) electric field distribution and F) Radial and z component of electric field as a function of radius at $z=3.5$ cm.

Additionally, the samples for Raman spectroscopy (green in Figure 3.6.) and electrical conductivity (purple in Figure 3.6.) were sectioned from areas directly adjacent to each other so that a relationship between graphitic carbon crystallize size measured by Raman and electrical

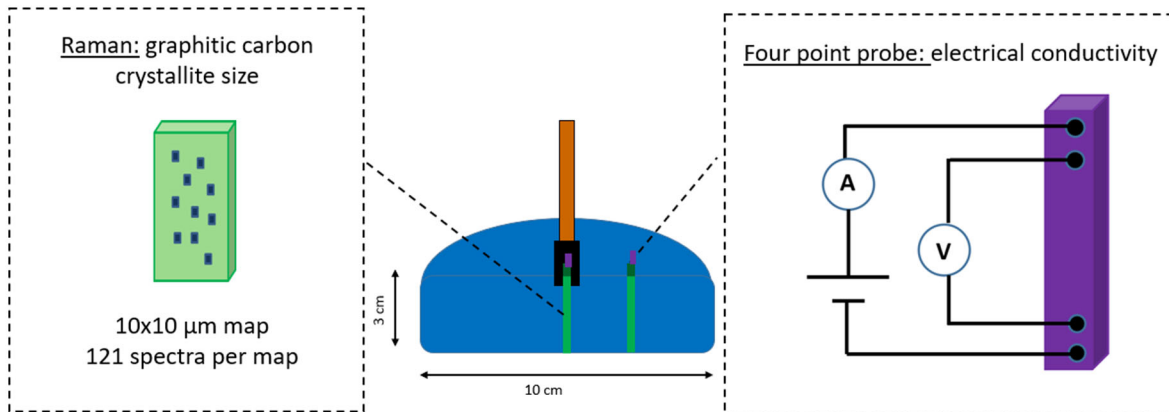


Figure 3.6. Diagram of where in the cast covetic samples for Raman spectroscopy and electrical conductivity were taken in the critical current density investigation. $R=0$ cm is in the high current density region (25 A/cm^2) near the electrode and $r=1$ cm is in a lower current density region (5 A/cm^2) away from the electrode.

conductivity could be established. Ideally both the graphitic carbon crystallite size and electrical conductivity would have both been measured from the same sample, however different dimension requirements for each of the characterization methods necessitated two separate samples. Thus, the graphitic carbon crystallite size and electrical conductivity in the covetic sample were both measured in two distinct areas: the region directly surrounding the electrode, $r=0$ cm, that experienced $\sim 25 \text{ A/cm}^2$ during processing and the region away from the electrode, $r=1$ cm, that experienced $\sim 5 \text{ A/cm}^2$ during processing.

3.5. Raman Spectroscopy

Ten $10 \mu\text{m} \times 10 \mu\text{m}$ maps of Raman spectra were collected from the covetic samples at $r=0$ cm and $r=1$ cm. Graphitic carbon crystallite size by the Tuinstra-Koenig relation was estimated from the Raman spectra maps⁹⁹. For sp^2 carbon, a double resonance process gives rise to characteristic G, D and 2D peaks whose position, shape and intensity are sensitive to defects¹⁰⁰. These effects can be used to track graphitization and amorphization processes¹⁰¹.

Notably, because the integrated intensity of the D peak at $\sim 1350 \text{ cm}^{-1}$ increases in the presence of defects, a quantitative method of estimating graphitic carbon crystallite size has been developed

that uses the integrated intensity ratio of the G peak at $\sim 1584 \text{ cm}^{-1}$ to the integrated intensity of the D peak at $\sim 1350 \text{ cm}^{-1}$ ⁹⁹. The relation has been improved upon by establishing standardized fitting procedures and accounting for laser wavelength¹⁰². The formula for graphitic carbon crystallite size in the basal plane, L_a , in nm is given by

$$L_a = (2.4 \times 10^{-10}) \lambda_l^4 \left(\frac{I_D}{I_G} \right)^{-1} \text{ [nm]} \quad (3.1)$$

where λ_l is the laser wavelength in nm (532 nm for this work), I_D and I_G are the integrated intensities of the D peak and G peak, respectively.

To calculate integrated intensity, Raman spectra were fitted in MATLAB using a deconvolution tool with an unconstrained non-linear iterative curve fitting procedure¹⁰³. After curve fitting, an exclusion rule was applied to filter out spectra that did not correspond to graphitic carbon. Any spectra with $R^2 < 0.5$ were excluded from calculations of crystallite size. Secondly, any spectra that had both $R^2 < 0.9$ and $I_D/I_G > 2$ standard deviations above the median were excluded.

From the remaining fitted spectra, a histogram of crystallite size for all 10 maps on the sample was generated to determine the extent of graphitic carbon crystallization. The precursor activated C crystallite size was 7-10 nm as seen in Figure 3.7 A, so the covetic process should result in a larger crystallite size. It is worth noting that the crystallite size of the graphite used to make the crucible and electrode is 50-130 nm, shown in Figure 3.7 B, so it is possible that an observed increase in crystallite size could be contamination from the electrode and/or crucible. Thus, it is the combination of both increased graphitic carbon crystallite size and improved electrical properties that would indicate successful processing conditions.

At $r=0$ cm, the area that experienced a 25 A/cm^2 current density where the electrode was inserted into the melt, some Raman spectra showed increased graphitic carbon crystallite size. Some maps showed increased size for almost all spectra taken from that area, like the maps shown in Figure 3.8 that had an average crystallite size of 22.3 ± 15.6 nm and 29.4 ± 12.2 nm, with optical micrographs showing the area where the Raman spectra were collected from. However, there were more areas that showed negligible increase in crystallite size compared to the activated carbon starting material, like the one shown in Figure 3.9 that

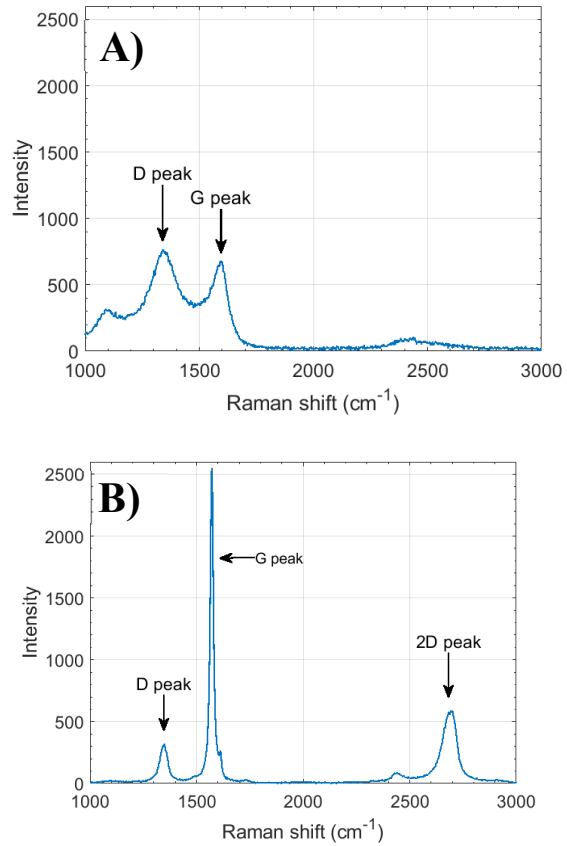


Figure 3.7. Reference Raman spectra for A) activated carbon used as the starting material and B) graphite used to make crucible and electrode

had an average crystallite size of 7.2 ± 1.7 nm. A histogram of the crystallite size for the region at $r=0$ cm is given in Figure 3.10, which shows that while there is some increase in graphitic carbon crystallite size, most spectra collected did not show an increase compared to the activated carbon starting material that had a crystallite size of 7-10 nm. This indicates that the current density of 25 A/cm^2 in the $r=0$ cm region around the electrode induced some rearrangement and crystallization of the graphitic carbon. However, the small fraction of carbon showing increased graphitic carbon crystallite size relative to the amount of activated carbon with no increase in crystallite size that is still present in the sample after current application indicates that either the magnitude of current density was insufficient to crystallize an appreciable amount of graphitic

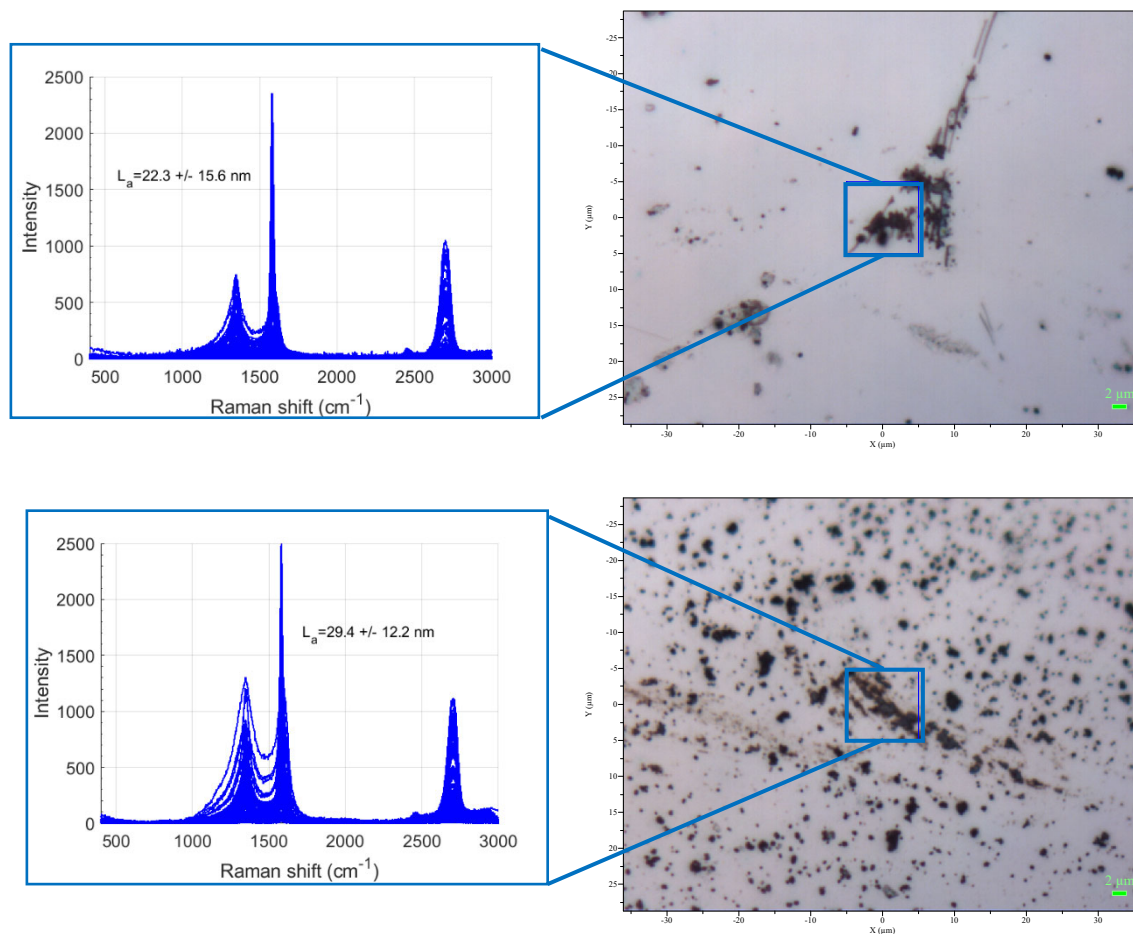


Figure 3.8. Left: Raman spectra collected from $r=0$ cm section that showed an increase in crystallite size of the carbon, and Right: Optical images showing the regions where the Raman spectra were obtained.

carbon for this duration of time (1000s, 16.67 minutes), and/or the high current density region was too localized such that there was not an appreciable volume of material that experienced the high current density necessary for carbon rearrangement and crystallization to occur.

At $r=1$ cm, away from the electrode where the current density was 5 A/cm^2 , there was no evidence of graphitic carbon found in the sample. Increased graphitic carbon crystallite size was typically found in the areas that appeared dark in the optical micrograph; however, the darker areas in the $r=1$ cm specimen did not show the G and D peak Raman signals that are characteristic of graphitic carbon. Some examples of Raman spectra from the $r=1$ cm sample

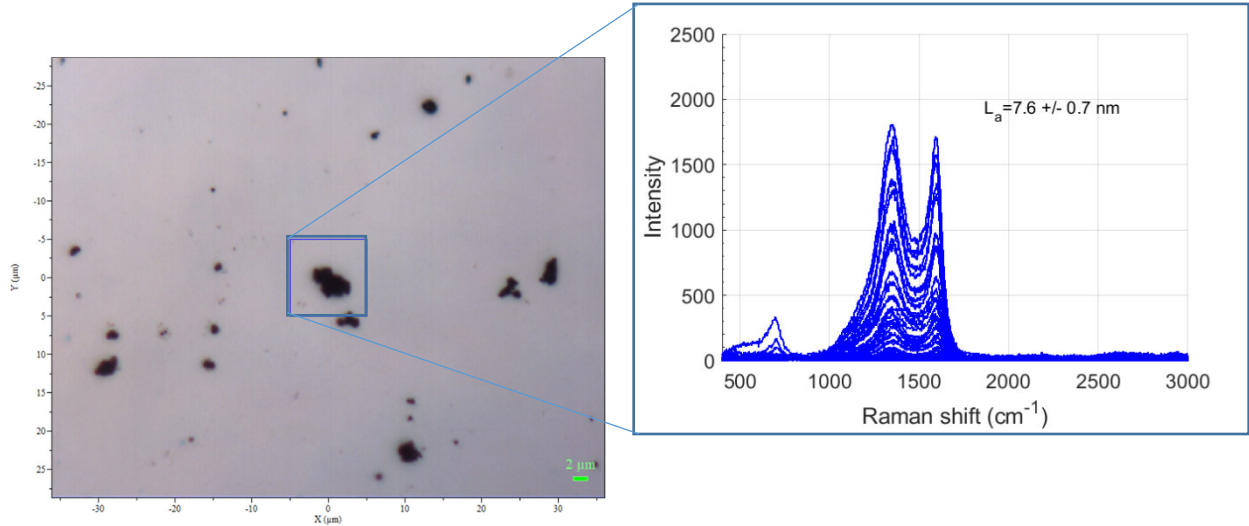


Figure 3.9. Raman spectra (right) collected from an area at $r=0$ cm (left) with crystallite size comparable to activated carbon

from dark areas are shown in Figure 3.11. The dark areas in the micrograph in Figure 3.11 were identified as Al-Fe-Si intermetallic phases by EDS mapping, and did not contain carbon, discussed in Section 4.3. These dark regions containing intermetallic compounds were usually found at grain boundaries.

3.6. Four Point Probe Electrical Conductivity

The electrical conductivity was measured in four areas by the four-point probe method, from the $r=0$ cm and $r=1$ cm areas in both the baseline and covetic samples, following the procedure described in Section 2.4. The baseline sample was subjected to the same melting and re-solidification process in the crucible; however, carbon was not added, and a current was not applied.

The electrical conductivity measurements at $r=0$ cm and $r=1$ cm are shown in Figure 3.12. The electrical

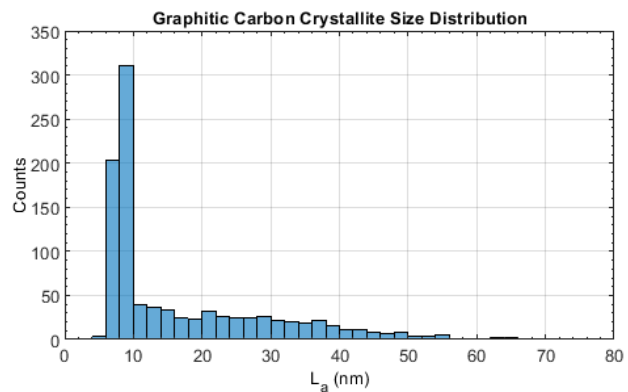


Figure 3.10. Histogram of crystallite size of the nanocarbon calculated for all 10 maps for the $r=0$ cm covetic sample

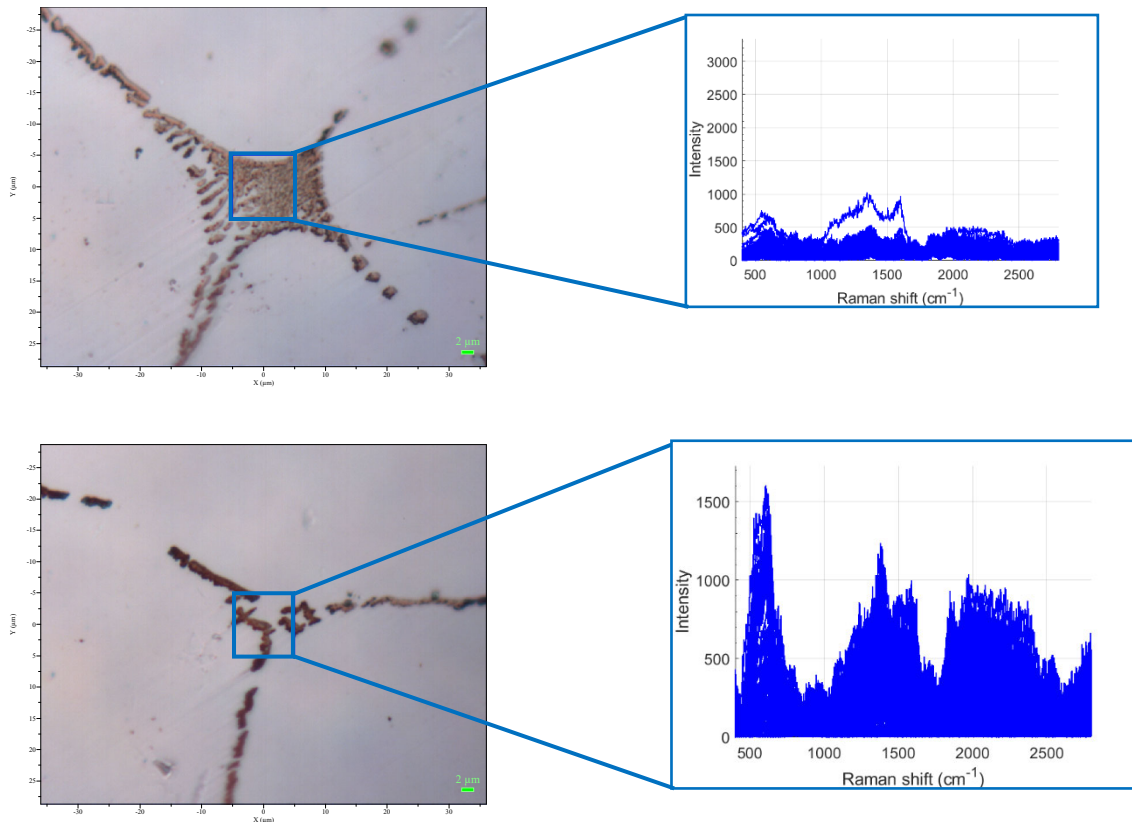


Figure 3.11. Raman spectra (right) from areas of the $r=1$ cm (left) that do not show the G and D peaks characteristic of graphitic carbon

conductivity of the covetic sample at $r=0$ cm was $59.9 \pm 0.2\%$ IACS (34.7 ± 0.1 MS/m), which was lower than the baseline sample at $r=0$ cm, $60.6 \pm 0.3\%$ IACS (35.2 ± 0.2 MS/m). This is consistent with the Raman results that showed there was no significant increase in crystallite size throughout the entire area of the covetic sample, despite some areas showing an increase in crystallite size. Additionally, the activated carbon that was still present in the sample after application of current could be a source of the decrease in electrical conductivity for the covetic sample. These results indicate that the 25 A/cm^2 current density on the electrode surface is not sufficient to produce a significant increase in graphitic carbon crystallite size to enhance electrical conductivity. Thus, it can also be concluded that the increase in graphitic carbon

crystallite size found by Raman at R=0 cm is not effective at increasing the electrical conductivity of the covetic sample.

In both the covetic and baseline samples, there is a slight ~2% decrease in electrical conductivity between r=0 cm and

r=1 cm, from 59.9 +/- 0.2% IACS (34.7 +/- 0.1 MS/m) to 58.5 +/- 0.2% IACS (33.4 +/- 0.1 MS/m) for the covetic and from 60.6 +/- 0.3% IACS (35.1 +/- 0.2 MS/m) to 59.4 +/- 0.3% IACS (34.5 +/- 0.2 MS/m) in the baseline. This could possibly be related to a thermal gradient during cooling and solidification, where the shape of the cylindrical crucible causes the center of the specimen to cool and solidify at a slower rate than the outer edges and top surface. This thermal gradient during cooling and movement of the solidification front from the outer edges of the sample to the interior results in changes in the local composition and microstructure of the cast metal at different radial positions that could potentially affect electrical conductivity. The variation is small, so it is reasonable to expect it could be a result of typical microstructural variation in the alloy.

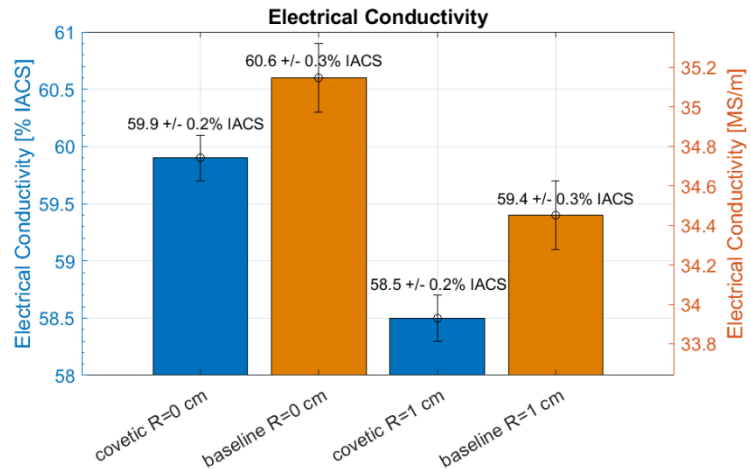


Figure 3.12. Electrical conductivity at r=0 cm and r=1 cm for the covetic and baseline samples

3.7. Discussion

3.7.1. AA-1350 Metallurgy

In addition to the application of current, the effect of thermal processing, i.e., melting and re-solidification, on AA-1350 with added carbon must be considered when interpreting the Raman scattering and electrical conductivity results. The fact that carbon was only detected in

the center of the cast covetic sample could potentially be explained by solute segregation as the metal solidifies. Carbon has low solubility in solid aluminum but is added in a relatively large quantity, 3 wt.%, to the system¹⁰⁴. The carbon is mechanically stirred into the molten aluminum before the application of current so that it is dispersed throughout the molten metal, but the carbon-aluminum mixture is thermodynamically unstable. Because the sample is not quenched, it can take up to 15 minutes for the covetic sample to completely solidify. As a result, the slow solidification rate could kinetically allow for solute rejection as carbon diffuses out of the newly formed solid phase into the liquid phase as the solidification front moves from the outer diameter to the center of the cylinder^{105,106}. Potentially, the carbon solute segregates to the center of the specimen, which solidifies last. This could potentially be one reason why there were both carbon that has increased in graphitic crystallite size and activated carbon that did not increase in crystallite size at $r=0$ cm, while carbon could not be detected in the $r=1$ cm sample that solidified before the $r=0$ cm sample. The diffusion coefficient of carbon in aluminum at 730°C, however, is quite low, $\sim 10^{-10}$ m²/s,¹⁰⁷ so other factors related to the electric potential, discussed in Section 3.7.2, may have also contributed to the high concentration of carbon at the center of the sample.

Along with the effects of carbon solute distribution in the metal, the relatively slow solidification rate of the covetic sample could affect the aluminum grain structure and local alloying element composition and microstructure in different areas of the cast. In a similar manner to the carbon solute, the local solute concentration of the alloying elements in AA-1350 (Si, Fe, etc) could be affected by the solidification process, where solute is rejected from the solid phase into the liquid phase where its solubility is higher¹⁰⁵. Solute can also segregate to the grain boundaries¹⁰⁸. Additionally, the size and morphology of solute precipitates could be affected by the local cooling rate, which could potentially cause differences in conductivity due

to the precipitates having lower conductivity than aluminum¹⁰⁶. Areas of the material that solidified more slowly (at $r=0$ cm) would also possess larger grains, and thus have higher electrical conductivity because the defects at grain boundaries add electrical resistance to the material¹⁰⁹. Any combination of these effects could have been the source of the decrease in electrical conductivity with radial position of the sample in the cast, seeing as the effect was also observed in the baseline sample that did not have carbon added.

3.7.2. Carbon Nanostructure Assembly Process

While the covetics process has typically been examined as a current-driven process^{26,27,41,44}, the observations in this work could potentially be better understood by considering the electric potential and fields present. Electrophoresis and dielectrophoresis are two examples of physical phenomena where particles migrate under the influence of an electric field. In electrophoresis, charged particles under the influence of a uniform electric field migrate as a result of surface charges between the particle and the medium, which is commonly used in analysis of biological specimens¹¹⁰. The clustering of carbon near the center of the specimen in covetics could potentially be explained by migration of charged carbon particles toward the electrode in the center of the sample.

In dielectrophoresis, under the influence of a non-uniform electric field, polarizable particles will experience a dielectrophoretic force that causes net movement of the particle¹¹¹. This phenomenon has been exploited to induce the assembly and rearrangement of nanoparticles¹¹²⁻¹¹⁵, with several authors using AC fields and reporting that the gradient of electric field has a significant effect on nanoparticle assembly. In the covetics process, a DC current has been used to attempt to induce self-assembly of graphitic, ideally graphene, sheets or ribbons within the molten metal. In this work, there was limited observation of graphitic carbon

that showed an increase in crystallite size. Potentially this could be due to the fairly low and uniform voltage throughout the Al+C mixture, shown in the COMSOL model discussed in Section 4.3. The applied current of 250 A used in this experiment was the maximum that the system could produce. It is possible that a different electrode configuration and/or higher applied current that produces a higher voltage and electric field could improve the ability of activated carbon to re-assemble into graphitic sheets or ribbons, as the electric fields in the current system are very small (~5-7 mV/m maximum). Oliveira et al.¹¹⁶ reported the formation of an electrically conductive network of carbon structures using a DC field, however a high dielectric perfluorocarbon (FC-40) medium was used for its high resistivity and high dielectric strength and, thus, ability to sustain high electric fields. In covetics processing, the medium is molten aluminum metal with low resistivity and dielectric constant, so it is not capable of sustaining a large electric field. This could potentially be why there was limited success using this DC method, as the electrophoretic force on the carbon particles in the molten aluminum was weak.

3.8. Conclusions and Future Work

The graphitic carbon crystallite size and electrical conductivity was measured in two regions of a 3 wt% C AA-1350 covetic sample: at $r=0$ cm where there is a current density of 25 A/cm² and $r=1$ cm where there is a lower current density of 5 A/cm². Graphitic carbon was found by Raman in the $r=0$ cm sample, with some areas showing increased crystallite size of 20-30 nm, while most areas showed a crystallite size of 7-10 nm, the same as the activated carbon starting material. In the $r=1$ cm sample, no evidence of graphitic carbon was found using Raman scattering. This segregation of carbon to the center of the sample could be explained as a result of carbon solute segregation during solidification. The lack of appreciable increase in graphitic carbon crystallite size has been attributed to the relatively uniform DC voltage present

throughout the sample and the low current density in the region surrounding the Cu/graphite electrode which is not conducive to self-assembly by a dielectrophoretic assembly process. Subsequently, the electrical conductivity measured in the covetic sample was lower than the baseline, due to the lack of a 3D conductive network of graphitic sheets formed within the sample.

Future work would involve exploring other electrode configurations that could increase the electric field gradient and potentially be more conducive to dielectrophoretic assembly of a conductive carbon network throughout the aluminum matrix. Potentially an AC field could produce better results than the DC field used in this study. Examining the covetics process from a voltage standpoint could lead to a mechanistic understanding of the process compared to the focus on current density used in this work. Additionally, the trends of graphitic carbon crystallite size and electrical conductivity at different points in the cast covetic sample could be more thoroughly evaluated if more samples were fabricated using the same methodology but for different currents and times. Potentially a higher current and/or longer duration of current application could improve the graphitic carbon structure and electrical properties measured in covetic samples.

Chapter 4: Micromechanics of AA-1350 3 wt. % C Covetics

4.1. Motivation and Objectives

The interpretation of mechanical properties in covetics by uniaxial tension testing has been complicated by the complex cause-and-effect of microstructure on macroscale mechanical response. Factors such as differing grain size, different precipitate concentration/size, and pre-existing stress/strain state of metals can all affect overall mechanical properties. Additionally, heat treatments, which affect these microstructural features, can significantly affect the mechanical properties of the final material¹¹⁷. Thus, for covetic materials, it has been difficult to determine whether the enhanced mechanical properties are a result of reinforcement by the graphitic carbon phase, or a result of microstructural factors/variation introduced during processing that are independent of the carbon phase^{31,41,44,118}. Shumeyko et al.⁴³ simulated the theoretical indentation response of an aluminum grain with an embedded epitaxial layer of graphene and found that the hardness would increase by 28% in this system with no change in stiffness; however, it is unclear whether this increase could be observed in practice when considering the additional effects of microstructural features such as voids, and the fact that the graphitic carbon in the covetics samples tested here resemble graphite more than graphene nanoribbons.

The value of using nanoindentation to address this limitation is the ability to locally probe the mechanical properties of areas that showed increased graphitic carbon crystallite size by Raman to determine whether those areas showed an increase in hardness and/or elastic modulus due to the presence of graphitic carbon. Additionally, because nanoindentation probes mechanical properties locally, it is feasible to use additional structural characterization

techniques in that area specifically to interpret the microstructural features that may affect the mechanical response. Prior to performing nanoindentation the ROI identified by Raman as having high carbon with increased crystallite size were analyzed by SEM/EDS and some by TEM in order to identify the grain orientation of the aluminum and presence of secondary phases in these regions. Thus, the goal of this work was to determine whether the graphitic carbon formed by the covetics process effectively acts as a reinforcement phase that improves the overall mechanical properties of covetic samples, and to account for microstructural features present in the sample that would affect the mechanical properties measured by nanoindentation.

4.2. Description of Covetic Samples and Identification of Regions of Interest (ROI)

The samples tested by nanoindentation were AA-1350 3 wt% C covetics. Ge et al.⁴⁴ reported the details of the fabrication process, electrical conductivity, and hardness testing. It was made by the same process described in Section 2.1, using activated carbon as the starting material and the pointed graphite electrode to apply current. The electrical conductivity of the sample that showed the greatest improvement was 61.8 +/- 0.7% IACS (35.8 +/- 0.4 MS/m). The hardness by Vickers hardness test was 0.2199 +/- 0.0068 GPa. Both the electrical conductivity and Vickers hardness were improved compared to the baseline sample, with electrical conductivity of 58.4 +/- 0.7% IACS (33.9 +/- 0.4 MS/m) and Vickers hardness of 0.203 +/- 0.011 GPa. The hardness was found to be inversely correlated to the porosity level in the sample (estimated by density), which motivated the use of nanoindentation to determine whether the improvement was related to the presence of the carbon structure or reduced porosity compared to the baseline. A plot of hardness vs. porosity is plotted in Figure 4.1. Regions of interest (ROI) that showed increased graphitic carbon crystallite size were identified in the covetic sample and the local mechanical properties were tested using nanoindentation.

4.3. SEM/EDS Analysis of the ROIs

Structural characterization was performed to gain microstructural information about the covetic samples that assisted in the interpretation of the nanoindentation results. Because nanoindentation tests a small volume of material (on the order of μm^3), microstructural features local to the indent can strongly affect the measurement¹¹⁹. The goal of this work was to isolate the role of graphitic carbon on the mechanical properties of covetic samples, thus SEM/EDS was used to identify other microstructural features that may have affected the mechanical response.

SEM was performed to collect micrographs from the areas where graphitic carbon ROIs were found by Raman spectroscopy. It was found that many of the areas that showed increased graphitic carbon crystallite size occurred at the edge of large voids ($\sim 100\text{-}500\ \mu\text{m}$), shown in

Figure 4.2. The red circles in the micrographs indicate the areas that showed increased graphitic carbon crystallite size by Raman spectroscopy.

Additionally, some of the carbon ROIs were at the AA-1350 grain boundaries. EDS was performed on these areas to identify intermetallic compounds at the grain boundaries, shown in Figure 4.3. The precipitates mostly consisted of iron with

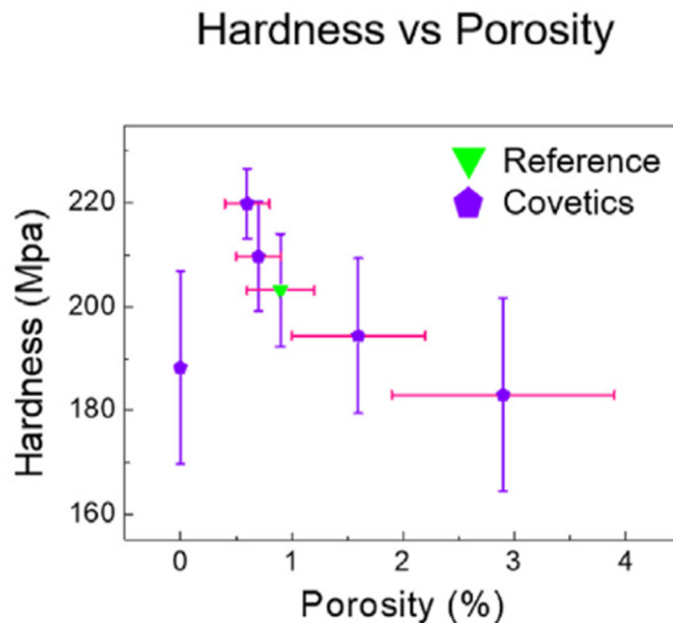


Figure 4.1. Vickers Hardness vs. porosity estimated from density measurements for AA-1350 3 wt% C samples. There is a trend that the hardness increases with decreased porosity in the sample. Reproduced from Ge, X., Klingshirn, C., Morales, M., Wuttig, M., Rabin, O., Zhang, S., & Salamanca-Riba, L. G. (2021). Electrical and structural characterization of nano-carbon–aluminum composites fabricated by electro-charging-assisted process. *Carbon*, 173, 115–125. <https://doi.org/10.1016/j.carbon.2020.10.063>

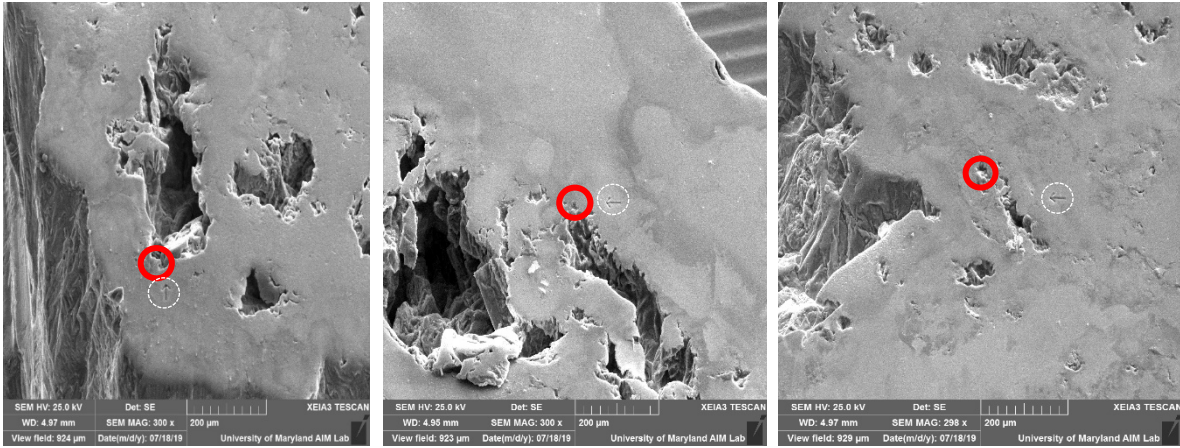


Figure 4.2. Scanning electron micrographs showing the presence of voids near carbon ROIs. The areas circled in red indicate the regions that showed increased graphitic carbon crystallite size by Raman. The small arrows etched into the sample surface, highlighted by the white dashed circles, were milled by FIB for easy identification of the ROIs in the various characterization instruments.

some oxygen. Oxygen was also present throughout the aluminum. Carbon was not detected, though that could be a result of the difficulty in detecting carbon with EDS, due to its low characteristic X-ray energy. This observation is consistent with the expected Al-Fe-Si intermetallic phases that form in AA-1350^{106,117}. It must be considered that hardness and reduced elastic modulus could be affected by proximity to Al-Fe-Si for carbon ROIs that occur near these areas. This is discussed in Section 4.5.3.

4.4. Transmission Electron Microscopy

TEM was used to gain additional structural information about the graphitic carbon ROIs. A lamella for TEM was extracted and thinned using FIB from a carbon ROI that showed increased graphitic carbon crystallite size by Raman spectroscopy. Raman spectroscopy determines structural characteristics indirectly by measuring how the phonon structure of the material scatters optical light. TEM allows for more direct structural information to be obtained by viewing how the atomic structure interacts with the electron beam. Diffraction patterns were

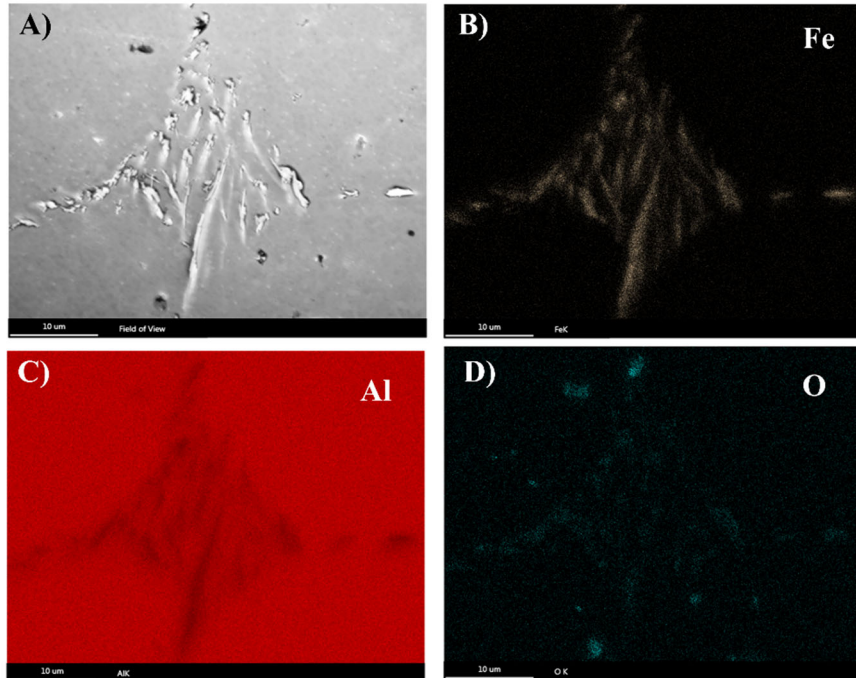


Figure 4.3. A) SEM micrograph of the area analyzed by EDS where precipitates were visible at a grain boundary. B) Fe element map C) Al element map and D) O element map. The precipitates mainly consist of Fe. O was observed in the precipitates and throughout the aluminum in lower concentrations.

collected, which gave additional information about the graphitic carbon crystal structure. High-resolution TEM (HRTEM) was used to image the carbon present in a covetic sample.

A TEM micrograph of a representative ROI showing carbon is presented in Figure 4.4.A. The area that shows increased graphitic carbon crystallite size by Raman was revealed to be a large graphite cluster, several microns in diameter with many graphite layers visible. The strong spots in the diffraction pattern from the carbon area in Figure 4.4.A indicates the c-axis direction of graphite, which means that there are several graphite layers present. The diffraction pattern from the aluminum grain in the bottom left of the figure indicates the FCC (110) crystallographic orientation. There was also an interfacial oxide between the graphite cluster and the Al grain analyzed by EDS, which is expected to degrade the electrical properties of the sample. The HRTEM micrograph shown in Figure 4.4.B shows many layers of graphite in a discrete phase

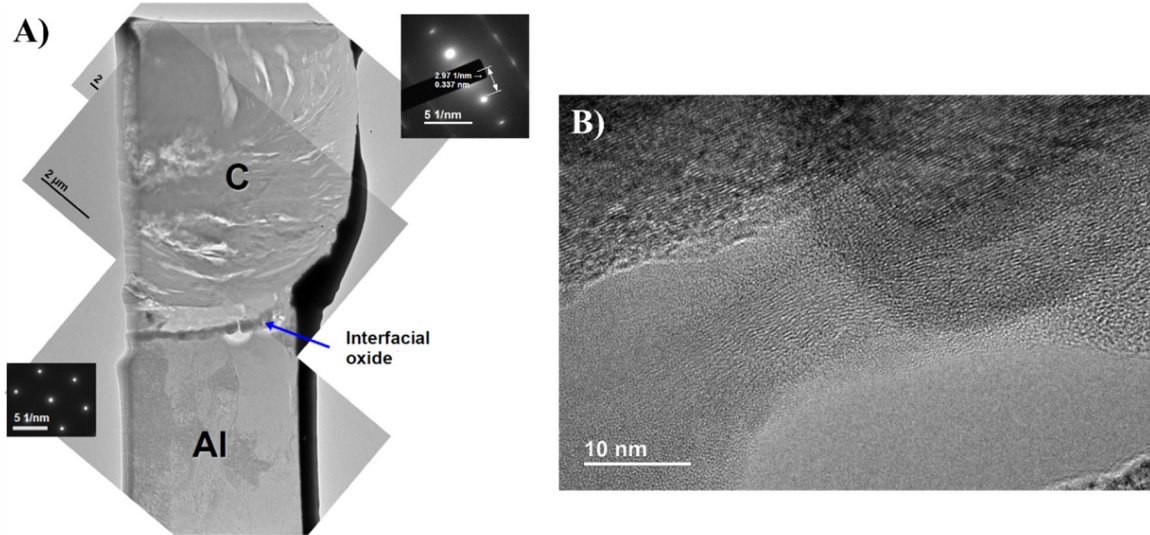


Figure 4.4.A) TEM micrograph showing a large carbon cluster connected to an Al grain with an interfacial oxide layer. The strong spots in the upper right diffraction pattern corresponds to the c-axis of graphite and the lower left diffraction pattern corresponds to the (110) crystallographic orientation of Al. B) HRTEM micrograph showing many graphite layers with some misalignment of layers.

adjacent to the aluminum (darker layers at the top of the micrograph). This indicates that the carbon structure formed during the covetics process in this area more closely resembles a segregated graphite phase rather than a network of graphene nanoribbons extending through the aluminum grains.

4.5. Nanoindentation

Nanoindentation was used to analyze the local mechanical properties of the covetic sample specifically around the ROIs where increased graphitic carbon crystallite size was found by Raman spectroscopy. The ROIs occurred in two microstructural regimes which were probed using the nanoindenter: (1) carbon aggregated into clusters within the aluminum grain and at the edge of voids and (2) carbon segregated to the aluminum grain boundaries. Three different sample stages were used to obtain nanoindentation data: the standard nanoindentation stage, the high-load stage to perform deeper indents, and the nanoECR (electrical contact resistance) stage.

The loading ramp rates were in the quasi-static regime and had a hold sequence for 10 seconds at max load to minimize the influence of creep on the fit of the unloading curve.

The piezo-scanner used on the standard and nanoECR tests allowed for precise positioning of the indents (± 20 nm in x and y) so that the microstructural features of interest could be targeted. Scanning probe microscopy (SPM) was performed by rastering the indenter tip over the sample surface with the piezo-scanner and used to position indents on and around the ROI. The piezo-scanner is capable of performing indents at user-specified coordinates and can be used to place arrays of several indents with user-specified spacing. Both techniques were used to measure the mechanical properties of carbon ROIs in the two microstructural regimes, (1) aggregated carbon clusters within the aluminum grain and near voids and (2) segregated carbon clusters at grain boundaries.

The Oliver-Pharr method was used to calculate the reduced elastic modulus and hardness from the nanoindentation load-displacement data, using the slope of the unloading curve, S , the pressure at max load, P_{\max} , and the contact area at max load, A_c ^{120,121}. In this analysis, S is determined by fitting a linear model to the initial unloading curve in the Hysitron software, where $S=dP/dh$, the rate of change of load as indent depth/displacement, h , is decreased (i.e. as the indenter is removed from the sample). Reduced elastic modulus, E_r , also frequently called the effective elastic modulus, E_{eff} can be calculated using

$$S = \beta \frac{2}{\sqrt{\pi}} E_r \sqrt{A_c} \quad (4.1)$$

where β is a geometric shape factor, 1.05 for a Berkovich tip. The contact surface area at maximum displacement, A_c , is calculated using an experimentally calibrated polynomial area

function that calculates contact surface area as a function of displacement. Hardness is calculated using

$$H = \frac{P_{max}}{A_c} \quad (4. 2)$$

4.5.1. Nanoindentation Near Carbon Aggregates Within Grain/Near Void

The standard stage/transducer was used to indent around carbon ROIs with indentation depths of 100 nm, which resulted in loads of 100-300 μ N. Indents were performed directly on the graphitic carbon areas and also in the AA-1350 matrix near the ROI to determine if the graphitic carbon showed higher hardness than the matrix. Additionally, an array of 3x3 indents with 8 μ m spacing between indents was performed to capture the variation in mechanical properties in the area surrounding the graphitic carbon filler and to assess reinforcement capabilities of the graphitic carbon structure formed by the covetics process.

The carbon ROIs tended to appear as large clusters (\sim 100 μ m). Indents were performed on the carbon inclusions and the nearby matrix to determine whether the graphitic carbon formed by the covetics process acts as a reinforcement phase with increased hardness and/or reduced elastic modulus than the aluminum matrix. Optical micrographs from the areas where indents were performed are shown in Figure 4.5.A for the carbon inclusion and 4.5.B for the aluminum matrix. The blue crosshairs in the micrographs indicate where the indents were performed. The load-displacement curve shown in Figure 4.5.C indicates that the carbon inclusion has decreased hardness and modulus compared to the matrix as it required less force to indent to the same depth of 100 nm in the covetic sample compared to the baseline, 100 μ N and 300 μ N, respectively. Additionally, decreased slope of the unloading curve for the carbon inclusion compared to the matrix indicates that the carbon inclusion is less stiff than the matrix. From

these results it can be determined that the graphitic carbon formed by the covetics process does not act as a reinforcement filler with enhanced mechanical properties. It has both lower hardness and stiffness than the aluminum matrix. This is consistent with the observation from TEM that the carbon phase consists of many graphite layers, as the energy barrier to dislocation glide along the basal plane of graphite is low, which reduces the resistance to plastic deformation¹²².

Further indentation was performed around an ROI that contained clustered graphitic carbon to further confirm that the graphitic carbon clusters do not act to reinforce the aluminum matrix. An optical micrograph with a diagram showing where Raman spectroscopy and nanoindentation were performed is shown in Figure 4.6.A. The distance between the area sampled by Raman spectroscopy and area sampled by nanoindentation ($\sim 40 \mu\text{m}$) was

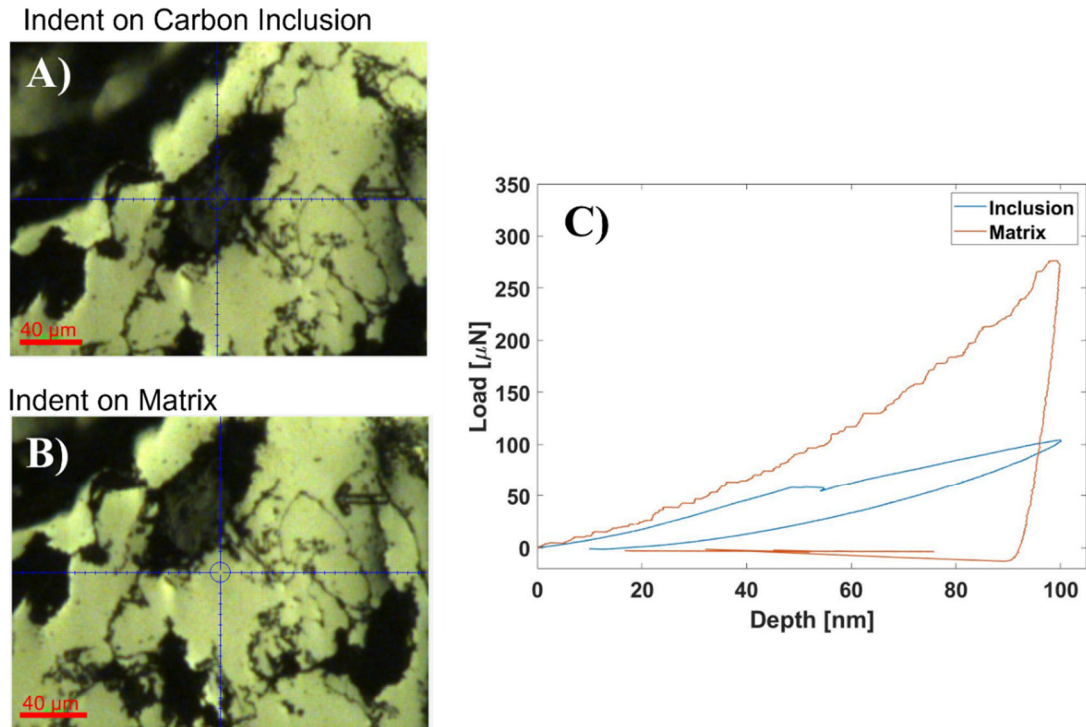


Figure 4.5.A) Optical micrograph from where the indent on the carbon inclusion was collected, shown by the crosshairs at the center of the micrograph. B) Optical micrograph showing where the indent on the matrix was collected. C) Load-displacement curve showing that the carbon inclusion has much lower hardness and reduced elastic modulus than the matrix indent, shown by the lower load needed to indent to the same depth and the decreased slope of the unloading curve

necessitated by the requirement of a flat sample surface for nanoindentation, discussed further in Section 4.7.1. The area sampled by nanoindentation showed dark features in the optical micrograph which likely corresponded to graphitic carbon. The load-displacement curves are shown in Figure 4.6.B and the reduced elastic modulus and hardness calculated from each curve are shown in Figure 4.6.C and 4.6.D, respectively. There was considerable point-to-point variation among each indent in the array, which reflects the microstructural heterogeneity of the sample. Similar arrays of nanoindentation were performed on the baseline sample. The average of several indents on the baseline sample gave an average reduced elastic modulus and hardness of 82.7 +/- 18.0 GPa and 1.10 +/- 0.30 GPa, respectively shown in Figure 4.6.C and 4.6.D. All of the nine indents on the covetic sample showed decreased elastic modulus compared to the average baseline values, while some hardness values in the covetic sample showed similar hardness to the baseline sample further demonstrating that the graphitic carbon clusters formed by the covetics process do not act as an effective reinforcement phase.

4.5.2. Electrical Contact Resistance (ECR)

ECR measurements were obtained around ROIs that showed increased graphitic carbon crystallite size to assess whether those areas also showed higher electrical conductivity. nanoECR was used to qualitatively assess whether the graphitic carbon ROIs showed enhanced electrical properties relative to the surrounding matrix. Using this method, it is possible to qualitatively assess whether the graphitic carbon ROIs are more or less conductive than the areas where graphitic carbon was not detected. A voltage bias is applied between the transducer and the nanoECR sample stage, and the current flow through the conductive boron-doped diamond tip is measured. The relative differences in current flow for indents in different areas of the sample can indicate whether the areas containing graphitic carbon are more or less conductive

than the aluminum matrix. Indents were performed in displacement control to 100 nm, and a 5 V bias was applied for 10 seconds at maximum displacement, while the current flow through the tip

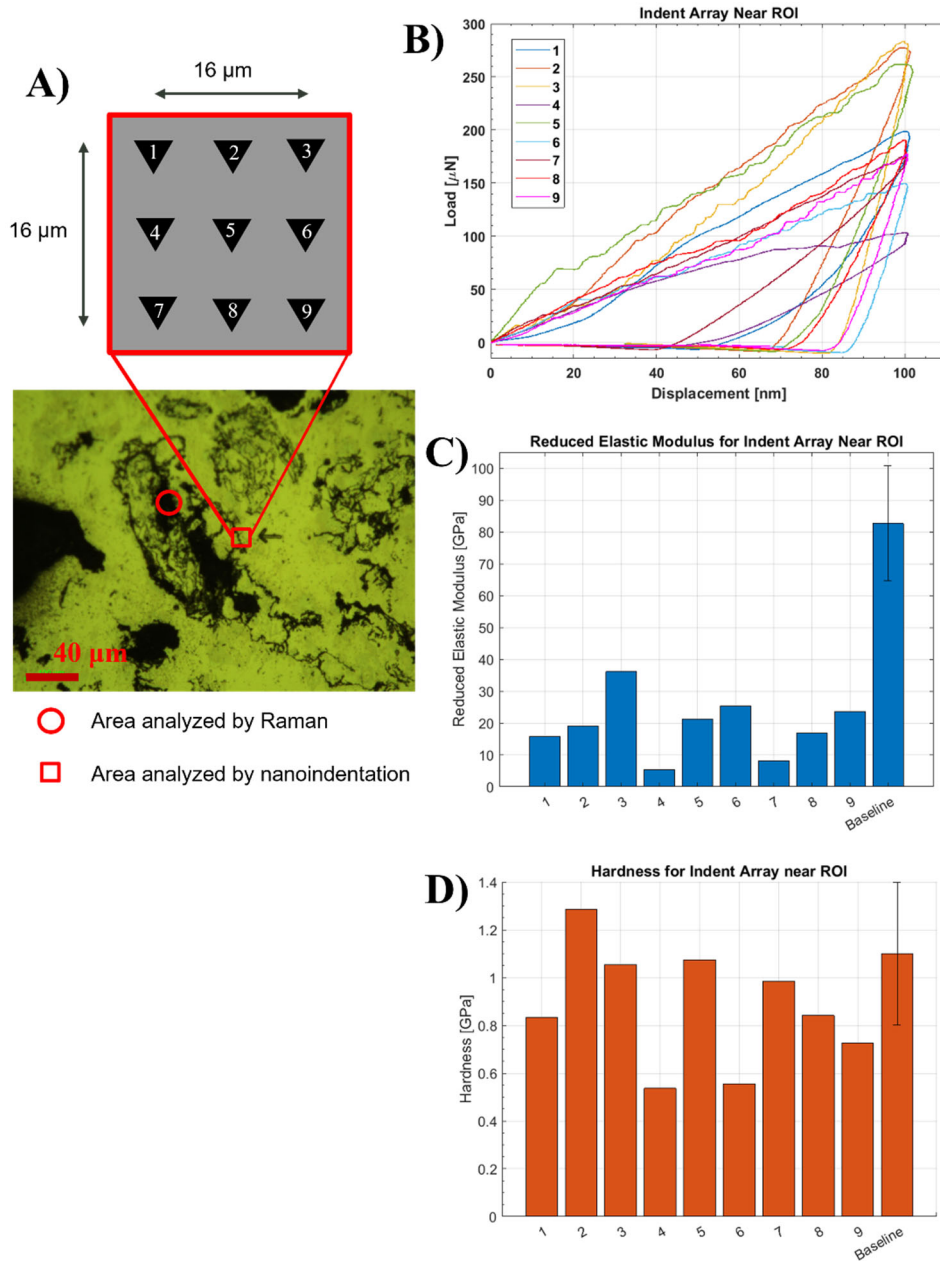


Figure 4.6.A) Optical micrograph with a diagram showing the areas where Raman spectroscopy (red circles) and nanoindentation (red square) were performed. B) Load-displacement curves for the indentation array showing variation in mechanical response. C) Bar chart of reduced elastic modulus and D) hardness showing that there is significant point-to-point variation in properties for the different indents in the array.

was measured. Electrical contact resistance measurements were performed on the carbon inclusion and compared to measurements on the aluminum matrix.

The results of current vs. time were compared for the indents on the carbon inclusion and on the matrix, shown in Figure 4.7. The current flow was greater for the two indents on the matrix, between 90-105 μA , compared to the three indents on the carbon inclusion which ranged from 30-80 μA . Thus, the carbon inclusion is less conductive than the aluminum matrix, and the graphitic carbon formed by the covetics process does not appear to be a highly conductive structure.

4.5.3. Nanoindentation Near Carbon at Grain Boundaries

One of the carbon ROIs that occurred at a grain boundary was tested with nanoindentation; however as mentioned in Section 4.3, Al-Fe-Si intermetallic phases formed at the grain boundary which could affect the interpretation of the indentation response. The Al-Fe-Si intermetallic phases strengthen the material by precipitation hardening, where the precipitates increase the hardness/yield

strength by blocking

dislocation motion.

Additionally, the defect

density at the grain

boundary can inhibit

dislocation motion and give

rise to hardening effects by

the Hall-Petch effect, where

a reduction in grain size

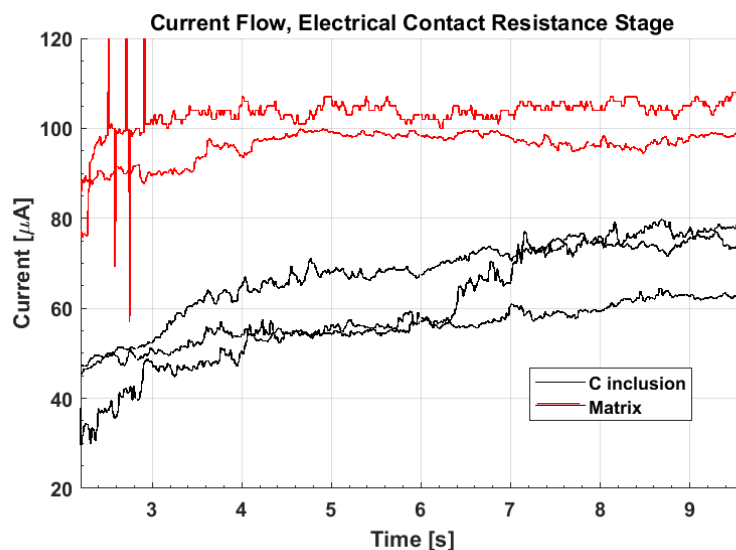


Figure 4.7. nanoECR measurements with a 5 V bias comparing current flow through the indenter tip when on the carbon inclusion and the aluminum matrix.

results in an increase in hardness/yield strength. As a result, these two strengthening phenomena must be considered when interpreting the nanoindentation results from this area.

Two distinct grains were observed with EBSD, shown in Figure 4.8, from an area where Raman spectra indicated increased graphitic carbon crystallite size, shown in Figure 4.9. An indentation array, shown in Figure 4.10, was placed around the ROI to determine

if there was a reinforcement effect from the graphitic carbon. Because the intermetallic phases and proximity to grain boundary are known to strengthen materials independent from the effects of the carbon phase, an indentation array was performed on the baseline sample with no carbon added in a region with similar microstructural features, shown in Figure 4.11, to assess the strengthening effects of these features in the absence of carbon. A comparison of reduced elastic modulus and hardness near the covetic and baseline grain boundaries are shown in Figure 4.12. It can be seen that there was no significant improvement in the reinforcement capability of the covetic sample that contained graphitic carbon compared to the baseline sample that showed similar microstructural features. This indicates that graphitic carbon formed near the grain

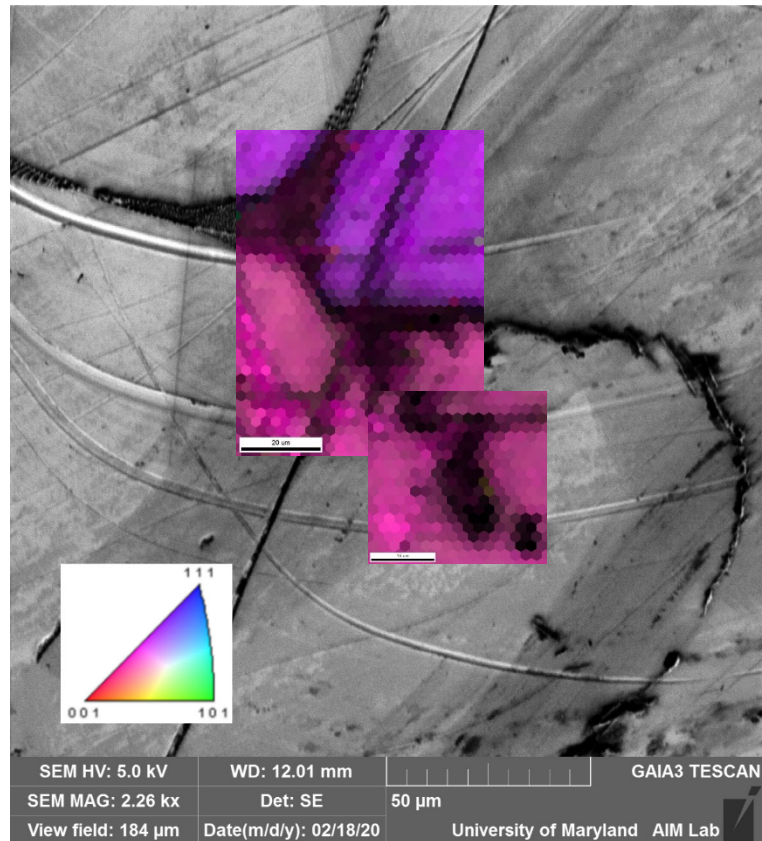


Figure 4.8. EBSD maps showing that the graphitic carbon ROI in Figure 4.9, occurs at the boundary between two grains with different orientations.

boundaries does not provide an appreciable increase in strength outside of known microstructural strengthening mechanisms that are observed in the baseline sample.

4.5.4. High-Load Transducer/Stage Around ROIs

The high-load stage was used to perform deeper indents that sampled a larger volume of material which minimizes the influence of point-to-point microstructural variation in the area around the indenter compared to the standard stage indents that were only 100 nm deep. Rather than testing specific microstructural features, the objective was to assess if the average hardness and/or modulus increased in the areas surrounding the carbon ROIs. The indents were performed in load-control mode with $P_{\max}=60$ mN, which resulted in typical indent depths of 1-6 μm . To determine if there was an average increase in mechanical properties around the carbon ROIs, the averages of hardness and reduced elastic modulus were compared for three carbon ROIs on the

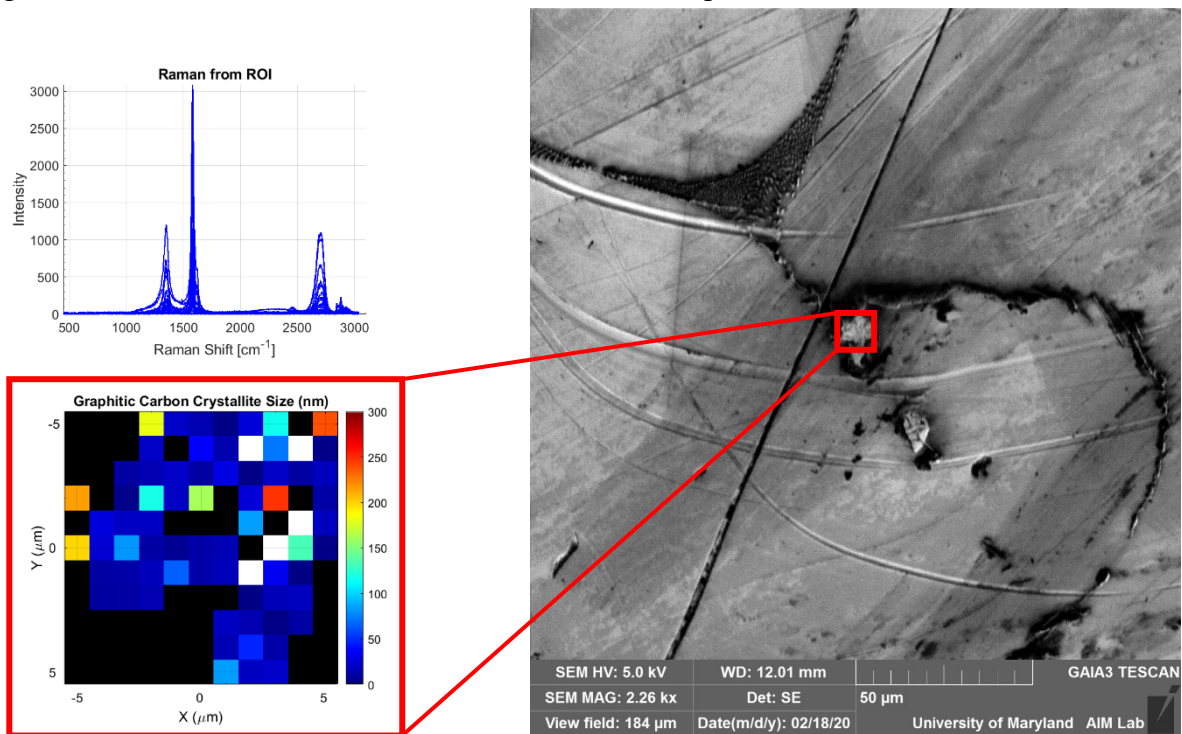


Figure 4.9. Left: Raman spectra and map of graphitic carbon crystallite size for the carbon ROI that occurs at a grain boundary in the SEM image at right.

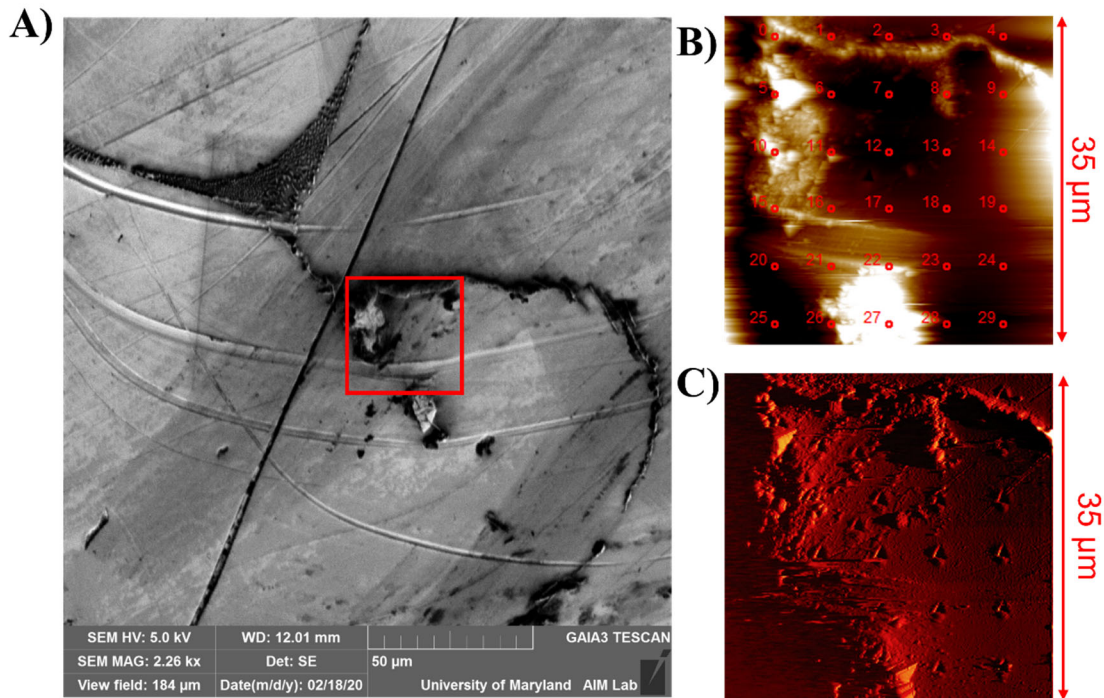


Figure 4.10. A) SEM micrograph showing the area of the covetic sample where the nanoindentation array was placed. B) Topography SPM micrograph prior to indenting showing the placement of the array and C) Gradient SPM micrograph after indentation showing the placement of indents.

covetic, a randomly selected area of the covetic, and the baseline sample. At each location, four 3x3 indent arrays with an indent spacing of 65 μm were performed and average hardness and reduced elastic modulus were calculated from the group of 36 indents in each area. Three covetic ROIs, a random area of the covetic sample, and an area of the baseline sample were compared to determine if (1) the covetic sample showed an increased reduced elastic modulus and/or hardness compared to the baseline and (2) if the covetic ROIs that contained graphitic carbon had higher mechanical properties than a randomly selected area of the covetic that had not previously been identified as an ROI with increased graphitic carbon crystallite size.

Optical micrographs from representative areas of the baseline and covetic samples showing the general microstructure in the areas where indents were performed are given in Figure 4.13.A and 4.13.C, respectively. It can be seen that there is greater microstructural

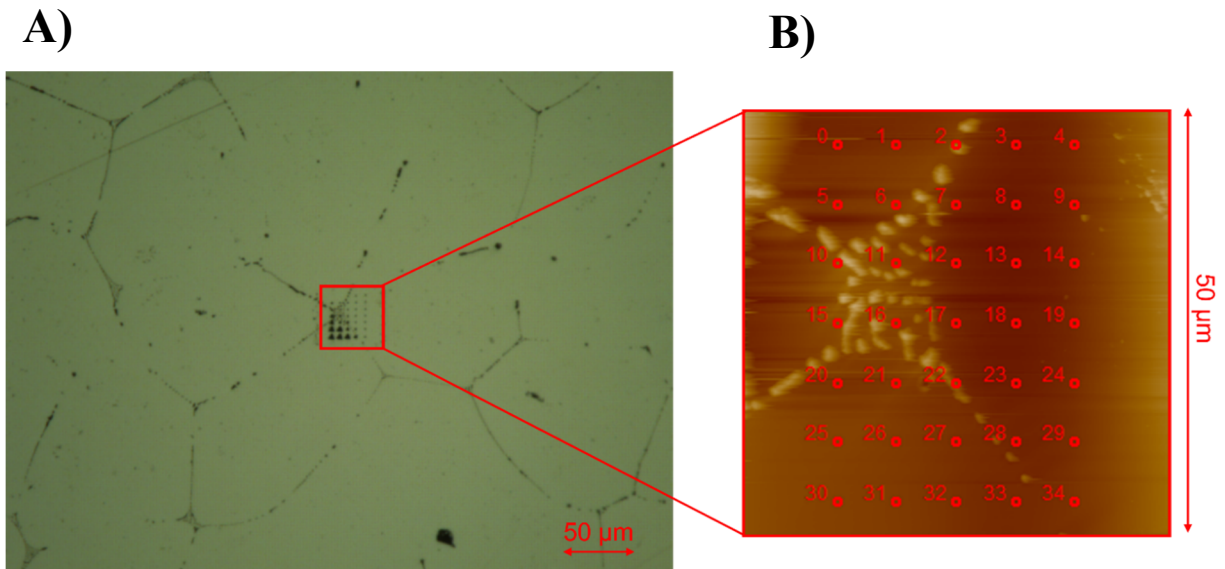


Figure 4.11. A) Optical micrograph showing the location of the indentation array on a grain boundary of the baseline sample. B) SPM topography micrograph showing the position of the indentation array relative to the precipitates visible at the grain boundary. The indents were performed in load control mode

heterogeneity in the covetic sample than the baseline, with many dark features on the covetic sample indicating either graphite aggregates or voids. The mechanical effects of these

microstructural features are reflected in the nanoindentation load-displacement curves, shown in Figure 4.13.B and 4.13.D. There was less variation in the indentation response on the baseline than the covetic sample, with some areas of the covetic sample showing much greater displacements

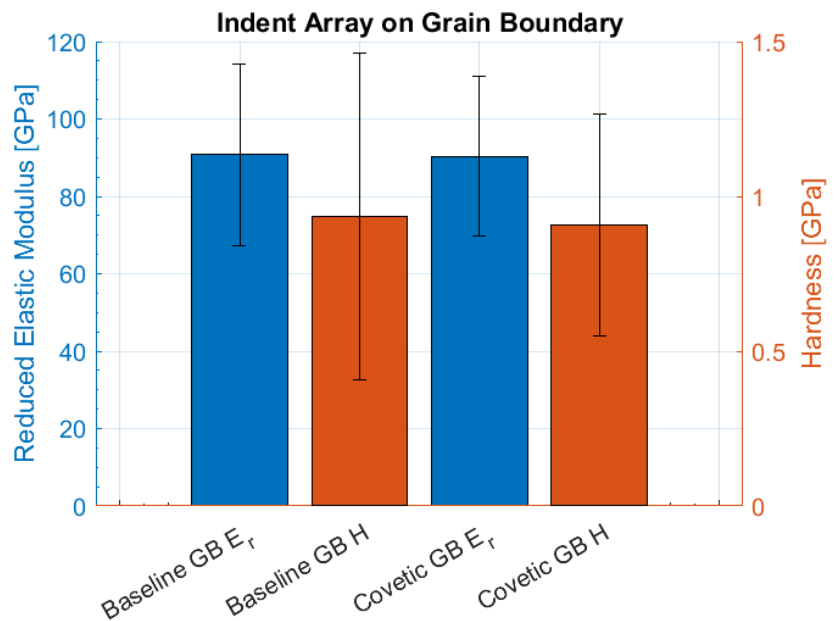


Figure 4.12. Summary of reduced elastic modulus and hardness calculated from the nanoindentation arrays performed on/around the grain boundaries in the baseline and covetic samples. The covetic showed no difference in reduced elastic modulus and hardness at the grain boundary from the baseline sample.

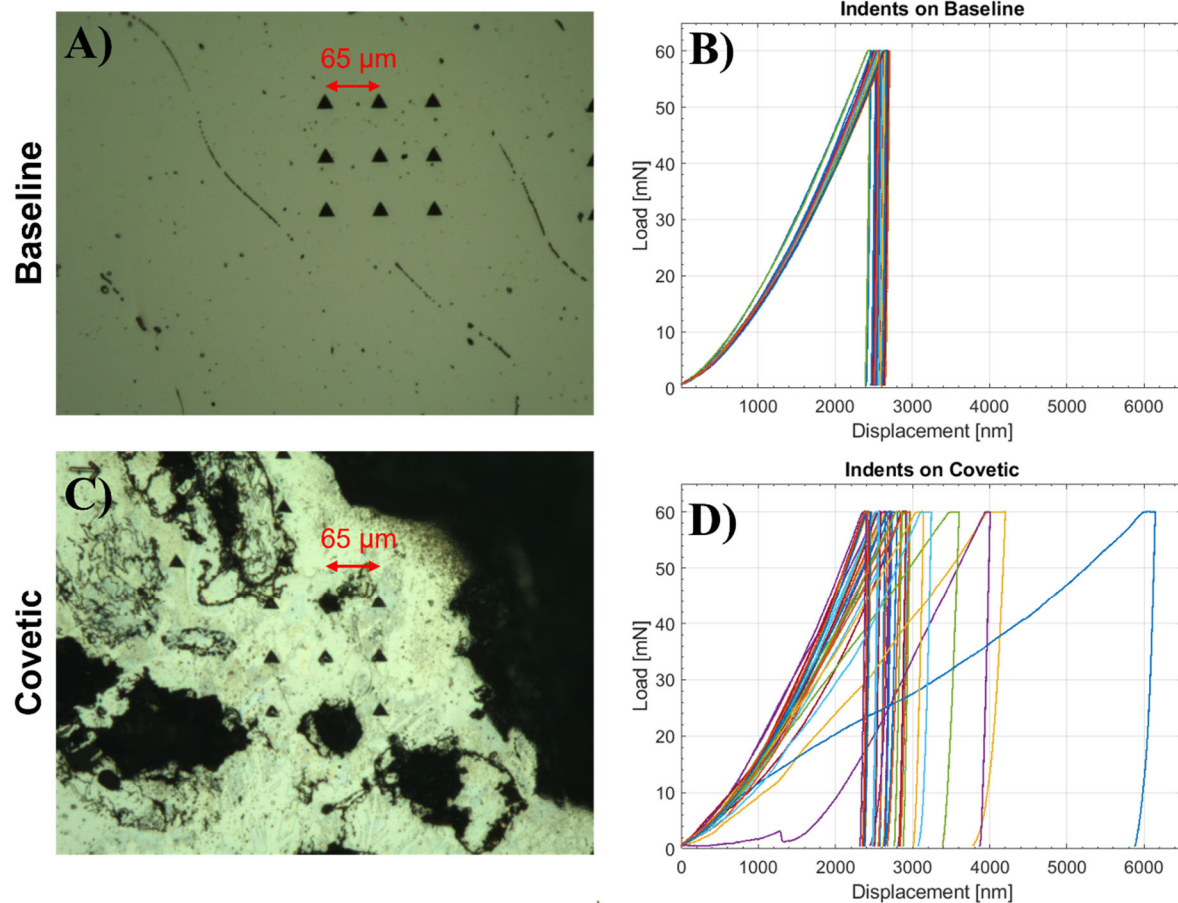


Figure 4.13. A) Optical micrograph showing a representative area of the baseline sample where an indentation array was placed. B) Load-displacement curves for all indents into the baseline sample, showing minimal variation. C) Optical micrograph showing a representative area of the covetic sample where indentation arrays were placed. There is considerably more microstructural heterogeneity than the baseline sample. D) Load-displacement curves for indents on the covetic sample. Consistent with the microstructural heterogeneity, there is more heterogeneity in the mechanical response than for the baseline.

for the same load, indicating a softer material. A statistical summary of the nanoindentation data for the three covetic ROIs, random covetic area, and baseline sample are shown in Figure 4.14. The reduced elastic modulus decreased for all areas on the covetic sample, which could be attributed to the increased compliance of the sample caused by voids and aggregated carbon. The hardness showed neither an increase nor decrease, but the variance of hardness increased for the covetic samples compared to the baseline. The increased variance in hardness could be a result of the increased microstructural heterogeneity in the covetic sample. The lack of an increase in

hardness is consistent with the previous observations that the graphitic carbon clusters formed by the covetics process do not demonstrate enhanced mechanical properties.

To remove points that occurred on or near voids from the statistical

analysis, *k*-means clustering was performed in MATLAB on the high-load transducer data to separate the indent data plotted as hardness vs. reduced elastic modulus into clusters and subtract out the two clusters that showed both the lowest hardness and reduced elastic modulus, which most likely occurred on or near voids. MATLAB uses the *k*-means++ algorithm and the squared Euclidian distance metric for cluster center initialization. The optimum number of clusters was determined by the elbow method. The two clusters with excessively low reduced elastic modulus were removed from the dataset and the statistics were re-calculated to determine if there was an improvement in mechanical properties in the areas that were not influenced by voids.

A plot of hardness vs. reduced elastic modulus is given in Figure 4.15 using the data shown in Figure 4.14. It can be seen that the reduced elastic modulus decreased for all indents on the covetic sample. Some indents showed a slight increase in hardness, but a majority of the points showed a decrease in hardness as the reduced elastic modulus decreased. The *k*-means clustering method was used to separate the data into distinct clusters so that the lower modulus

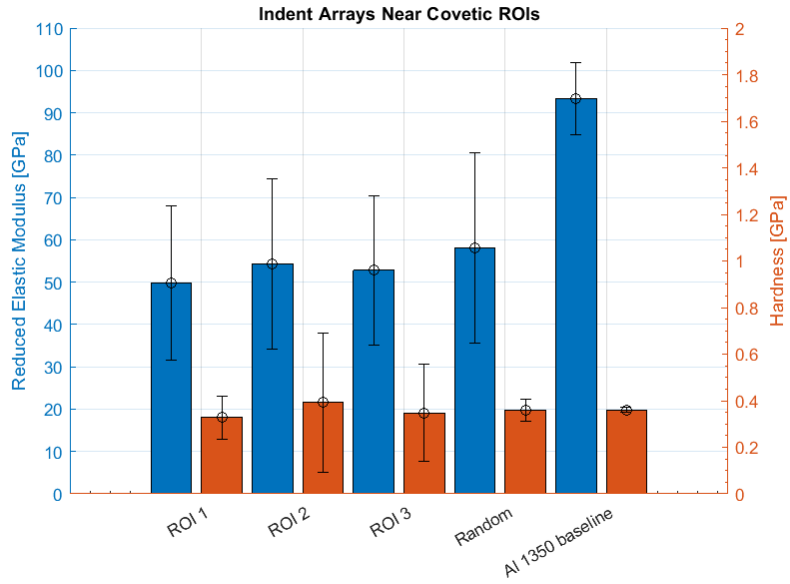


Figure 4.14. Summary of reduced elastic modulus and hardness measured from the indentation arrays placed near the three covetic ROIs, a random area of the covetic sample, and the baseline sample.

and hardness values that most likely corresponded to voids could be removed from the data set. The optimum number of clusters was selected using the elbow method where the total Euclidian distance from each data point to its centroid is plotted vs. the number of clusters used and the optimum number of clusters is chosen as

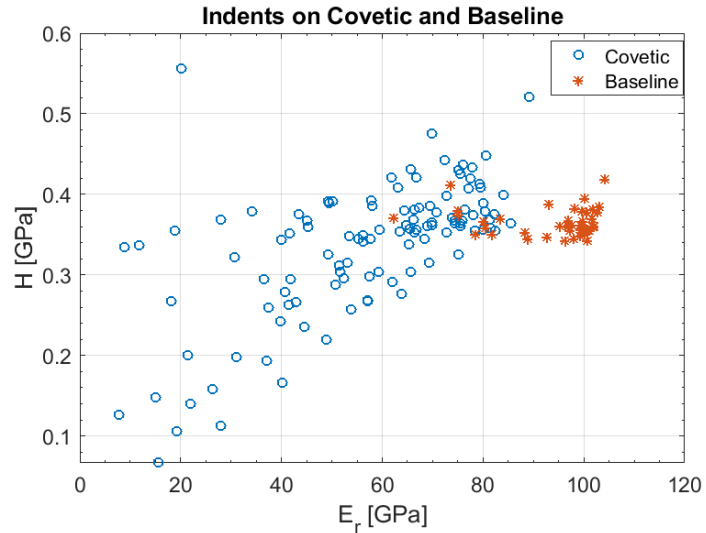


Figure 4.15. Hardness plotted vs. reduced elastic modulus showing that the modulus was reduced in all covetic sample compared to the baseline. The covetic sample also showed more variation in hardness than the baseline sample.

the point where the decrease in distance for each additional cluster becomes linear^{123,124}. The plot of total Euclidian distance vs. number of clusters is shown in Figure 4.16 where the optimum

number of clusters is 5. Figure 4.17.A shows the clustered data with $k=5$ chosen as the optimum number of clusters from the elbow method. The two clusters that showed the lowest hardness and reduced elastic modulus were removed from the statistical analysis, k_3 and k_5 , as it was assumed that they most likely

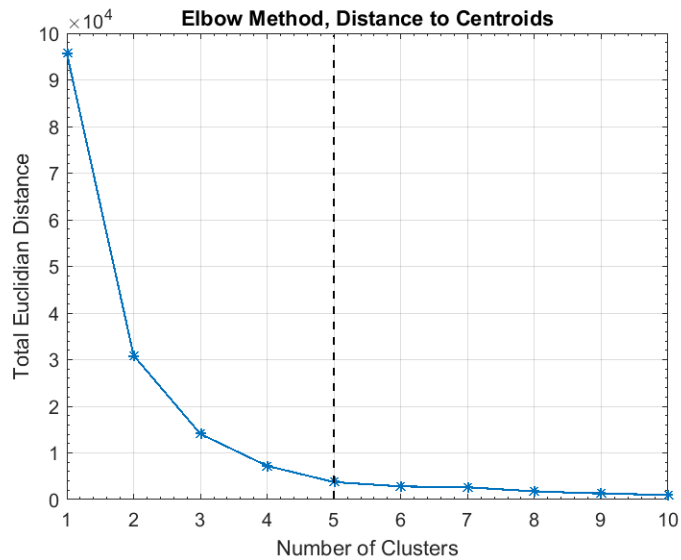


Figure 4.16. Total Euclidian distance vs. number of clusters used to evaluate the optimum number of clusters by the elbow method. The optimum number of clusters is chosen as the point where the decrease in distance for each additional becomes linear, which for this dataset is $k=5$.

corresponded to indents influenced by voids.

The average reduced elastic modulus and hardness of the covetic sample with k3 and k5 removed was compared to the baseline values, shown in Figure 4.17.B. Even when removing k3 and k5 from the analysis, the covetic sample still showed lower reduced elastic modulus compared to the baseline, although the variance decreased. Similarly, the average hardness of the covetic sample after removing k3 and k5 was only slightly improved (from 0.325 to 0.368 GPa), but the variance was reduced. This analysis indicates that even after excluding the points that most likely corresponded to voids and showed the lowest mechanical properties, the reduced elastic modulus and hardness of the covetic sample were lower than the baseline indicating no reinforcement by the graphitic carbon phase. Thus, the graphitic carbon clusters formed by the covetics process are not an effective reinforcement phase.

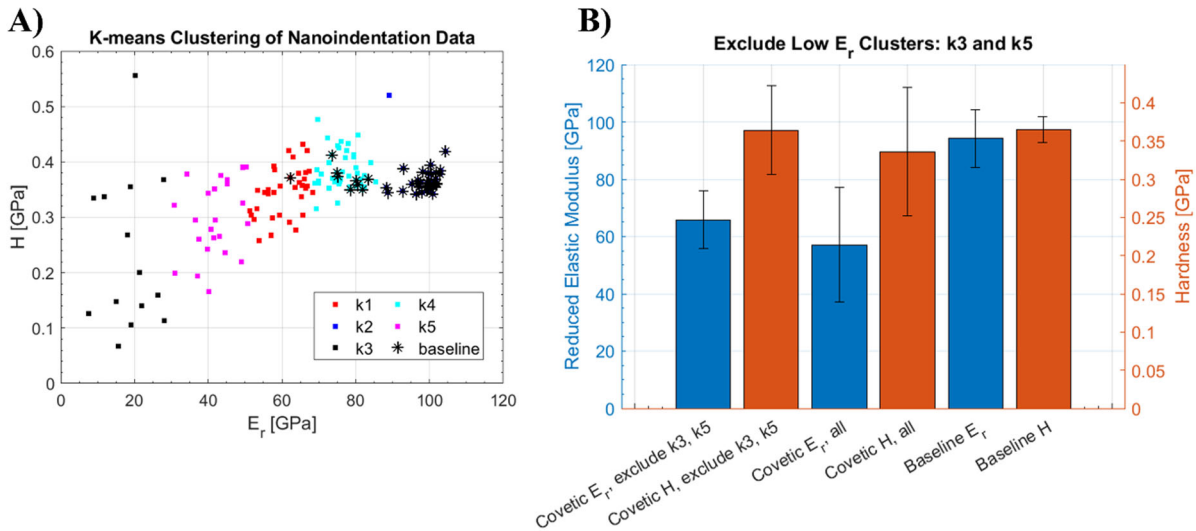


Figure 4.17.A) H vs. E_r data grouped into five clusters using the k -means clustering method. The two clusters with the lowest modulus, k3 and k5, were assumed to be influenced by voids in the covetic sample and were excluded from B) the statistical summary.

4.6. Discussion

4.6.1. Contact Area Function: Pile-up and Sink-in Behavior

There are a number of assumptions made in the analysis of nanoindentation data which contributed to the challenge in measuring the mechanical properties of covetics using this technique. Most relate to the calculation of the contact area from the contact area function. The main difference between nanoindentation and other indentation testing methods (Rockwell, Brinell, Vickers, Knoop) is that the contact area used in hardness calculations must be estimated using a contact area function that is empirically calibrated for the specific tip to give tip-sample contact area as a function of indent depth, which accounts for imperfections in the tip geometry introduced during machining and wear over time. The calibration is performed on a single crystal fused quartz sample, and the result is extrapolated to material systems that may have slightly different properties/behavior. The following assumptions are made in the formulation of the contact area function and subsequent calculation of reduced elastic modulus and hardness: (1) the material is homogeneous and isotropic, (2) the sample surface is perfectly flat, and (3) the material is elastic-perfectly plastic, i.e. the material is linear elastic up until the yield point where plastic deformation occurs without work hardening. When these assumptions do not explicitly apply to the material being tested, nanoindentation can still be a useful technique, but the interpretation of the results must be carefully considered.

The prevalence of porosity and voids in the covetic sample formed during processing seemed to dominate the elastic properties of the covetic samples. In this instance, the assumption that the material is homogenous no longer applies. The elastic response of the heterogeneous material can be considered like a series of springs connected in series or parallel. The presence of voids in the volume of material deformed by the indenter tip adds a compliance to the system,

which is reflected in the reduced elastic modulus. On the covetic samples, the reduction in reduced elastic modulus most likely primarily reflects the compliance effect of voids present in the sample rather than any changes in elastic properties of the solid material as a result of interaction between the graphitic carbon and aluminum matrix.

Another notable source of error in the area function for this material system is “pile-up” or “sink in” of the material around the indenter tip which leads to an underestimation of contact area for pile-up (and subsequent over-estimation of reduced elastic modulus and hardness) and overestimation of contact area for sink-in behavior (underestimation of reduced elastic modulus and hardness). Aluminum, which has a low yield stress, tends to exhibit “pile-up” behavior where plastically deformed metal flows up from the sample surface around the indenter tip, which is not adequately accounted for in the area function calculation that assumes the material deformation is elastic-perfectly plastic. Additionally, work-hardening can affect the pile-up/sink-in behavior of the material which is not easily quantified and accounted for, as residual stress in the material can affect the work-hardening behavior¹¹⁹. While this effect likely contributed to some overestimation of the reduced elastic modulus and hardness of aluminum, the indents directly on the carbon inclusion show such a drastic reduction in mechanical properties that it is clear that the graphitic carbon formed as a result of the covetics process was not an effective reinforcement phase.

4.6.2. Microstructural Strengthening Mechanisms

When interpreting nanoindentation of a heterogeneous alloy microstructure, it is important to consider the microstructural strengthening mechanisms in metals, aside from the effect of the graphitic carbon, that can introduce point-to-point variation in reduced elastic modulus and hardness that are unrelated to graphitic carbon reinforcement. These effects are

likely what caused some of the variation in the indentation response, which necessitated the collection of many (>100 indents) on the covetic sample with the high load transducer so that statistical analysis could be used to interpret the results.

The main microstructural features that affected the indentation response in this work were proximity to grain boundaries, precipitate strengthening by the Al-Fe-Si intermetallic phases at grain boundaries, voids, and potentially work hardening/pre-existing strain in the aluminum matrix during sample solidification and/or machining/polishing. For the scope of this work, it was not necessary to meticulously account for the effect of each of these phenomena, but reasonable attempts were made to be aware of the source of variation, such as by performing EDS/EBSD and indenting on a grain boundary of the baseline sample. Despite the variation in local mechanical response caused by these effects, it was still possible to make two important observations pertinent to the understanding of the mechanical properties of covetics: (1) there is no clearly demonstrated improvement in mechanical properties as a result of the graphitic carbon clusters introduced into AA-1350 during covetics processing, and (2) the significant void content in covetic samples introduced during processing results in a significant decrease in reduced elastic modulus and hardness of covetic samples compared to the baseline.

4.7. Conclusions and Future Work

The nanoindentation performed in this work demonstrated that there is no evidence that the graphitic carbon clusters produced by the covetics processing method act as an effective reinforcement phase that enhances the mechanical properties of the final composite material. Structural characterization by SEM and TEM indicated that graphitic carbon is present in covetics in the form of large clusters and that there is significant porosity. These two factors result in a significant decrease in reduced elastic modulus and, to a lesser extent, the hardness.

Statistical analysis performed on a population of >100 indents indicates that there is no improvement in mechanical properties, even after removing indents that most likely occurred on voids. Future work to improve the mechanical properties of covetics should focus on the processing technique to improve spatial homogeneity of carbon by formation of graphene nanoribbons throughout the aluminum matrix and the prevention of carbon clustering and void formation.

Chapter 5: Updates to the Covetics Processing System

5.1. Motivation and Objective

The results discussed in Chapters 3 and 4 indicated that the electrical and mechanical properties of covetic samples were degraded by aggregated carbon clusters, oxidation at the carbon-aluminum interface, and voids in the final cast. Increased graphitic carbon crystallite size was measured in some areas of some samples, but the presence of the defects mentioned resulted in a net degradation of electrical and mechanical properties. Additionally, only some areas showed increased graphitic carbon crystallite size, while many areas showed the same graphitic carbon crystallite size as the activated carbon starting material, indicating that potentially insufficient mixing of the aluminum-carbon mixture prevented all of the carbon from entering the high current density region around the electrode during processing. To address these issues a series of updates were made to the covetics processing system to attempt to improve sample quality and observe an increase in electrical conductivity. The main goal was to improve homogeneity of carbon in the covetic sample while limiting oxidation and porosity, which should help improve the electrical conductivity.

5.2. Updates to the Covetics Processing System and Procedure

5.2.1. Dehydrate Activated Carbon Starting Material

In the covetics process, activated carbon with 100 nm particle size is used as the carbon starting material. Activated carbon has high surface area and reactivity; however, this also leads to a high adsorption capacity which could introduce contamination into the covetics sample¹²⁵. The high surface area and reactivity of activated carbon is believed to help facilitate the re-crystallization process when current is applied; however, contamination from adsorbed vapor

species could potentially lower electrical conductivity of the covetic sample. The adsorbing capacity of activated carbon is so high that it is frequently used as a filter material. It has been shown by TEM in Chapter 4 that the carbon present in the covetic sample is surrounded by an oxide layer at the carbon-aluminum interface despite processing in an argon-rich atmosphere. This may have been a result of adsorbed oxygen and water vapor species in the activated carbon

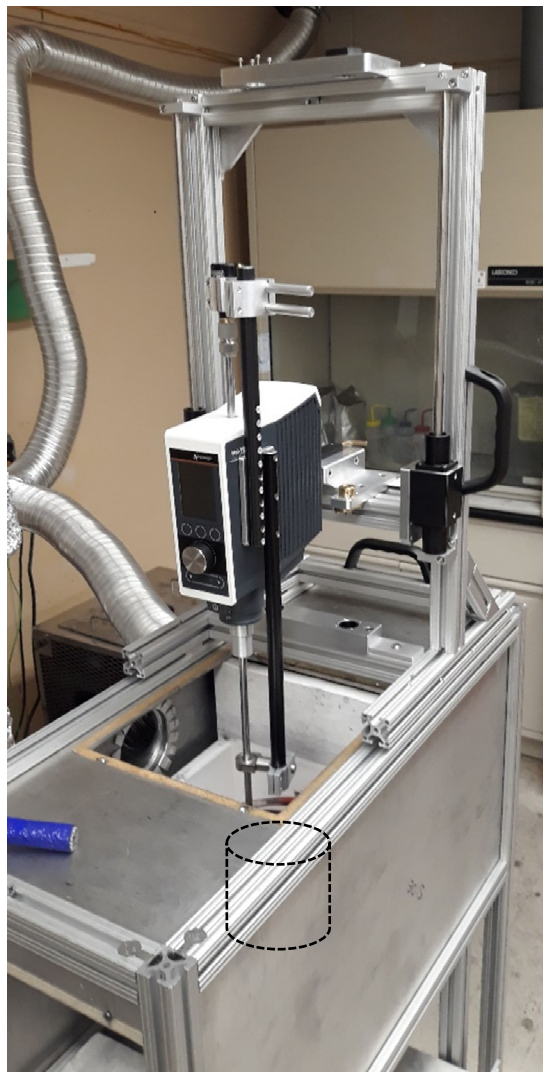


Figure 5.1. The stirrer mounted on an aluminum frame above the aluminum enclosure that contains the induction furnace. The black cylinder indicates the position of the crucible in the enclosure box.

starting material that are then incorporated into the covetic sample.

To mitigate the detrimental effects of adsorbed oxygen and water vapor, the activated carbon starting material was de-gassed in a vacuum furnace at 160° C and 30 mTorr for 24 hours prior to the start of covetics processing. The relatively low temperature was chosen to allow de-gassing of vapor species from the activated carbon surface while preventing reaction of the carbon with oxygen, which begins to occur at 400°C¹²⁵. After de-gassing, the activated carbon was transferred into the crucible and inserted into the covetics processing system that had been purged with argon gas.

5.2.2. Updated Stirring System with Argon Flow

Previously, stirring was performed by an electric drill attached to a variable resistor to adjust mixing speed. In the updated system, this component was

replaced by a Heidolph overhead stirrer capable of achieving 2000 rpm, which allowed for more precise control during processing and evaluation of mixing speed as a process parameter. A photograph of the covetics processing system with the new stirrer mounted on an aluminum frame is shown in Figure 5.1. The aluminum frame was used to move the stirrer up and down from the processing enclosure, the aluminum box in Figure 5.1 that contains the crucible.

Additionally, the shaft and impeller of the stirrer were modified to allow argon flow through the shaft and into the molten Al+C mixture during processing. De-gassing of aluminum castings with pressurized argon is commonly done to remove gas bubbles that cause porosity in the final product¹²⁶. As argon flows through the molten metal, gaseous impurities diffuse into the argon bubbles that then flow out to the surface, resulting in a denser final product. In particular, atomic hydrogen, which is soluble in liquid aluminum, is known to cause porosity in aluminum castings¹²⁶. Additionally, the argon flow could help remove any remaining oxygen impurities that may have been incorporated into the covetic sample by adsorption to the activated carbon.

To employ this technique in covetics processing, a hollow stainless steel rod was used as the shaft of the stirrer and connected to a 99% purity argon tank by vinyl tubing. The impeller tip on the end of the shaft was machined from graphite with outlet holes to allow argon flow out of the shaft and through the molten Al+C, shown in Figure 5.2. As the impeller mixed the Al+C mixture during covetics processing, argon flowed through the shaft and impeller and into the molten material. The goal of this procedure was to remove hydrogen that can cause porosity and remove oxygen, both of which would degrade the electrical conductivity of the covetic sample while at the same time getting better mixing of the carbon in the liquid metal.

5.3. Experimental Methods

5.3.1. Sample Processing Conditions and Sectioning for Characterization

Three covetic samples were made with the updated covetics processing system following the procedure described in Section 2.1 to determine whether the modifications produced samples with increased graphitic carbon crystallite size and electrical conductivity. All three samples were 3 wt% C AA-1350 covetics with current application for 1000s (16.67 minutes) with the pointed graphite electrode. The cylindrical samples were 10 cm in diameter and 2 cm tall. The

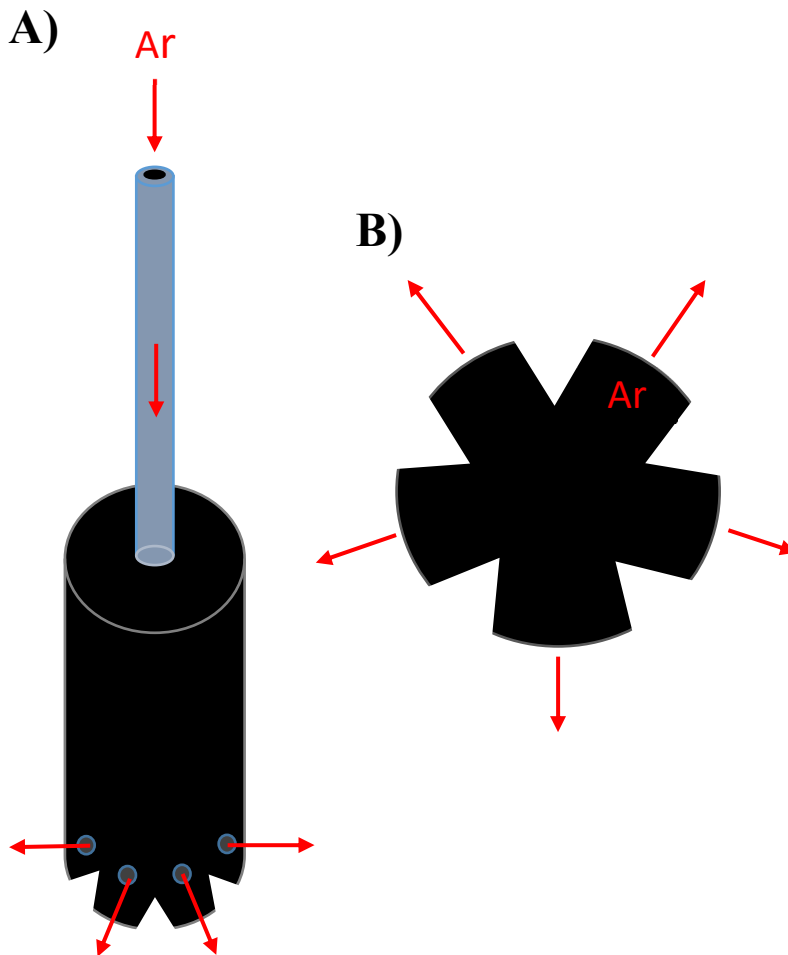


Figure 5.2. Diagram of the stirrer that consists of a graphite impeller attached to a hollow stainless-steel shaft shown from the A) side view and B) bottom view. The red arrows indicate the direction of argon flow through the shaft and out into the melt through holes in the graphite impeller

applied current, stirring speed, and time of argon flow through the stirrer was varied in each sample. Sample A had 100 A applied current, stirring speed of 700 rpm and argon flow through the stirrer during application of current. Sample B had 200 A applied current, stirring speed of 800 rpm, and argon flow through the stirrer during the application of current. Sample C had 200 A applied current, stirring

Table 5.1. Processing conditions for the three covetic samples made with the redesigned impeller

Sample	Current	Stirring Speed	Ar Flow Description
A	100 A	700 rpm	During current application (1000s/16.67 minutes)
B	200 A	800 rpm	During current application (1000s/16.67 minutes)
C	200 A	800 rpm	For 5 minutes after current application is complete

speed of 800 rpm, and argon flow through the stirrer for five minutes after the application of current. A summary of processing conditions for each sample is given in Table 5.1. The samples for Raman spectroscopy and electrical conductivity were sectioned and prepared following the procedure described in Section 2.1.

5.3.2. Raman Spectroscopy, Graphitic Carbon Crystallite Size

The samples for Raman spectroscopy were taken from the center of the cast covetic samples. Graphitic carbon crystallite size was calculated from the Raman data by using the integrated intensity ratio of the D peak at $\sim 1350\text{ cm}^{-1}$ to the G peak at $\sim 1600\text{ cm}^{-1}$ following the method described in Section 3.2.2. Ten $10\text{ }\mu\text{m} \times 10\text{ }\mu\text{m}$ maps were collected for each covetic sample and a histogram of crystallite size from the spectra in all ten maps was generated to determine whether there was an increase from the 7-10 nm crystallite size of the activated carbon starting material as a result of the application of current.

5.3.3. Four Point Probe Electrical Conductivity Measurement

Electrical conductivity was measured by the four point probe method following the procedure outlined in Section 2.4. The samples for electrical conductivity were $\sim 10\text{ cm}$ long cut from the center of the covetic sample along the diameter to determine whether the electrical conductivity of the covetic sample increased compared to the baseline sample. The baseline sample was melted and re-solidified in the covetics processing system and stirred with argon flow through the stirrer for 1000 seconds, but carbon was not added, and current was not applied

during the process. Two samples for electrical conductivity were taken from different places within the baseline sample to assess the spatial variation of electrical conductivity in the cast sample.

5.4. Results and Discussion

5.4.1. Raman Spectroscopy

The histograms of graphitic carbon crystallite size calculated from the Raman spectra are given in Figure 5.3. The results indicated that most carbon present in the covetic samples had the same crystallite size as the activated carbon starting material. 1,210 Raman spectra were collected per sample, but the number of spectra showing crystallite size greater than 20 nm was only 11 for Sample A, 20 for Sample B, and 18 for Sample C. Thus, neither the 100 A or 200 A applied current used for these samples was sufficient to induce rearrangement and crystallization of the activated carbon into graphitic sheets with increased crystallite size.

5.4.2. Electrical Conductivity

The electrical conductivity of each sample measured by the four-point probe method is given in Figure 5.4. Sample A had a conductivity of 55.4 +/- 0.2% IACS (32.1 +/- 0.1 MS/m) and Sample B had a conductivity of 56.9 +/- 0.5% IACS (33.0 +/- 0.3 MS/m). Neither Sample A nor B showed an improvement compared to the baseline samples with 55.6 +/- 1.6% IACS (32.2 +/- 0.9 MS/m) and 47.6 +/- 0.9% IACS (27.6 +/- 0.5 MS/m). Sample C performed significantly worse than all other samples with an electrical conductivity of 35.7 +/- 0.9% IACS (20.7 +/- 0.5 MS/m). Thus, the electrical conductivity was not improved by the addition of activated carbon and application of current by the covetics process. This is consistent with the Raman results that did not show a significant increase in graphitic carbon crystallite size in any of the three covetic samples.

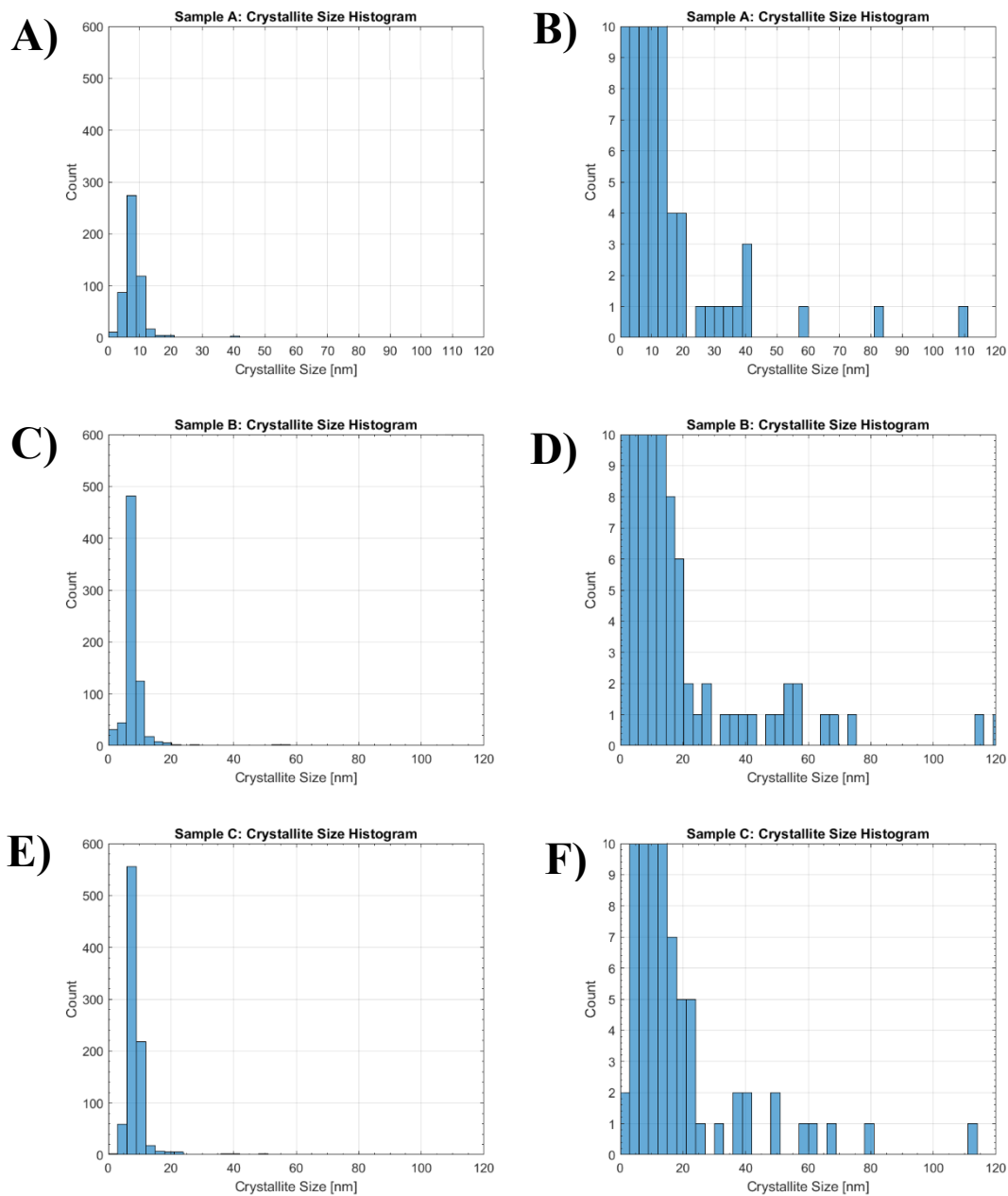


Figure 5.3. Histograms showing the crystallite size for each sample calculated from the Raman spectra. A) Sample A, B) sample A with the y-axis maximum changed to ten counts so that the lower counts at higher crystallite size are visible, C) Sample B, D) Sample B with y-axis maximum of 10 counts, E) Sample C and F) Sample C with y-axis maximum of 10 counts

The variation in electrical conductivity for baseline A and baseline B samples indicates that there are effects other than the addition of carbon that can cause a change in electrical conductivity. The most likely explanation is the persistence of porosity and voids in the samples.

Despite the modification to the processing system to de-gas aluminum by flowing argon through the molten material via the stirrer, macroscopic voids were still present in the final sample, shown in the photographs in Figure 5.5. Even in a cross-section of the baseline sample, shown in

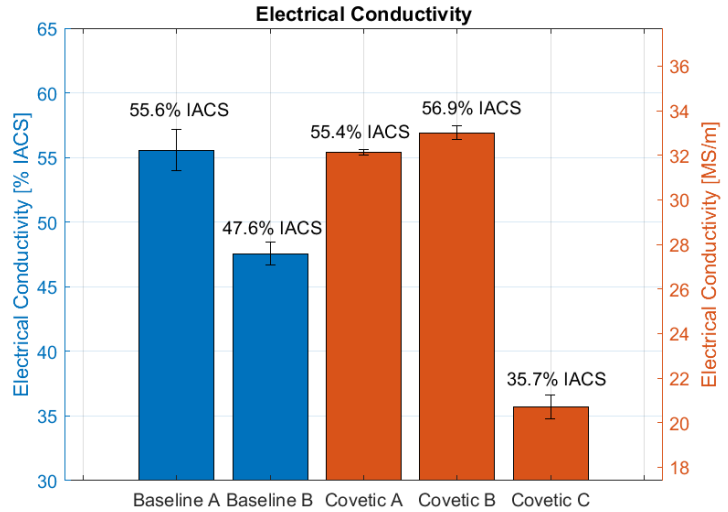


Figure 5.4. Electrical conductivity measured from the two baseline samples and three covetic samples.

Figure 5.5.A., there is a visible large pore about 1 cm long. The macroscale void content in the covetic samples, shown in Figure 5.5.B. and 5.5.C. is even greater. The microscale void content

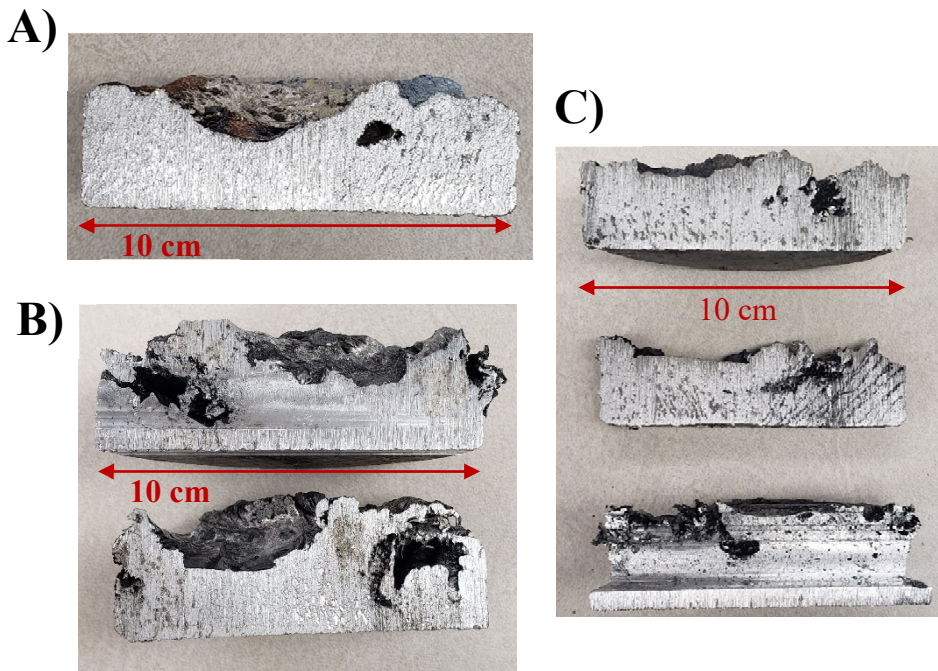


Figure 5.5. Photographs of the interior cross-sections of A) the baseline sample B) Sample A and C) Sample B. All three samples show voids, with the covetics showing higher porosity.

determined from density measurements was ~10% in covetic samples made by a similar process, and baseline samples showed no microscopic voids (fully dense) in areas selected away

from the macroscopic voids.

For the covetic samples that contain carbon, solute segregation of carbon could be a source of porosity, discussed further in Section 3.4.1. In the baseline sample where carbon was not added, solidification shrinkage could have been the source of the void content. In cast specimens, solidification shrinkage occurs because the density of liquid phase is lower than the solid phase. As the material transforms from liquid to solid, it occupies a smaller volume of space, and contraction of the material can cause pore formation¹⁰⁹. The presence of porosity and voids would lower the electrical conductivity of the samples, consistent with the fact that all of the samples showed lower conductivity than the expected value for AA-1350, 62% IACS¹¹⁷. Potentially the significant difference in electrical conductivity for the two baseline samples was a result of different void content in each sample. Metallurgical effects such as grain size, solute distribution, precipitate formation, etc. could also contribute some variation to electrical conductivity, as the samples were taken from slightly different locations in the cast sample.

5.5. Conclusions and Future Work

Modifications were made to the covetics processing system to attempt to minimize oxide content and void formation. The activated carbon starting material was de-gassed in a vacuum furnace prior to processing, the stirring speed was increased to 700-800 rpm, and argon was fed through the molten material through the stirring shaft. Three AA-1350 covetic samples with 3 wt% C were made using the updated system, varying applied current, stirring speed, and argon flow time. The average graphitic carbon crystallite size in the covetic samples did not increase compared to the activated carbon starting material. The electrical conductivity of the three covetic samples did not show an improvement relative to the baseline sample with no added carbon or application of current.

Despite the modifications to the processing system, porosity was still present in the covetic and baseline samples, which degraded electrical conductivity. In future work, the issue of carbon solute segregation in the cast material could potentially be addressed by quenching the material. By rapidly solidifying the material in a quenching process, the kinetics are manipulated so that the system does not have time to move toward thermodynamic equilibrium during cooling, which could help prevent the aggregation of carbon that occurs as the covetic sample cools slowly. This could also result in a reduction in grain size, which would lower the electrical conductivity of the sample. These effects highlight the metallurgical complexity of the system as it relates to solidification, heat treatment, and post-processing and illustrates the need for a procedure designed to maximize homogeneity of the carbon and electrical conductivity of the sample.

Chapter 6: Micromechanics of an IM7/PEEK Laminate with Added Copper Mesh Layers

6.1. Motivation and Objectives

In composite materials, mechanical properties of the composite are primarily dictated by the microscale nature of the interface between the reinforcement phase and the matrix⁴⁶. Interfacial shear stress transfer between the matrix and reinforcement phase affects the overall mechanical properties of the composite. As a result, understanding the microscale interfacial properties is key to determining the macroscale mechanical properties of the composite. In CFRPs, an interphase region exists where there is chemical bonding between the fiber and the polymer matrix, which leads to an effective volume fraction of reinforcement that is larger than the actual volume fraction of the carbon fiber reinforcement¹²⁷. Poor interfacial strength between fibers and matrix will lead to low bulk shear strength, which is typically measured by single fiber pull out test; however, sample preparation is tedious and there is disagreement over the ideal test set-up¹²⁸. Nanoindentation has emerged as a useful technique to characterize the mechanical properties of this interphase region and how it changes as a result of processing or damage due to the ability to rapidly test many fibers^{129–135}. Understanding how processing methods affect the interphase region is key to predicting the overall mechanical performance of the composite. Developing methods of using nanoindentation to achieve more robust characterization of the interphase region and interfacial properties of CFRPs would assist in this endeavor.

The objectives of this work were to use nanoindentation to (1) understand the effect of annealing of the PEEK matrix on the mechanical properties of the fiber/PEEK interphase region, and (2) determine to what extent the copper mesh may act as a reinforcement phase or source of

weakness in the multifunctional composite. It has been demonstrated that the mechanical properties of PEEK can vary depending on the crystallinity of the polymer, with higher tensile strength and elastic modulus for higher crystallinity, and that the degree of crystallinity can vary depending on the thermal history of the PEEK^{136–139}. In CFRP composites with a PEEK matrix, the crystallinity of PEEK can affect the interfacial adhesion, with better adhesion for higher PEEK crystallinity at the interface^{138–142}. Thus, an annealing procedure was carried out and nanoindentation was used to determine if the annealing procedure enhanced the interfacial adhesion and extended the interphase region at the fiber/PEEK interface. With regards to the copper mesh, copper could potentially act as a reinforcement phase if there is sufficient interfacial bonding due to its higher strength and elastic modulus compared to the PEEK; however, it is possible that a lack of interaction between Cu/PEEK could result in minimal reinforcement. Thus, nanoindentation was used to assess the interfacial adhesion between Cu/PEEK and determine whether the copper mesh is acting as a reinforcement phase.

6.2. SEM and X-ray CT of CFRP laminate with Cu Mesh

The sample tested by nanoindentation was received from SURVICE and consisted of a unidirectional CFRP laminate with two copper mesh layers. The carbon fibers were IM7, and the polymer matrix was polyether-ether ketone (PEEK). A cross-sectional SEM micrograph of the sample is shown in Figure 6.1.A. The laminates consisted of unidirectional continuous carbon fiber plies with different relative orientations of the fibers in each layer, shown in Figure 6.1.B, where three CFRP layers with different fiber orientations can be seen. The top and bottom layers have fibers oriented normal to the cross-sectional sample surface and the center layer has fibers oriented in the transverse direction. A schematic showing the general geometry of the CFRP sample with layers containing different in-plane relative fiber orientation is shown in Figure

6.1.C. The fibers in each ply were oriented in either the 90° , 0° , $+45^\circ$, or -45° direction. Nanoindentation was performed around the fibers in the layers where the fibers are oriented normal to the sample surface. The two copper mesh layers had different in-plane relative orientations, with one rotated 45° relative to the other, shown by the X-ray micro-CT 3D

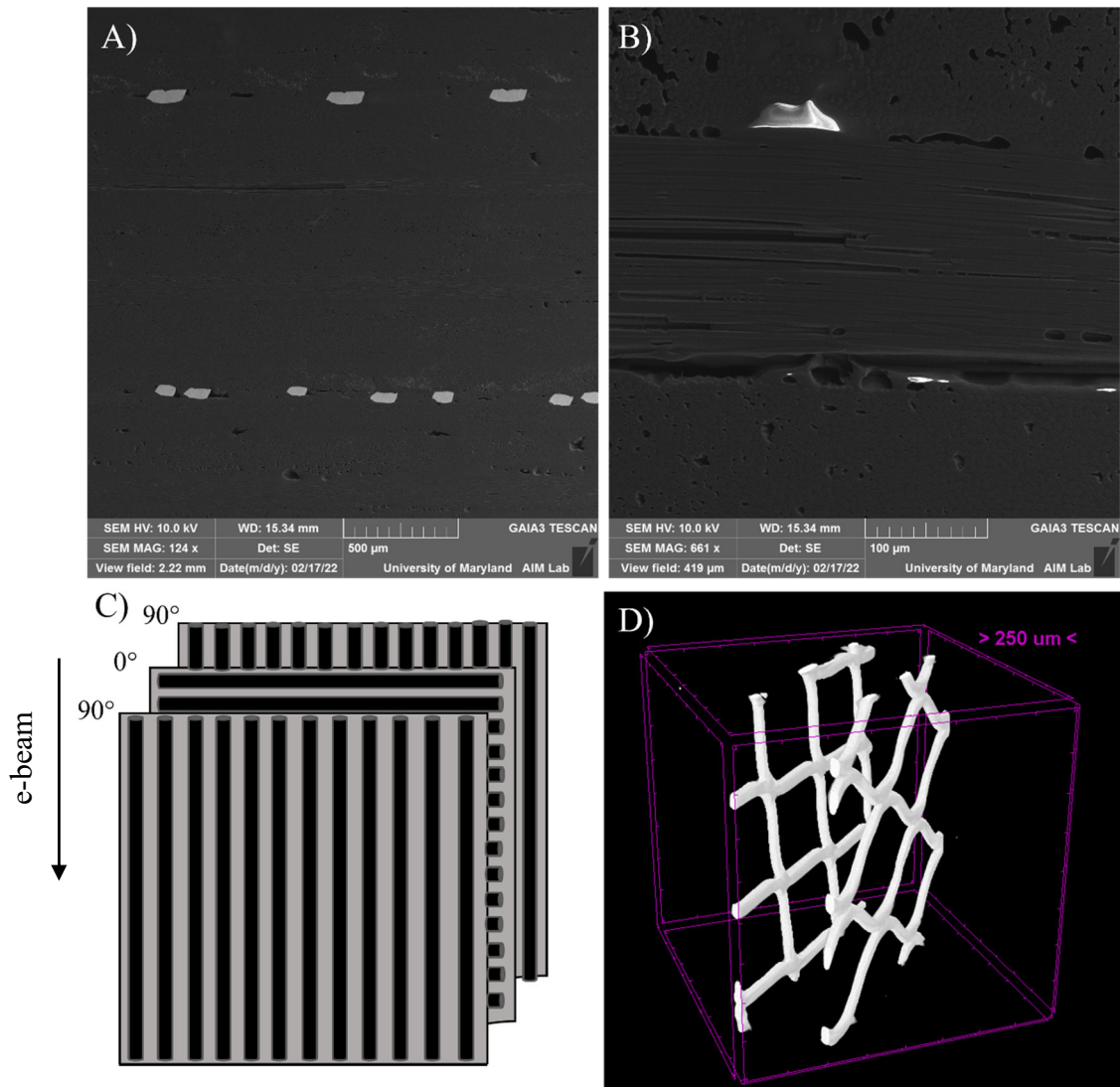


Figure 6.1.A) Cross-sectional SEM micrograph of the multifunctional composite showing three CFRP layers and two copper (bright areas) mesh layers. B) Three CFRP layers with different relative fiber orientations showing normal to the page in the top and bottom layer and fibers parallel to the page in the center layer. C) Schematic of fiber orientations in the micrograph. D) X-ray CT image showing the two copper layers with 45° relative orientation between the layers.

reconstruction in Figure 6.1.D. Nanoindentation was performed with basal plane of the mesh oriented normal to the sample surface, as shown in the micrograph in Figure 6.1.A.

6.3. Annealing Effects on Raman Spectra of PEEK

To understand the effects of processing on the interface mechanical properties and reinforcement ability of the carbon fibers, the composite sample was annealed at 200°C for 1 hour in air at ambient pressure in an oven. The sample was cooled in the oven, which took 1 hour for the sample to return to room temperature. The annealing protocol was selected following the work of Yang et al.¹⁴³

The crystallinity of PEEK before and after annealing was calculated using Raman spectroscopy from the peak shift of the 1651 cm⁻¹ Raman peak. This indicator was chosen following the work of Doumeng et al.¹⁴⁴, which evaluated the correlation coefficient for 18 Raman indicators and percent crystallinity calculated by DSC and found that S, the 1651 cm⁻¹, peak position had the highest correlation coefficient (r=0.92). The equation relating S and X_c, percent crystallinity is

$$X_c = -3478(S) + 5765.2 \quad (6.1)$$

To calculate the average percent crystallinity before and after annealing, 30 Raman spectra were collected and the position of the 1651 cm⁻¹ peak was found using the MATLAB “findpeaks” function. A representative Raman spectrum is shown in Figure 6.2.A, where the red asterisk indicates the 1651 cm⁻¹ peak used as an indicator of crystallinity. The average percent crystallinity before and after annealing is shown in Figure 6.2.B. It can be seen that the average percent crystallinity did not change as a result of the annealing process, from 40.6 +/- 6.9% before annealing to 41.4 +/- 5.5% after annealing. Given that the typical crystallinity of

commercial PEEK is 30-40%¹⁴⁵, it is reasonable to assume that the relatively high initial crystallinity is what led to the lack of further increase from the annealing procedure.

6.4. Nanoindentation Results as a Function of Distance from Fiber/Cu

6.4.1. Histograms of Nanoindentation Results

To investigate the mechanical properties of the composite near the interface of C fiber/PEEK and Cu/PEEK, nanoindentation was performed in the area surrounding the filler phases. Five 6x6 indent arrays were performed in the three regions: (1)

near carbon fibers before annealing, (2) near carbon fibers after annealing, and (3) near copper mesh before annealing. The loading rate, hold time at max load, and unloading rate were selected to minimize the rate-dependent effects of PEEK viscoelasticity, by using a slow indentation strain rate (0.025 1/s) and longer hold sequence at max load (30 s)^{123,146,147}. The indents were performed in displacement control mode to 300 nm depth. The reduced elastic modulus and hardness were calculated from the Oliver-Pharr method^{120,121}, discussed in Section 4.2.4. To summarize, the reduced elastic modulus, E_r , is calculated from

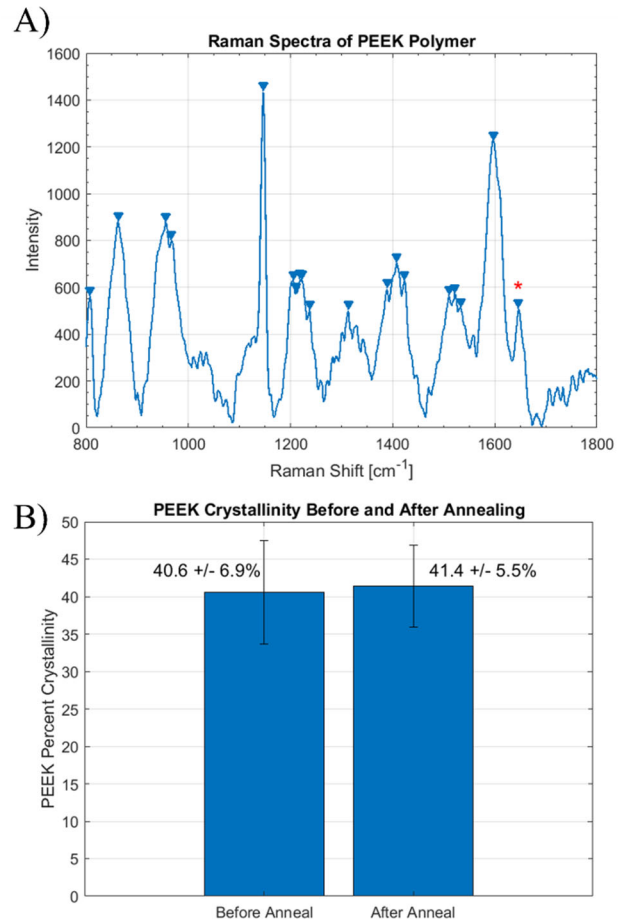


Figure 6.2.A) Representative Raman spectrum collected from the PEEK matrix. The red asterisk indicates the 1651 cm⁻¹ peak used to calculate percent crystallinity of PEEK. B) PEEK crystallinity calculated from the Raman data before and after the annealing procedure

$$S = \beta \frac{2}{\sqrt{\pi}} E_r \sqrt{A_c} \quad (6.2)$$

where S is the slope from a linear fit of the initial unloading curve, dP/dh , β is a geometric shape factor, and A_c is the contact area. Hardness is calculated using

$$H = \frac{P_{max}}{A_c} \quad (6.3)$$

where P_{max} is the maximum load.

Histograms of the reduced elastic modulus and hardness calculated from the indents in each of the three areas are shown in Figure 6.3. Each area had a population of 180 indents, from the five 6x6 indent arrays. In each of the three areas, the distributions skew towards lower reduced elastic modulus and hardness, which was expected as the majority of indents occurred on the PEEK matrix, which has lower modulus and hardness than both the carbon fibers and copper. The indents from the populations near the carbon fibers (Figure 6.3 A-D) show a range

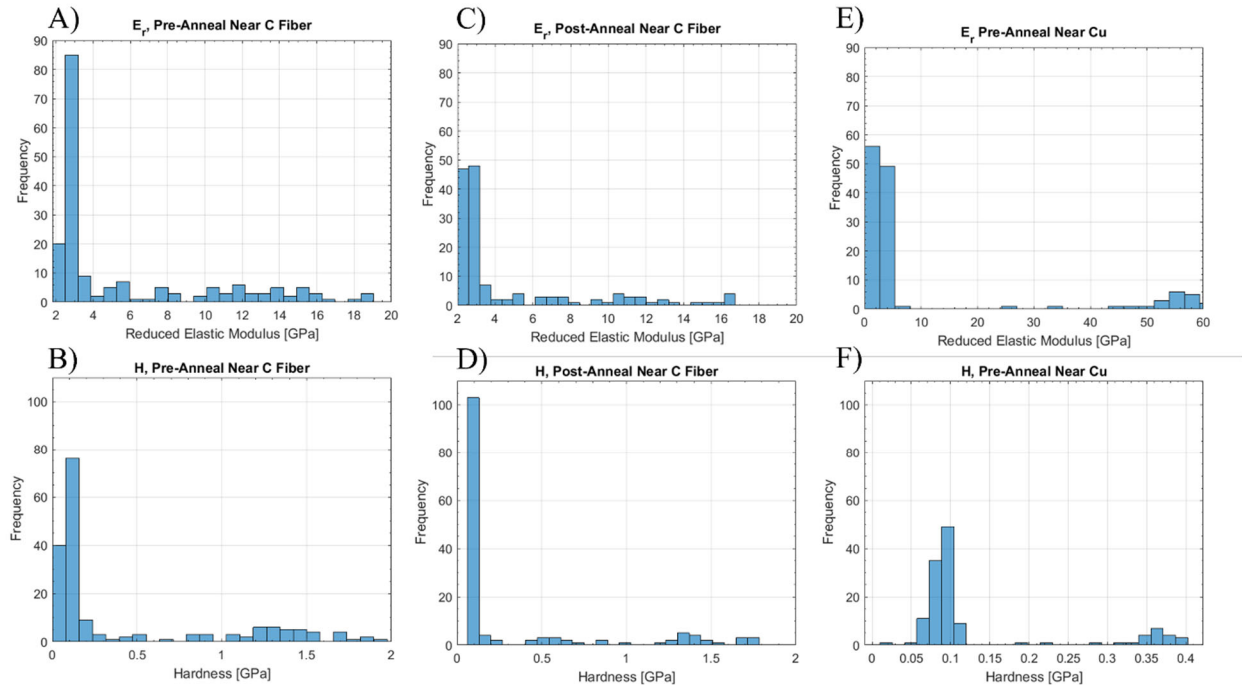


Figure 6.3 Histograms of nanoindentation results from the three areas, A) Reduced elastic modulus pre-anneal near fiber, B) Hardness pre-anneal near fiber, C) Reduced elastic modulus post-anneal near fiber, D) Hardness post-anneal near fiber, E) Reduced elastic modulus pre-anneal near Cu and F) Hardness pre-anneal near Cu.

of increased modulus/hardness which corresponds to the indents that were influenced by the carbon fiber reinforcement. There is no apparent difference between the data near the carbon fibers before and after annealing. In contrast, the histogram of indents near the copper mesh (Figure 6.3 E and F) do not show this same range of increased modulus/hardness, instead there appears to be two discrete clusters of lower and higher modulus/hardness. The lower cluster is from the indents that occurred on the PEEK matrix, and the higher cluster is the indents that occurred on the copper. In the following sections, these observations are further investigated by plotting the reduced elastic modulus and hardness as a function of distance from the fiber/Cu to make inferences about the strength of the interface between carbon fiber/PEEK and Cu/PEEK.

6.4.2. Measurement of Distance from Fiber/Cu Edge from SPM

To measure the distance from each indent to the edge of carbon fiber/Cu SPM micrographs were collected of each indent array after indentation. Representative micrographs showing the indent arrays are shown in Figure 6.4. An array around carbon fibers is shown in Figure 6.4.A and B. and an array around the copper mesh cross-section is given in Figure 6.4.C and D. ImageJ was used to measure the distance between each indent and the nearest carbon fiber/Cu edge. The results were used to plot reduced elastic modulus and hardness as a function of distance from carbon fiber/Cu edge and assess the reinforcement ability of the carbon fibers before and after annealing, and the reinforcement ability of the carbon fibers compared to the copper mesh.

To investigate the effect of annealing on the PEEK matrix and fiber/PEEK interface, the modulus and hardness as a function of distance from the nearest fiber were analyzed. In Figure 6.5, the reduced elastic modulus and hardness are plotted as a function of distance from the nearest carbon fiber. It can be seen that the modulus and hardness both increase as the indents

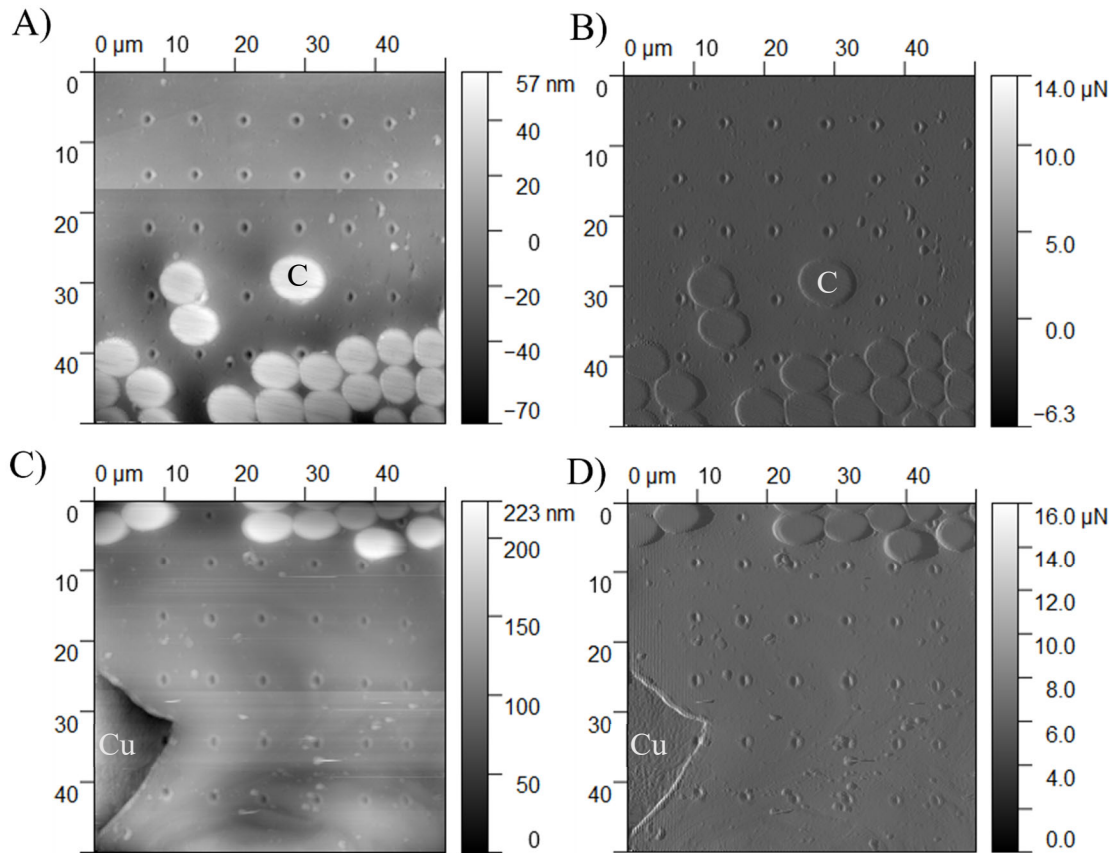


Figure 6.4 Scanning probe micrographs collected using the nanoindentation piezo-scanner showing the indentation arrays. A) Topography image near carbon fibers B) Gradient image near carbon fibers, C) Topography image near Cu, and D) Gradient image near Cu.

approach the fiber/matrix interface. The modulus and hardness in the region > 3 microns away from the fiber edge is relatively constant and corresponds to the reduced elastic modulus and hardness of the PEEK matrix without any reinforcement effects from the carbon fibers.

The data was split into two groups: (1) the matrix phase $> 5 \mu\text{m}$ away from the fiber edge and (2) the fiber and interface region $< 5 \mu\text{m}$ away from the fiber edge and on the fiber to determine the change in modulus/hardness in the matrix only. The average reduced elastic modulus and hardness in these two regions before and after annealing are shown in Figure 6.6. There was a slight increase in the hardness of the matrix after annealing, from 0.081 ± 0.012 GPa to 0.103 ± 0.014 GPa ($P=.05$). There was no change in the reduced elastic modulus of the

matrix, from 2.64 +/- 0.17 GPa to 2.60 +/- 0.18 GPa after annealing. There was a larger variance in the reduced elastic modulus and hardness of the fiber/interface region due to the variation with distance from the fiber edge in this region. Consequently, there was no observed change in the average reduced elastic modulus (3.90 +/- 2.06 GPa to 3.75 +/- 1.78 GPa after annealing) or hardness (0.161 +/- 0.153 GPa to 0.200 +/- 0.197 GPa after annealing) in the fiber/interface region. Thus, the annealing protocol resulted in a small increase in the PEEK matrix hardness, but the reduced elastic modulus was unchanged.

6.4.3 Nanoindentation: Comparison of CFRP Interface Region Before and After Annealing

The large variance in reduced elastic modulus and hardness in the fiber/interface region made it difficult to assess the interfacial strength before and after annealing by average values

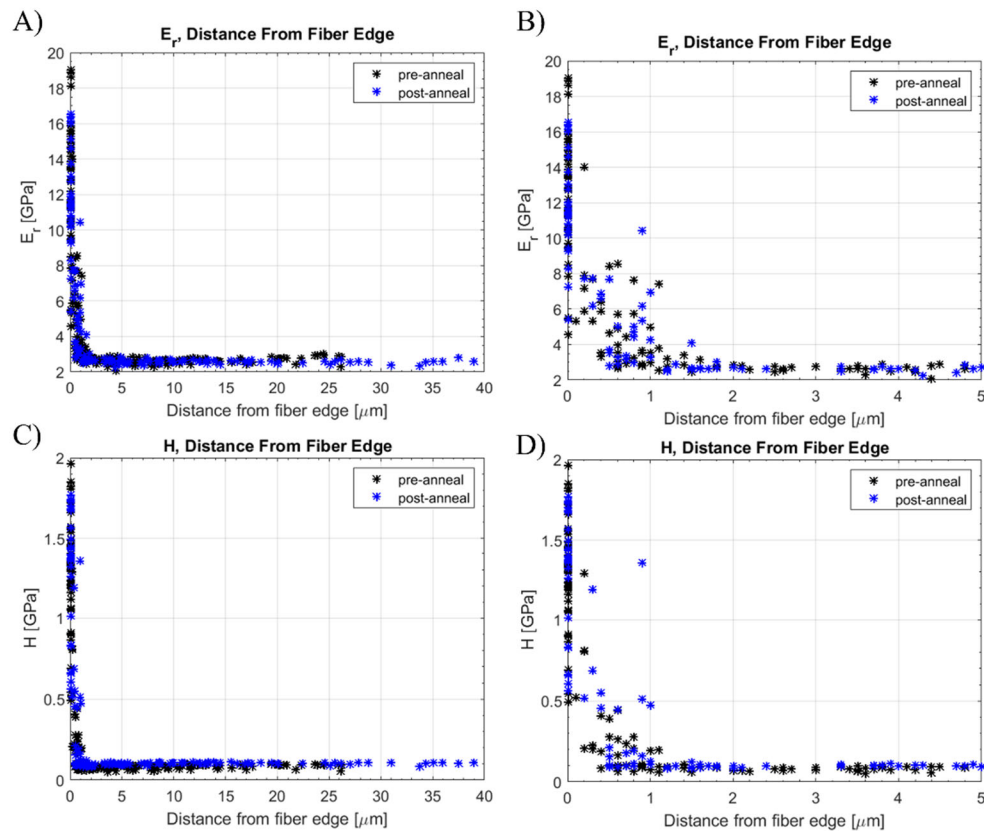


Figure 6.5. Nanoindentation results as a function of distance from the carbon fiber edge before and after annealing. A) Reduced elastic modulus for all data points, B) Reduced elastic modulus in the region <math>< 5 \mu\text{m}</math> from the fiber edge, C) Hardness for all data points, and D) Hardness in the region <math>< 5 \mu\text{m}</math> from the fiber edge.

alone. Thus, a power law function was fitted to the reduced elastic modulus and hardness as a function of distance from the fiber edge using the MATLAB Curve Fitting Toolbox to evaluate the trend in modulus/hardness increase as the indenter approaches the edge of the fiber. The exponent of the fitted power law function can be used to compare the rate of decay of the reinforcement effect of the fiber as the distance from the fiber is increased.

A decreased rate of decay would indicate that the fiber is more effectively reinforcing the matrix due to enhanced interfacial bonding and interfacial shear strength, leading to a larger interphase region. For indents in the matrix near the carbon fiber edge, as the interaction volume of material deforming under the indenter tip expands and reaches the carbon fiber, effective load transfer at the fiber/PEEK interface impedes deformation and increases modulus and/or hardness. A rapid drop in modulus/hardness as indents enter the matrix would indicate that there was not effective interfacial bonding and reinforcement between the fiber and the matrix, resulting in a

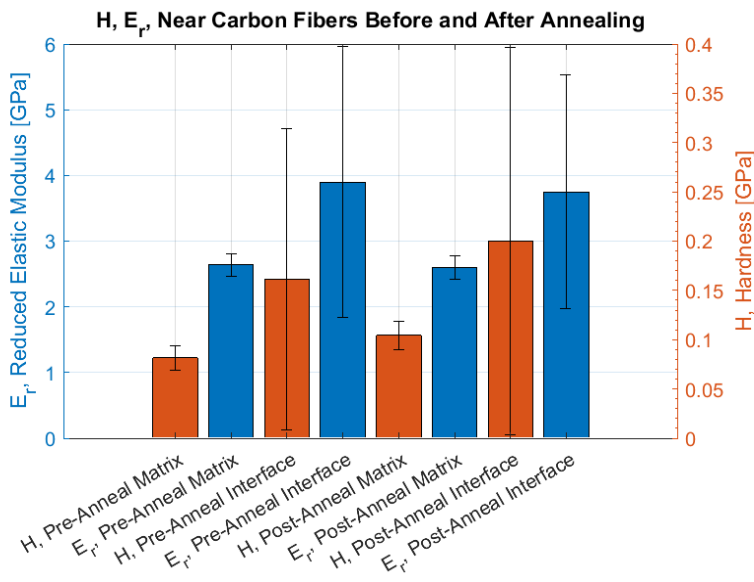


Figure 6.6. Average reduced elastic modulus and hardness in the matrix and interface regions. The interface region was defined as data points $< 5 \mu\text{m}$ from the fiber edge and the matrix region was defined as data points $> 5 \mu\text{m}$ from the fiber edge.

smaller area of the matrix that is reinforced by the carbon fiber. In this case, as the interaction volume of material deforming under the indenter tip reaches the carbon fiber, there is not effective strain transfer, and PEEK flows unimpeded along the fiber surface with little change in modulus/hardness. Thus, the trend in modulus/hardness as a

function of distance from the fiber edge can be used to assess the interfacial bonding and the size of the interphase region of the fiber/PEEK interface before and after annealing.

The fitted curves for reduced elastic modulus and hardness are shown in Figure 6.7. The shaded regions indicate the error in the fit for the curves based on a 95% confidence interval. It can be seen from the plot of reduced elastic modulus vs. distance from fiber edge in Figure 6.7.A that there was no change in elastic properties in the interface region as a result of the annealing procedure. The exponent of the power law functions was un-changed as a result of the annealing process, from -3.505 ± 0.801 to $-$

2.992 ± 0.665 . This is consistent with the observation that the matrix values of reduced elastic modulus did not change as a result of the annealing process. The hardness,

however, appeared to show a decrease in the rate of decay as

distance from the fiber edge increases, shown in Figure 6.7.B,

with the post-anneal curve lying above the pre-anneal curve. The power law exponent decreased from -5.215 ± 1.239 to -3.763 ± 1.036

after annealing. The results indicate that there was a slight increase in the

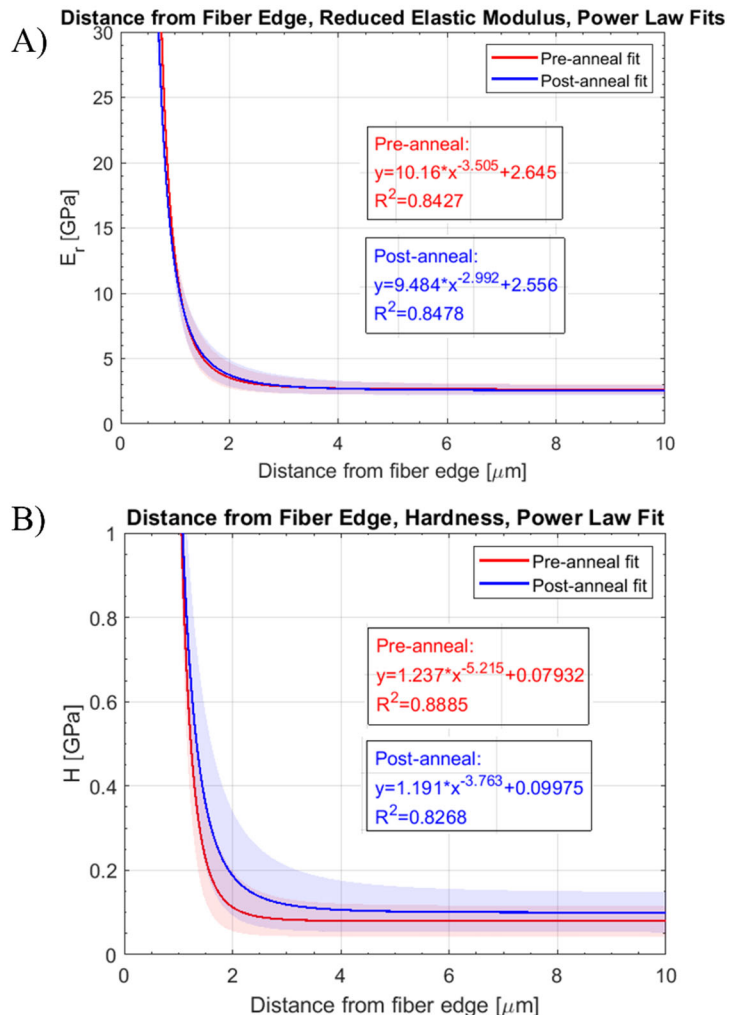


Figure 6.7 Power law fits for A) reduced elastic modulus and B) hardness as a function of distance from the fiber edge before and after annealing.

reinforcement ability of the carbon fiber as a result of the annealing process with an increase in the span of the interphase region, though the difference is small. Given that the crystallinity was not shown to significantly change as a result of the annealing process and that the increase in hardness in the matrix was small while the modulus was unchanged, the modulus/hardness at the interface would not be expected to significantly change, either.

6.4.4. Nanoindentation: Comparison of CFRP to Copper Interface Region

The reduced elastic modulus and hardness near the copper mesh in Figure 6.3 E and F were also plotted as a function of distance from the copper edge, shown in Figure 6.8. It can be seen that the hardness, shown in Figure 6.8.A and 6.8.B, and reduced elastic modulus, shown in Figure 6.8.C and 6.8.D do not decrease gradually as distance from the interface is increased, but rather there is an abrupt transition in modulus/hardness as the indents enter the matrix phase. This is consistent with the histograms in Figure 6.3.E and 6.3.F that show two discrete clusters of reduced elastic modulus and hardness values rather than the range of values shown in Figure 6.3.A-D for the indents around the carbon fibers. As a result, the R^2 values of the power law fits for the reduced elastic modulus and hardness as a function of distance from the copper edge, shown in Figure 6.9 are lower than the values for the distance from the carbon fiber. The R^2 values for the reduced elastic modulus and hardness, respectively, as a function of distance from the copper edge were 0.8017 compared to 0.8427 and 0.8478 for the carbon fibers, and 0.6633 compared to 0.8885 and 0.8268 for the carbon fibers, indicating that the power law trend is a less accurate way of representing the data near the copper edge. This also indicates that the copper's ability to reinforce the matrix is not as pronounced as the reinforcement effects of the carbon fiber. There is not a strong interfacial bond at the Cu/PEEK interface, thus the interfacial shear strength is low and there is not effective load transfer between Cu and PEEK.

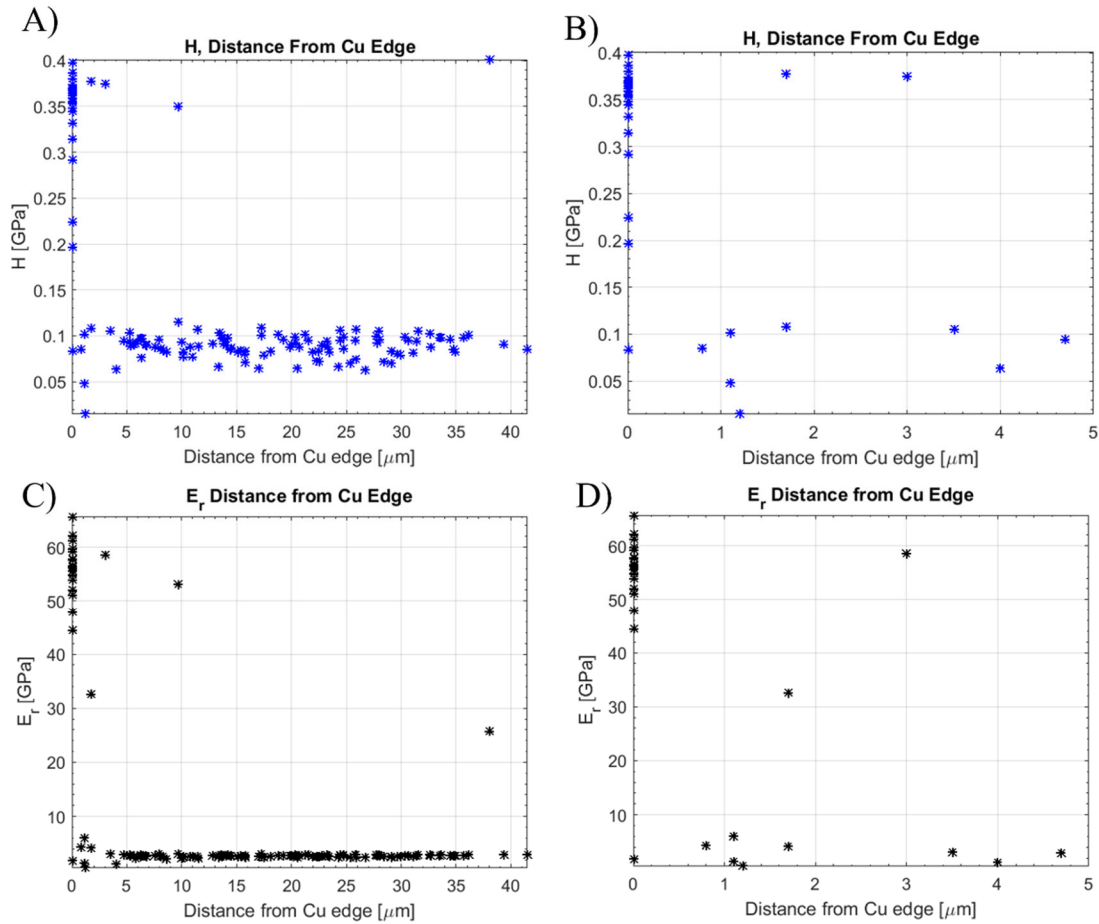


Figure 6.8. Nanoindentation results as a function of distance from the Cu edge before and after annealing. A) Hardness for all data points, B) Hardness s in the region $<5 \mu\text{m}$ from the fiber edge, C) Reduced Elastic Modulus for all data points, and D) Reduced Elastic Modulus in the region $<5 \mu\text{m}$ from the fiber edge.

In CFRP manufacturing, functionalization of the carbon fiber surface and the addition of a sizing layer between the carbon fiber and the matrix are both used to enhance interfacial adhesion^{46,127}. A potential reason why the carbon fibers are a more effective reinforcement phase than the copper could be due to the more developed engineering of the fiber/matrix interface than the Cu/matrix interface. In this work, the copper mesh was incorporated by applying pressure during the assembling of the layers in the composite/copper multifunctional shielding material with the primary goal of enhancing electromagnetic shielding effectiveness of the multifunctional composite. As a result, the interface characteristics of Cu/PEEK and how they

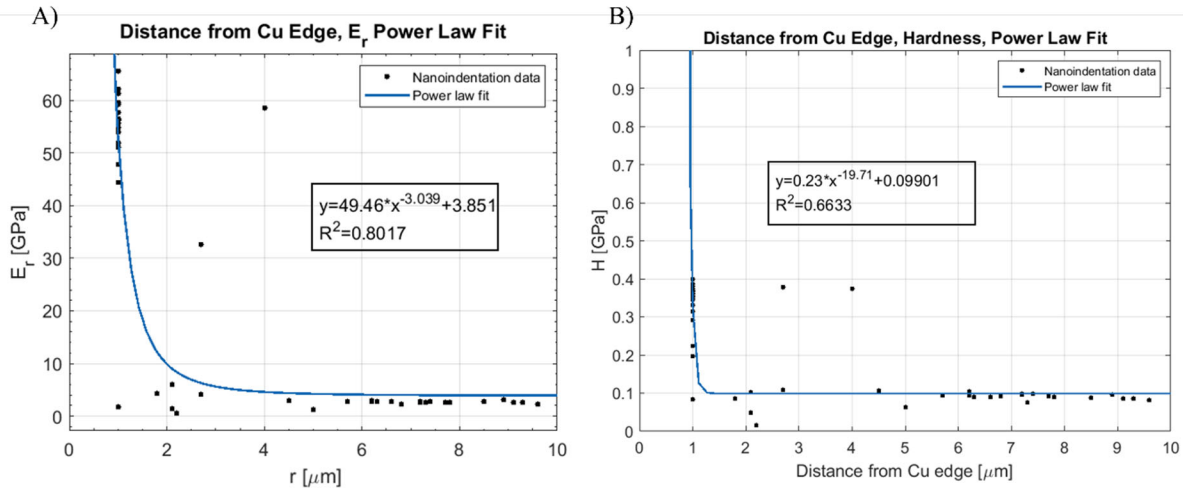


Figure 6.9. Power law fits for A) reduced elastic modulus and B) hardness as a function of distance from the Cu.

pertain to mechanical properties were not designed to the same extent that the fiber/PEEK interface was. Potentially, chemical functionalization of the copper mesh surface prior to incorporation into the CFRP laminate could enhance adhesion between Cu/PEEK. For example, Kim et al.¹⁴⁸ found that Ar⁺ radiation of PEEK in the presence of O₂ gas modified functional groups on the PEEK surface and resulted in enhanced adhesion between PEEK and Cu. If the interfacial adhesion between Cu/PEEK could be enhanced in the multifunctional composite, it would result in the copper mesh acting as a more effective reinforcement phase, thus improving the overall mechanical properties of the multifunctional composite.

6.5. Conclusions and Future Work

Nanoindentation was used to investigate the micro-mechanical properties of a multifunctional composite consisting of a CFRP laminate with additional copper mesh layers. The reduced elastic modulus and hardness were correlated to the distance from the nearest carbon fiber, and copper mesh and results before and after annealing the composite were compared. From Raman results, it was found that the crystallinity of the PEEK matrix was unchanged at ~41% crystallinity before and after annealing. It was found that the hardness in the

matrix increased from 0.081 +/- 0.012 GPa to 0.103 +/- 0.014 GPa ($P=0.05$) as a result of the annealing process. Additionally, fitting a power law function to the data indicated that the rate of decay of hardness as the distance from the fiber increased was lower after annealing, implying that the annealing process may have enhanced the interfacial adhesion and extended the interphase region surrounding the carbon fiber. In contrast, the reduced elastic modulus in the matrix did not change after annealing. The hardness and modulus of the PEEK composite as a function of distance from the copper edge was not well described by a power law function, and instead appeared to be two discrete clusters of higher modulus/hardness on the copper and lower modulus/hardness in the matrix. This implies that there is not adequate interfacial bonding between the copper and PEEK, which results in a limited ability of the copper to act as a reinforcement phase.

Future work would use this data analysis technique to investigate the effect of chemical functionalization on the Cu/PEEK interface. If the interfacial adhesion could be enhanced, the copper would act as a reinforcement phase in addition to providing an electromagnetic shielding function, improving the overall properties of the multifunctional composite. Additionally, the effect of PEEK viscoelasticity on the nanoindentation response could be further investigated using dynamic mechanical analysis (DMA) which would give information about the storage and loss modulus of the material. Knowledge of the complex elastic modulus could potentially give more information about the elastic properties of PEEK near the interface

Chapter 7: Model of Electromagnetic Interference Shielding Effectiveness for the Multifunctional Composite Containing CFRP and Copper Mesh Layers

7.1. Motivation and Objectives

Electromagnetic interference (EMI) shielding enclosures are used to protect sensitive electronic components and control systems from EM radiation that can compromise their functionality. For aerospace applications in particular, minimizing weight of the shield is critical without compromising shielding effectiveness and strength. Utilizing a multifunctional composite that combines multiple functions into a single structure can decrease the overall weight needed to perform both functions⁴⁵. In this work, the multifunctional composite was comprised of a unidirectional CFRP laminate with an added Cu mesh layer. The CFRP laminate was intended as a structural component while the Cu mesh was incorporated to increase the EMI shielding effectiveness (SE). The multifunctional structure contains multiple CFRP plies, each with different relative orientations of the fibers. The Cu mesh is placed between CFRP plies. The overall structure could contain more than one Cu mesh with different relative in-plane orientation between them and for different separations (thickness of the CFRP composite) between Cu mesh layers.

More efficient design of the optimal laminate lay-up could be achieved if the structure could be modeled for different stacking of plies with different fiber orientations and placement of the Cu mesh layers. Prior theoretical work studying the shielding effectiveness of carbon fiber composites has primarily been concerned with woven carbon fiber fabrics^{60,71,95,149–153}, while less attention has been given to unidirectional carbon fiber composites^{94,154}. Additionally, it is unclear

how the choice of placement of the Cu mesh in the CFRP lay-up affects SE. Thus, the objective of this work is to design a finite element model that simulates the SE of different arrangements of the multifunctional composite structure. This would aid in more efficient design of a multifunctional structure with improved SE compared to the fabrication and experimental testing of each proposed structure.

7.2. Calculation of Shielding Effectiveness from the COMSOL Model

Shielding effectiveness (SE) can be calculated by considering it as a transmission line problem, following the approach proposed by Schelkunoff⁵⁴. The basic theory of electromagnetic shielding is presented in Section 1.7 and summarized here. Reduction of the electromagnetic field by a shield material occurs due to three main factors: reflection of the wave at the interface between media due to a difference in impedance, and absorption loss due to Ohmic loss and polarization loss⁵⁵. By considering the problem as analogous to a transmission line, the shielding effectiveness can be calculated by adding each contribution. SE in decibels (dB) is a measure of the reduction in amplitude of the electromagnetic wave transmitted through the medium given by⁵⁵

$$SE = 20\log\left(\frac{E_{initial}}{E_{transmitted}}\right) = 20\log\left(\frac{H_{initial}}{H_{transmitted}}\right) = 10\log\left(\frac{P_{initial}}{P_{transmitted}}\right) = R + A + B \text{ [dB]} \quad (7.3)$$

where E is the amplitude of the electric field, H is the amplitude of the magnetic field, and P is the power. R, A, and B are the values of reflection loss, absorption loss, and internal reflection correction factor, respectively, measured in decibels.

To calculate the shielding effectiveness in COMSOL, the RF module was used with the Electromagnetic Waves, Frequency Domain physics interface, which solves for the time-harmonic electric field using Maxwell's Equations. The model consists of a waveguide with two ports on each end and the shield placed in the middle, shown in Figure 7.1. Port 1 is the

transmitter that excites the initial electromagnetic wave and Port 2 is the receiver after the signal goes through the shielding material. Periodic Floquet boundary conditions were applied to the remaining four faces to construct the unit cell of a semi-infinite model, with the k-vector for Floquet periodicity corresponding to the k-vector of Port 1, the excitation port. The model solves for electric field as the dependent variable, and calculates the reflection and transmission coefficients, S_{11} and S_{12} , respectively, of the two-port network to calculate shielding effectiveness.

The electric field is solved using Maxwell's equations and constitutive relations. The general, time-varying Maxwell's equations are given by^{155,156}

$$\nabla \times H = J + \frac{\partial D}{\partial t} \quad (\text{Maxwell-Ampere's Law}) \quad (7.4)$$

$$\nabla \times E = -\frac{\partial B}{\partial t} \quad (\text{Faraday's Law}) \quad (7.5)$$

$$\nabla \cdot D = \rho \quad (\text{Gauss's Law, electric form}) \quad (7.6)$$

$$\nabla \cdot B = 0 \quad (\text{Gauss's Law, magnetic form}) \quad (7.7)$$

where J is the current density. D is the electric displacement field, B is the magnetic flux density, and ρ is the electric charge density. Additionally, the equation of continuity is given by^{155,156}

$$\nabla \cdot J = -\frac{\partial \rho}{\partial t}. \quad (7.8)$$

Out of the previous five equations, only three are independent. Maxwell-Ampere's and Faraday's Law can be combined with either the electric form of Gauss's Law or the continuity equation to form an independent system. Additionally, the relevant constitutive equations assuming linear media are^{155,156}

$$D = \epsilon_0 \epsilon_r E \quad (7.9)$$

$$B = \mu_0 \mu_r H \quad (7.10)$$

$$J = \sigma E \quad (7.11)$$

where ϵ_0 is the vacuum permittivity (8.85×10^{-12} F/m), ϵ_r is the relative permittivity of the medium, μ_0 is the vacuum permeability ($4\pi \times 10^{-7}$ H/m), μ_r is the relative permeability of the medium, and σ is the electrical conductivity of the medium. Maxwell's equations, the continuity equation, and the constitutive relations are used to formulate the equation solved by COMSOL, the time-harmonic equation in phasor notation for electric field assuming a sinusoidal excitation given by¹⁵⁵

$$\nabla \times \mu_r^{-1}(\nabla \times E) - k_0^2(\epsilon_r - \frac{j\sigma}{\omega\epsilon_0})E = 0 \quad (7.12)$$

where k_0 is the free-space wave number, j is the imaginary unit ($\sqrt{-1}$), and ω is the angular frequency of the EM wave. The electric field, E , is the dependent variable, and the EM wave frequency (ω) and material properties (μ_r , ϵ_r , σ) are model inputs. Field continuity boundary conditions are enforced at the interfaces between the different components of the shielding material including the interface between air and the first layer of material.

Once the electric field has been calculated, the reflection (S_{11}) and transmission (S_{21}) coefficients of the two-port network can be calculated and used to calculate shielding effectiveness. The reflection coefficient, S_{11} , indicates the ratio of electric field amplitude of the wave reflected back to Port 1 to the initial excitation wave, given by⁵⁸

$$E_{Port\ 1} = E_1 + S_{11}E_1 \quad (7.13)$$

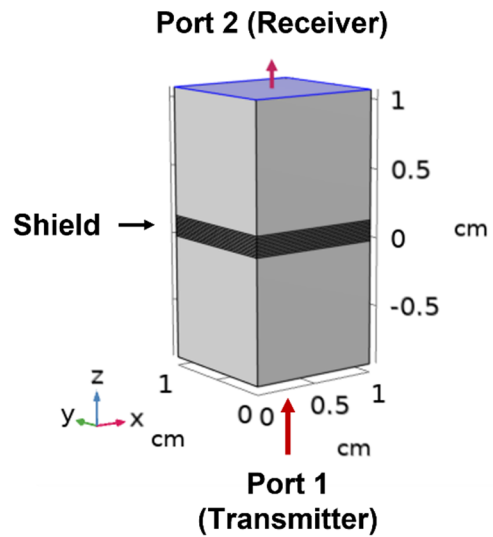


Figure 7.1. Geometry of the EM shielding model where Port 1 is the transmitter generating the EM wave and Port 2 is the receiver. The shield is placed between the two ports. Periodic boundary conditions were applied to the remaining four faces of the model to generate a semi-infinite shield in the x and y directions.

where $E_{Port 1}$ is the power-normalized eigenmode expansion of the electric field at Port 1. E_1 is the fundamental mode of the excitation electric field at Port 1. A linearly polarized EM wave with a magnitude of 1 V/m in x , y , and z was used for E_1 in the model, with a power of 10 W. The first term represents the initial excitation wave, and the second term represents the reflected component. The transmission coefficient, S_{12} , is given by⁵⁸

$$E_{Port 2} = S_{12}E_1 \quad (7. 14)$$

which represents the portion of the initial excitation wave, E_1 , that transmits through the shield and reaches Port 2. S_{11} and S_{12} are both complex, scalar values that can be represented in decibels by

$$S_{11,dB} = 20 \log_{10}(|S_{11}|) \quad (7. 15)$$

$$S_{12,dB} = 20 \log_{10}(|S_{12}|) \quad (7. 16)$$

The shielding effectiveness in terms of $S_{12,dB}$ is given by

$$SE = S_{12,dB,without shield} - S_{12,dB,with shield} = -S_{12,dB,with shield} \quad (7. 17)$$

assuming that there is no attenuation of the electric field without a shield so $S_{12}=1$ and $S_{12,dB}=0$.

Additionally, the SE components associated with reflection, SE_R , and absorption, SE_A , can be calculated by⁵⁶

$$SE_R = R = 10 \log_{10} \left(\frac{1}{1-|S_{11}|^2} \right) [dB] \quad (7. 18)$$

$$SE_A = A = 10 \log_{10} \left(\frac{1-|S_{11}|^2}{|S_{12}|^2} \right) [dB] \quad (7. 19)$$

Thus, the shielding effectiveness of the multifunctional composite can be determined through calculation of the electric field, reflection, and transmission coefficients in COMSOL at a given frequency. The frequency range considered in this work is from radiofrequency regime (~ 50 MHz) through the super high frequency microwave regime (~ 10 GHz). For reference, the wavelength in this frequency range is given in Figure 7.2. The relevant material properties

necessary for the model are permittivity, magnetic permeability, and electrical conductivity. For the CFRP laminate, rather than explicitly modeling the geometry of graphite fibers in a polymer matrix, the material properties were approximated by homogenizing each ply into a homogeneous, anisotropic material and using rotation matrices to model the different relative fiber orientation in each ply. The Cu mesh was represented by using an analytical expression for sheet impedance of a wire mesh⁹⁶ and inserting a layer with an impedance boundary condition into the model. The shielding effectiveness for different CFRP laminate lay-ups, mesh material and mesh open area were compared.

7.3. Shielding Effectiveness of CFRP Laminate

7.3.1. Homogenization of Material Properties

The material properties of the unidirectional CFRP plies were homogenized to reduce the amount of computer memory necessary to solve the model, summarized in Table 7.1. Both the IM7 graphite fibers and PEEK polymer matrix are non-magnetic, so the magnetic properties were assumed to be isotropic with $\mu_r=1$. However, the electrical properties were anisotropic due to the high conductivity in the fiber direction (σ_L) and lower conductivities in the transverse

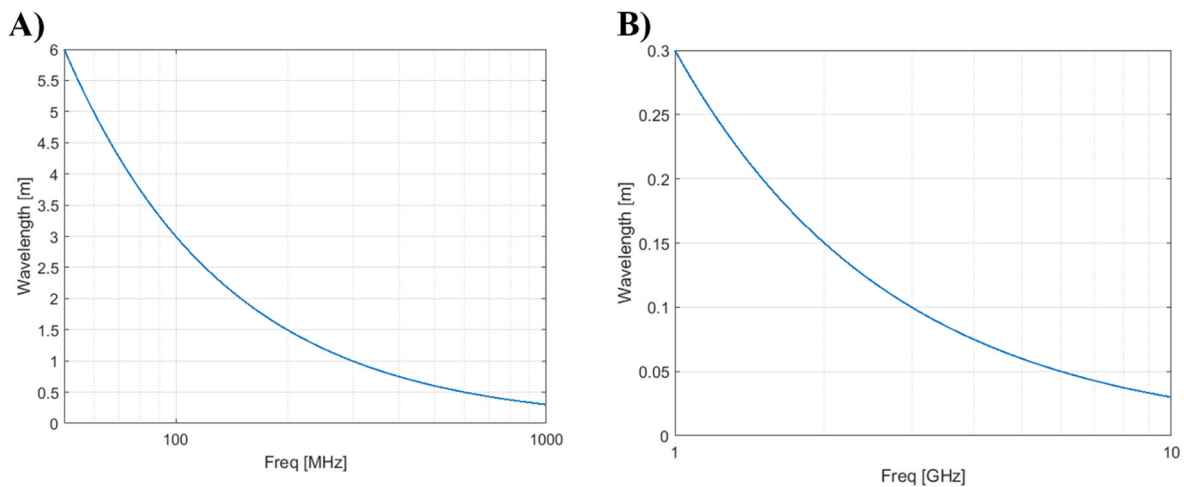


Figure 7.2. Plot of wavelength at a given frequency in the range A) 10 MHz to 1000 MHz (1 GHz) and B) 1 GHz to 10 GHz.

Table 7.1. Summary of the material properties used for each CFRP ply

Property	Isotropic/Anisotropic	Scalar/Complex	Value
μ	Isotropic	Scalar	$\mu_0=4\pi \times 10^{-7}$ H/m
σ	Anisotropic	Scalar	$\sigma_{\theta \text{ orientation}} = \begin{bmatrix} \sigma_L * \cos^2\theta + \sigma_T * \sin^2\theta & \frac{\sigma_L - \sigma_T}{2} \sin(2\theta) & 0 \\ \frac{\sigma_L - \sigma_T}{2} \sin(2\theta) & \sigma_L * \sin^2\theta + \sigma_T * \cos^2\theta & 0 \\ 0 & 0 & \sigma_{CP} \end{bmatrix} [S/m]$ $\sigma_L=4 \times 10^4 \text{ S/m}, \sigma_T=\sigma_{CP}=8 \text{ S/m}, \theta=\text{orientation of fibers}$
ϵ	Anisotropic	Complex	$\hat{\epsilon} = \epsilon_0 - \frac{j\sigma}{\omega}$ $\epsilon_0=8.85 \times 10^{-12} \text{ F/m}, j=\text{imaginary unit}, \omega=\text{angular frequency of EM wave}$

directions (σ_T), as the graphite fibers are electrically conductive while the polymer matrix is insulating¹⁵⁷. Each individual ply contained fibers in a single direction, and each ply in the laminate had different relative orientation of the fibers, discussed in Chapter 6 and shown in Figure 6.1. The anisotropic electrical conductivity of a single ply was represented by a tensor, and the lay-up was constructed by using rotation matrices to account for the different relative fiber orientations (0° , 90° , $+45^\circ$, or -45°) in each layer of the laminate. The DC value of electrical conductivity was used while the permittivity used was frequency dependent.

The electrical conductivity of CFRPs used in this work has been previously studied and reviewed by Zhao et al.¹⁵⁷ For a ply of unidirectional carbon fibers, the electrical conductivity tensor for fibers at a relative angle, θ , is given by¹⁵⁸

$$\sigma_{\theta \text{ orientation}} = \begin{bmatrix} \sigma_L * \cos^2\theta + \sigma_T * \sin^2\theta & \frac{\sigma_L - \sigma_T}{2} \sin(2\theta) & 0 \\ \frac{\sigma_L - \sigma_T}{2} \sin(2\theta) & \sigma_L * \sin^2\theta + \sigma_T * \cos^2\theta & 0 \\ 0 & 0 & \sigma_{CP} \end{bmatrix} [S/m] \quad (7.20)$$

where σ_{CP} is the conductivity in the cross-ply direction and was assumed to be equal to σ_T , though it can be lower when there are inter-ply resin rich regions⁹². For example, the electrical conductivity for the 0° orientation, with fibers along the x-direction, is given by

$$\sigma_{0^\circ} = \begin{bmatrix} \sigma_L & 0 & 0 \\ 0 & \sigma_T & 0 \\ 0 & 0 & \sigma_T \end{bmatrix} [S/m] \quad (7.21)$$

where σ_{11} (for σ_{ij} in tensor notation) corresponds to the direction parallel to the fibers, and σ_{22} and σ_{33} correspond to the directions perpendicular to the fibers in this frame of reference. In the model, σ_{11} , σ_{22} , and σ_{33} correspond to the x , y , and z directions in Figure 7.1, respectively. Thus, the electrical conductivity tensor for each orientation can be obtained once values for σ_L and σ_T are determined.

The conductivity in the longitudinal direction parallel to the fibers can be determined from the rule of mixtures by considering the graphite fibers as conductive inclusions in parallel. Using this model, the electrical conductivity in the parallel direction is given by^{157–159}

$$\sigma_L = \sigma_F v_F + \sigma_M (1 - v_F) \quad (7.22)$$

where σ_F is the conductivity of the fibers, v_F is the volume fraction of fibers, and σ_M is the conductivity of the matrix. In this case, the polymer is insulating so σ_M is zero. Thus, the expression simplifies to

$$\sigma_L = \sigma_F v_F \quad (7.23)$$

In this work, IM7 fibers with a conductivity of 6.67×10^4 S/m reported by the manufacturer⁶¹ were used in a PEEK polymer matrix composite. The volume fraction of fibers was 0.60. Thus, σ_L was equal to 4×10^4 S/m.

The electrical conductivity in the transverse direction has been shown experimentally to be ~ 3 orders of magnitude below σ_L ^{160–162}. Conduction in the transverse direction has been theoretically studied in the works by Wasselynck et al.^{158,163–165} by explicitly modeling the fibers using a Monte Carlo simulation to account for random positioning of fibers in the matrix (i.e. fibers were not evenly spaced) and “waviness” (deviation from being perfectly straight) of the

carbon fibers. After a virtual sample was generated by the Monte Carlo simulation, an equivalent impedance analysis was used to deduce the conductivity. It was found that conduction in the directions perpendicular to the fibers is the result of two phenomena: (1) the fibers are not perfectly parallel and have a probability of contacting with neighboring fibers which provides conductive paths in the transverse directions, and (2) under an AC field, capacities develop between nearby fibers and mutual inductance can occur. The latter has been demonstrated to become significant at frequencies greater than 1 GHz, leading to a complex-valued conductivity¹⁶⁴. In a work comparing the theoretical model to experimental measurements, Wasselynck et al.¹⁵⁸ found that transverse conductivity was ~ 8 S/m for a volume fraction of 0.60. Thus, $\sigma_T=8$ S/m was used in the calculation of the electrical conductivity tensor in this work, which was also consistent with various experimental studies that determined that the transverse conductivity is typically 3 orders of magnitude lower than the longitudinal direction^{160–162}.

For permittivity the CFRP was assumed to be a lossy conductor, meaning that SE by absorption loss was dominated by Ohmic loss. This assumption is valid when the electrical conductivity of the material is high compared to the polarizability⁵⁸. In general, the complex, frequency dependent permittivity is given by the expression⁵⁹

$$\hat{\varepsilon} = \varepsilon' - j\varepsilon'' = \varepsilon_r \varepsilon_0' - j\varepsilon'' \quad (7. 24)$$

where ε' represents the real part of the permittivity corresponding to capacitance, and ε'' is the imaginary part of the permittivity corresponding to polarization delay loss and Ohmic loss, given by⁵⁹

$$\varepsilon'' = \varepsilon_d + \frac{\sigma}{\omega} \quad (7. 25)$$

where ε_d is the contribution from polarization delay loss and the second term represents the contribution from Ohmic loss. When a material is conductive and can sustain current, ε_d can be

assumed to be negligible. Additionally, when $\sigma \gg \omega\epsilon'$ is valid, ϵ_r can be assumed to be equal to one and $\epsilon' = \epsilon_0$ ⁵⁸⁻⁶⁰. For the case of graphite fibers in PEEK polymer, $\epsilon_r = 1$ due to their high conductivity, while ϵ_r of PEEK is reported to be 3.2 at 1 GHz¹⁶⁶. To estimate the validity of the good conductor approximation, the ratio $\sigma/\omega\epsilon'$ in the longitudinal and transverse directions is plotted for $\epsilon_r = 1$ and $\epsilon_r = 3.2$, shown in Figure 7.3. When the frequency increases beyond 1 GHz, the lossy conductor approximation is still applicable in the longitudinal, high conductivity direction, but is less applicable in the lower conductivity transverse direction. Ideally, the complex permittivity in the frequency range of interest would be experimentally measured, as it is difficult to theoretically predict⁵⁹. Rather, the complex, anisotropic permittivity was assumed to be

$$\hat{\epsilon} = \epsilon_r \epsilon_0 - \frac{j\sigma}{\omega} \quad (7.26)$$

with $\epsilon_r = 1$, assuming that the lossy conductor approximation was valid, and that the absorption loss was dominated by Ohmic loss (σ/ω) more than polarization loss (ϵ_d).

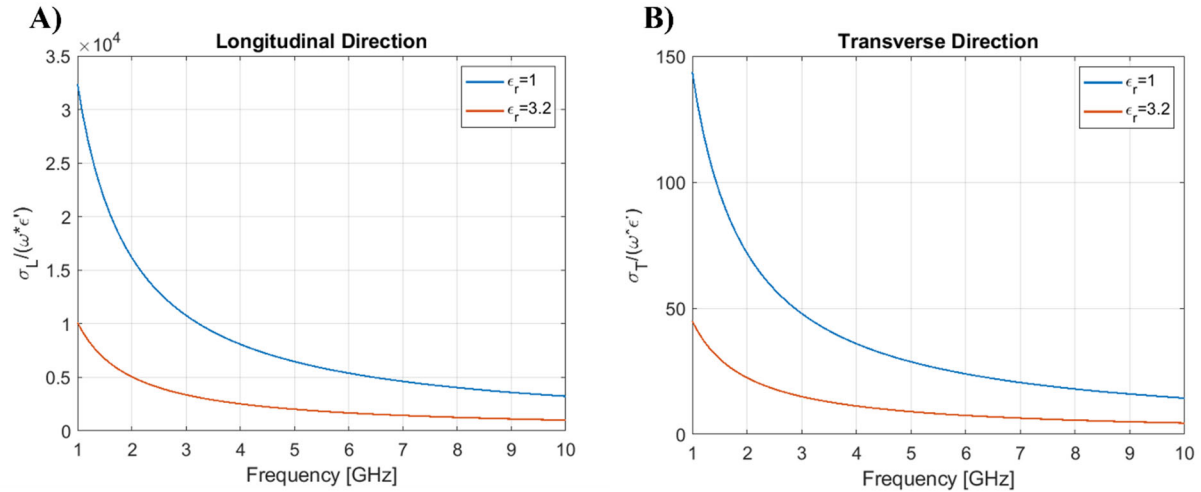


Figure 7.3. Evaluation of the validity of the lossy conductor approximation for permittivity in A) the longitudinal direction parallel to the fibers and B) the transverse direction perpendicular to the fibers.

7.3.3. Effect of Material Property Values on Shielding Effectiveness

To understand the sensitivity of SE calculated from the model to the material properties selected, σ_L , σ_T , and ϵ_r were each varied in the GHz regime. The CFRP lay-up used was $[90^\circ, 0^\circ, +45^\circ, -45^\circ, 0^\circ, 90^\circ]$, without any copper mesh layers. The thickness of each ply was 0.125 mm, consistent with the SEM micrographs shown in Section 6.2. The results are shown in Figure 7.4. It can be seen that the choice of σ_T and ϵ_r have minimal effect on the calculated SE. There is a maximum variation of ~ 3 dB and ~ 10 dB for σ_T (Figure 7.4 B) and ϵ_r (Figure 7.4 C), respectively. However, the selection of σ_L can have a significant impact on the calculated shielding effectiveness (Figure 7.4 A). In the context of the assumptions made to determine material properties for the model, σ_L was the most straight-forward to approximate by the rule of mixtures using values reported by the manufacturer. It can be determined that the assumptions made for σ_T and ϵ_r are reasonable for the purposes of the model because the precision of the approximation is not as critical as the selection of σ_L for the calculation of shielding effectiveness. Additionally, this demonstrates that the high electrical conductivity in the longitudinal direction parallel to the fibers is the dominant mechanism in electromagnetic shielding by Ohmic loss in unidirectional CFRPs.

7.3.4. Effect of Ply Thickness on Shielding Effectiveness

The shielding effectiveness of a laminate without copper mesh was modeled in the GHz regime to determine the SE contribution from the CFRP alone. The lay-up used was $[90^\circ, 0^\circ, +45^\circ, -45^\circ, 0^\circ, 90^\circ]_2$ which is typically used in structural applications due to its quasi-isotropic mechanical properties⁴⁶. Shielding effectiveness for the lay-up with individual ply thickness of 0.125 mm in the range 2-10 GHz is shown in Figure 7.5.A. It can be seen that the contribution to SE from absorption is much larger than the contribution from reflection. The same laminate lay-

up was modeled with an individual ply thickness of $t=0.0625$ mm, shown in Figure 7.5.B. The contribution to SE by reflection was the same as the lay-up with 0.125 mm ply thicknesses; however, the absorption loss was lower due to the reduced thickness of each ply and, subsequently, the overall laminate thickness. This can be understood by considering that the reflection component due to impedance difference is concerned with the number of interfaces between different media, while the absorption loss is proportional to the thickness of the material, discussed in Section 1.7. Because the shielding effectiveness of the CFRP was

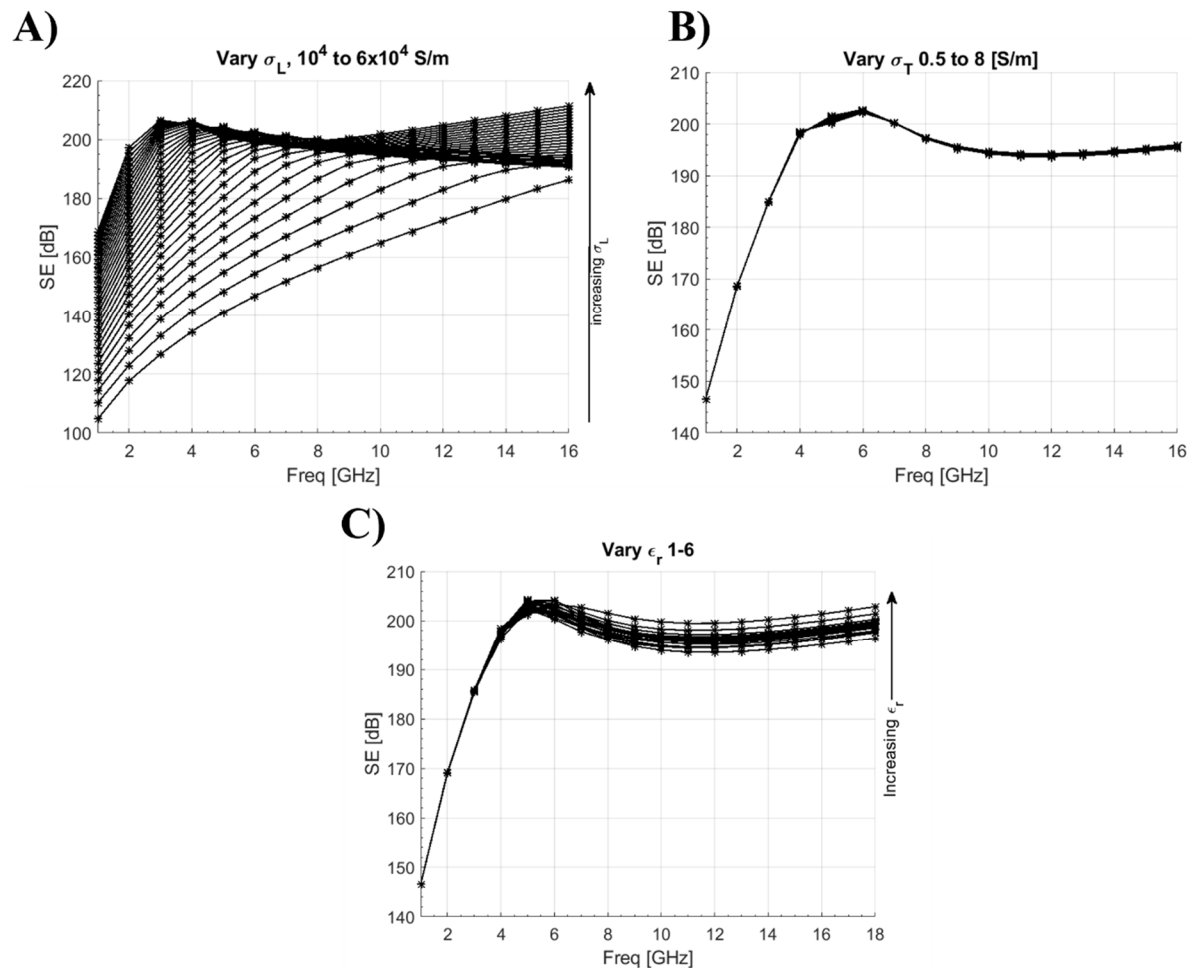


Figure 7.4. The effect of varying A) longitudinal electrical conductivity, B) transverse conductivity and C) real part of the imaginary permittivity on the SE in the range 1-16 GHz for a lay-up of $[90^\circ, 0^\circ, +45^\circ, -45^\circ, 0^\circ, 90^\circ]$.

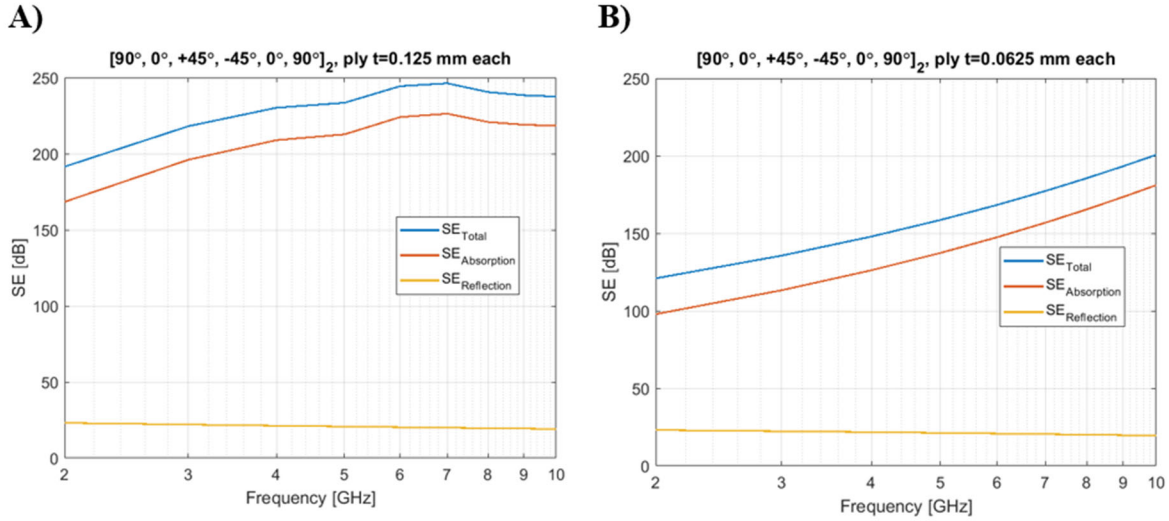


Figure 7.5. The effect of ply thickness on SE in the range 2-10 GHz for the lay-up $[90^\circ, 0^\circ, +45^\circ, -45^\circ, 0^\circ, 90^\circ]_2$. In A) the ply thickness is 0.125 mm, and in B) the ply thickness is 0.0625 mm.

dominated by absorption loss, further improvement in SE could be achieved by increasing the thickness of each ply in the laminate.

7.3.5. Effect of Fiber Orientation on Shielding Effectiveness

The dominant effect of absorption loss in the CFRP can be understood by considering the Ohmic loss in the material. To investigate this further, the E field magnitude and current density magnitude in the model were plotted in Figure 7.6.A and 7.6.B, respectively for the 2 GHz test. The E field decreased as the wave traveled through the thickness of the laminate in the +z direction. From the plot of current density, the current was higher in the first few layers of the CFRP laminate and decreased as the EM wave traveled through all the layers. The EM power loss density and current density components (J_x , J_y , and J_z) are plotted in Figure 7.7.A and 7.7.B, respectively, for the 2 GHz test. The plot of EM power loss density shows that most of the electromagnetic power is dissipated in the first two layers of the CFRP laminate, with fibers oriented along y for the 90° ply and along x for the 0° ply. The plot of current density shows that a current is induced along the high conductivity fiber direction, which is the mechanism by

which EM energy is dissipated. As the current flows, the resistance of the material dissipates the energy as heat. By the time the EM wave reaches the +45° and -45° ply, the induced current is much lower, and the EM power loss is similarly low. Thus, absorption due to Ohmic loss in the high conductivity direction parallel to the fibers is the dominant mechanism by which CFRPs shield EM radiation.

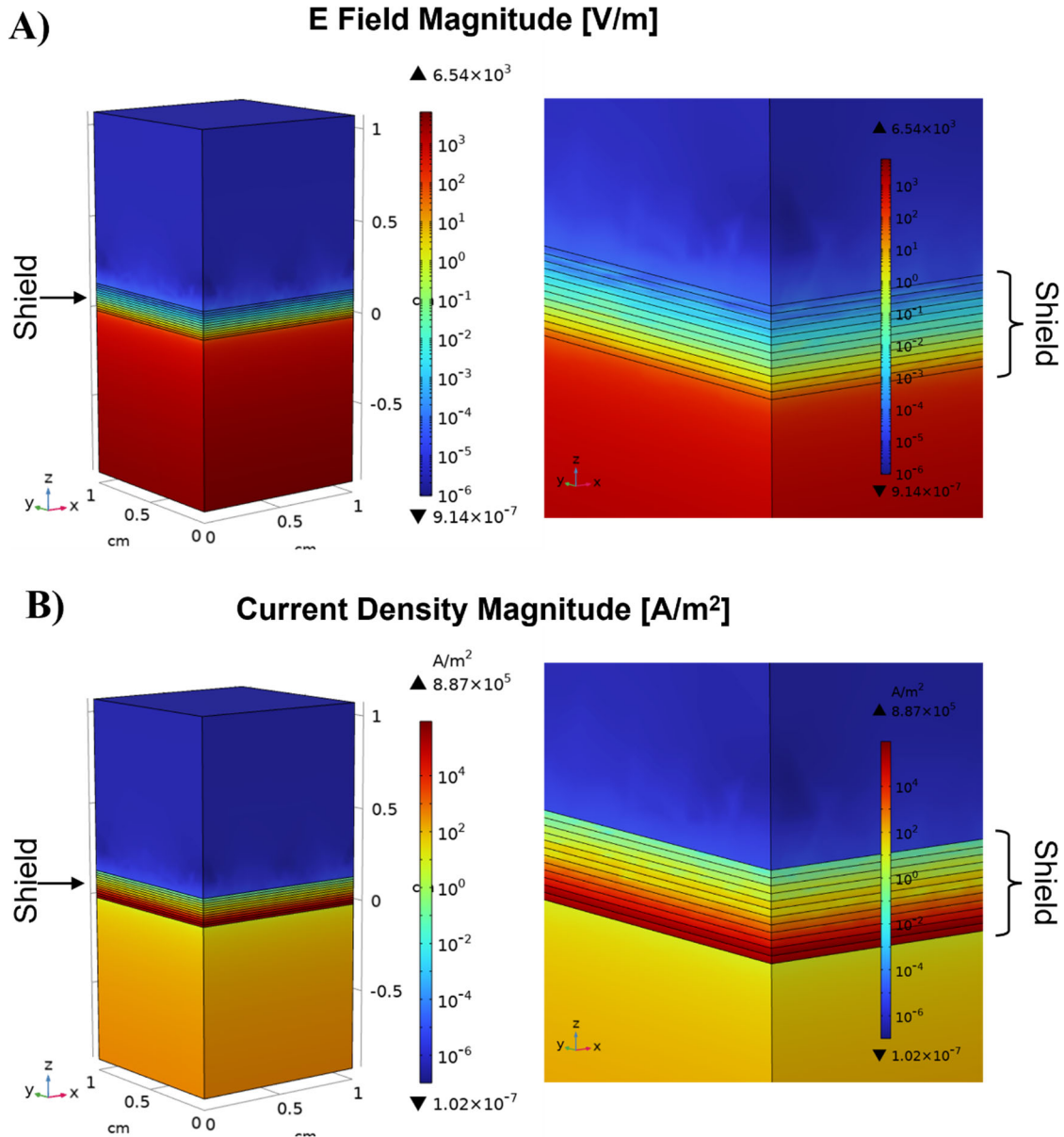


Figure 7.6.A) Electric field magnitude and B) current density magnitude distribution through the model for the lay-up $[90^\circ, 0^\circ, +45^\circ, -45^\circ, 0^\circ, 90^\circ]_2$ at 2 GHz. The thickness of each ply was 0.125 mm.

To further investigate the role of the high conductivity direction parallel to the fibers on the shielding effectiveness mechanism of the CFRP without copper mesh, the $[90^\circ, 0^\circ, +45^\circ, -45^\circ, 0^\circ, 90^\circ]_2$ lay-up was compared to a lay-up of $[90^\circ, 0^\circ, +45^\circ, -45^\circ]$, both with individual ply thickness of 0.125 mm. The first lay-up consisted of 12 plies, while the second consisted of 4 plies, thus the total laminate thicknesses were 1.5 mm and 0.5 mm, respectively. The second lay-up was chosen to compare the SE for a reduced number of plies/laminate thickness while still including each of the four orientations. The different lay-ups were tested in the frequency range 50 MHz-10 GHz. The SE calculated for each laminate are shown in Figure 7.8. The reflection component of SE was the same for the 12 ply lay-up and the 4 ply lay-up, indicating that multiple layers with the same fiber orientation did not provide an additional contribution to shielding effectiveness by reflection in the 12 ply laminate. As expected, the absorption component of SE was reduced considerably by reducing the

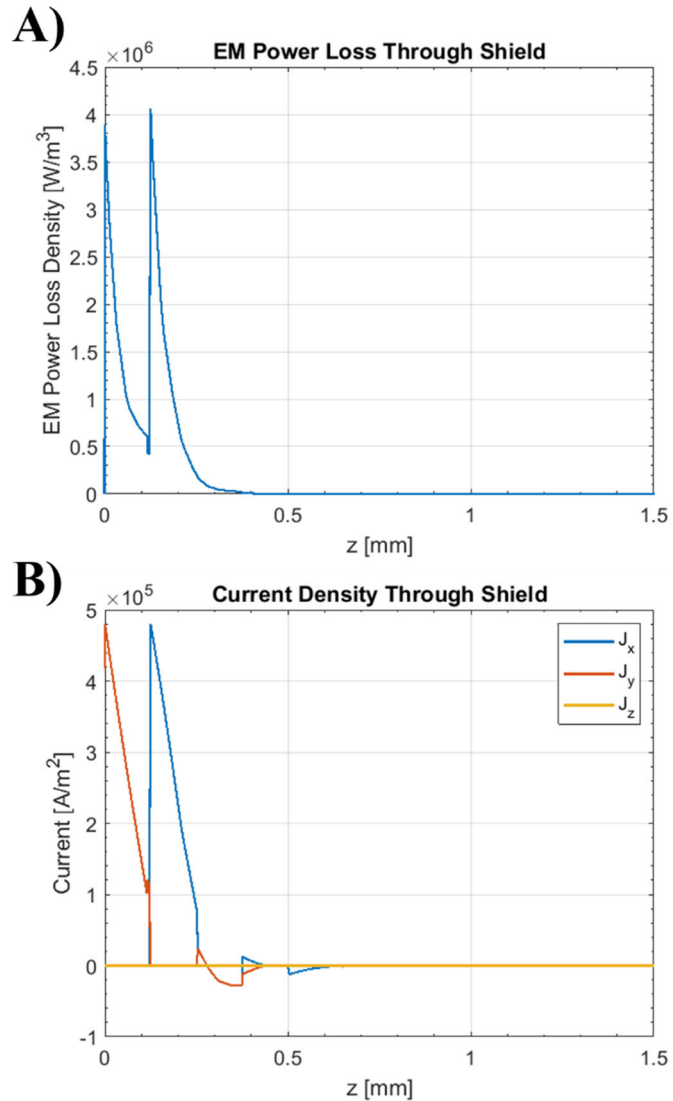


Figure 7.7.A) EM power loss and B) current density as a function of z through the center of the shield at 2 GHz for the model shown in Figure 7.6 with a lay-up of $[90^\circ, 0^\circ, +45^\circ, -45^\circ, 0^\circ, 90^\circ]_2$.

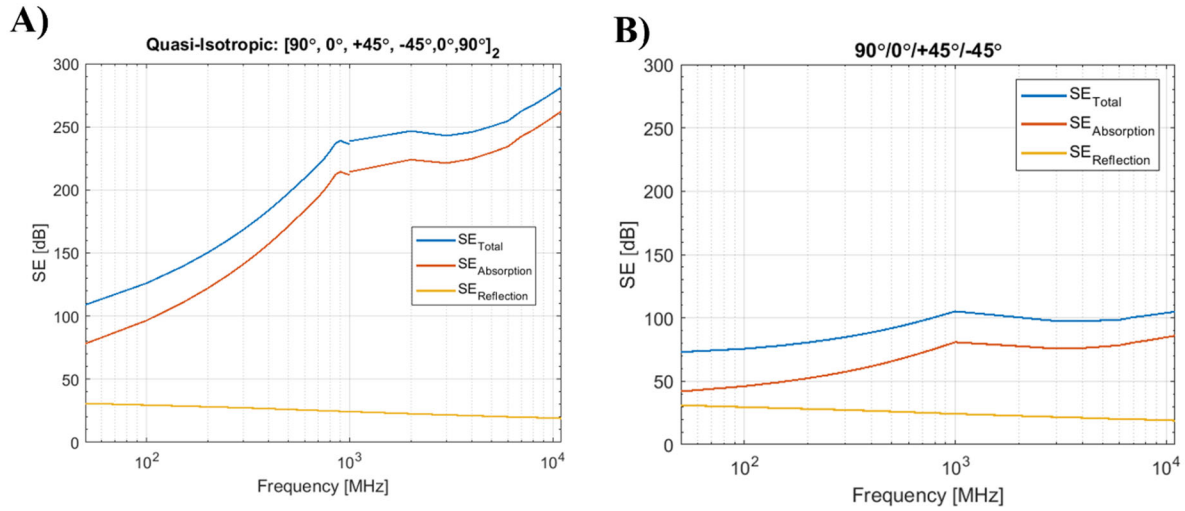


Figure 7.8. SE in the range 50 MHz to 10 GHz for A) the lay-up $[90^\circ, 0^\circ, +45^\circ, -45^\circ, 0^\circ, 90^\circ]_2$ and B) the lay-up $[90^\circ, 0^\circ, +45^\circ, -45^\circ]$ with reduced number of plies/overall laminate thickness.

thickness of the laminate by 1/3. This result further indicated that increasing the thickness of the CFRP laminate increases the shielding effectiveness considerably because the dominant mechanism is absorption loss.

7.3.6. Effect of Fiber Orientation on Shielding Effectiveness

Two laminates, each with four plies (0.5 mm total thickness) but different fiber orientations were tested to determine the importance of multiple fiber orientations on SE. The $[90^\circ, 0^\circ, +45^\circ, -45^\circ]$ laminate was compared to a $[90^\circ, 90^\circ, 90^\circ, 90^\circ]$ laminate in the range 50 MHz to 10 GHz. The results are shown in Figure 7.9. The model indicated that both the reflection loss and absorption loss decreased for the $[90^\circ, 90^\circ, 90^\circ, 90^\circ]$ laminate with fibers oriented in only one direction. In this configuration, the fibers are all oriented along the y-direction, thus the electrical conductivity was high ($\sigma_L=4 \times 10^4$ S/m) in the y-direction, but three orders of magnitude lower in the x-direction and z-direction ($\sigma_T=8$ S/m). As a consequence, the incident EM field which had components in both the x-direction and y-direction was only able to

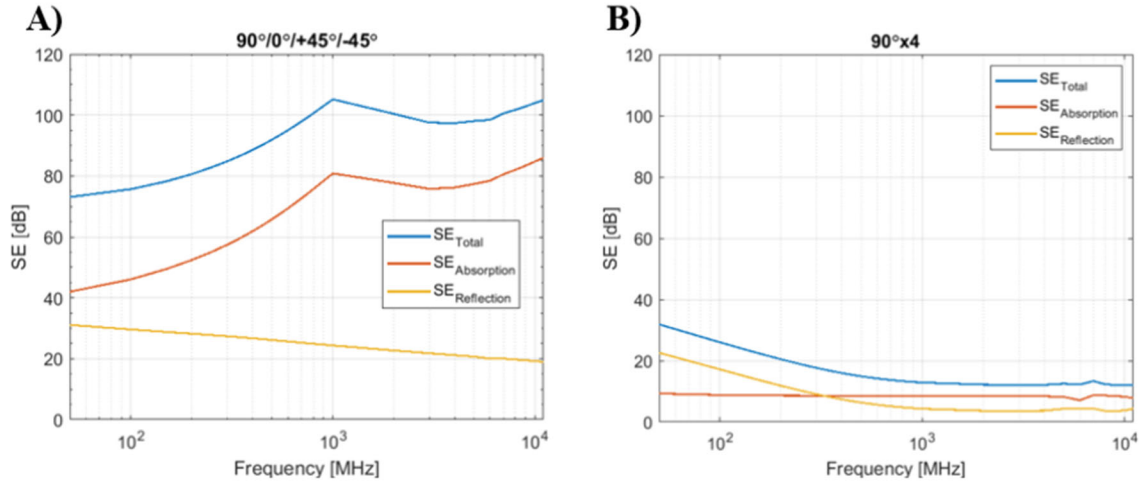


Figure 7.9. SE in the range 50 MHz to 10 GHz for A) the lay-up $[90^\circ, 0^\circ, +45^\circ, -45^\circ]$ and B) the lay-up $[90^\circ, 90^\circ, 90^\circ, 90^\circ]$ with the same thickness but with fibers oriented in only one direction, the y -direction.

be dissipated in the y -direction, causing lower SE. The results indicate that multiple fiber orientations that increase isotropy of electrical conductivity in the overall CFRP laminate are desired to improve SE. In this manner, the individual CFRP plies with fibers parallel to each other act like a grating that effectively shields the EM wave in one direction. Thus, designing a laminate with multiple relative orientations of fibers is desirable to enhance overall shielding effectiveness.

7.4. Shielding Effectiveness of Cu Mesh

7.4.1. Analytical Sheet Impedance Expression

The shielding effectiveness of the copper mesh can be calculated by using an analytical expression for the equivalent sheet impedance of a wire mesh screen developed by Casey et al.¹⁶⁷ The large difference in length scale between the EM wavelength and the mesh dimensions made explicitly modeling the geometry of the copper mesh very memory intensive. Once the sheet impedance of the copper mesh was calculated, it was incorporated into the COMSOL model as a boundary layer with the calculated impedance at a given frequency using the “Lumped Element”

boundary condition, which relates the tangential E field component to the surface current density induced on the boundary surface. By homogenizing the copper mesh into a single boundary condition in the model, the memory requirements of the problem were greatly reduced.

The sheet impedance expression developed by Casey et al.¹⁶⁷ considers the copper mesh as a set of two perpendicular wire screens, shown in Figure 7.10. The copper mesh characteristics needed for the calculation are r_w , the radius of the wire, a_s , the separation between wires, and σ , the conductivity of copper. For the copper mesh used in the multifunctional composite samples, r_w was 0.05 mm, and a_s was approximated as 474 μm . The conductivity of copper is 5.87×10^7 S/m. The equation for Z_s , equivalent sheet impedance, is given by¹⁶⁷

$$Z_s = Z'_w a_s + j\omega L_s \quad (7.27)$$

Where Z'_w is the internal impedance per unit length wire, and L_s is the sheet inductance parameter. Z'_w is given by¹⁶⁷

$$Z'_w = R'_w \frac{\sqrt{j\omega\tau_w} I_0(\sqrt{j\omega\tau_w})}{2I_1(\sqrt{j\omega\tau_w})} \quad (7.28)$$

where R'_w is the DC resistance per unit length of wire, τ_w is the diffusion time constant, and $I_0()$ and $I_1()$ are the modified Bessel function of the first kind as function of $\sqrt{j\omega\tau_w}$, order 0 and 1, respectively. R'_w is given by¹⁶⁷

$$R'_w = (\pi r_w^2 \sigma_w)^{-1} \quad (7.29)$$

and τ_w is given by

$$\tau_w = \mu_0 \mu_r \sigma_w r_w^2 \quad (7.30)$$

where μ_r is the relative magnetic permeability, 1 for copper which is non-magnetic. The remaining parameter necessary for the calculation of Z'_w is L_s , the sheet inductance parameter, given by¹⁶⁷

$$L_s = -\frac{\mu_0 a_s}{2\pi} \ln\left(1 - e^{-\frac{2\pi r_w}{a_s}}\right) \quad (7.31)$$

A MATLAB script was written to calculate Z_s as a function of frequency and linked to COMSOL so that it could be incorporated into the model using the Lumped Element boundary condition that specifies impedance. The shielding effectiveness was then calculated following the same analysis described in Section 7.2. The SE result for one mesh layer is compared to the SE reported by the manufacturer of the Cu mesh using the experimental ASTM D4935-10 method in Figure 7.11. The SE values calculated using equivalent sheet impedance match the experimentally measured values, demonstrating the validity of this approach. First, the equivalent sheet impedance expression was used to compare the shielding effectiveness of a single mesh layer using different metals. Then, SE for different geometries of the copper mesh

was considered for a single mesh layer. The material properties and geometries used in the calculations are summarized in Table 7.2.

Finally, the copper mesh was incorporated into the CFRP model to investigate the effect of copper mesh placement with respect to the CFRP plies on SE.

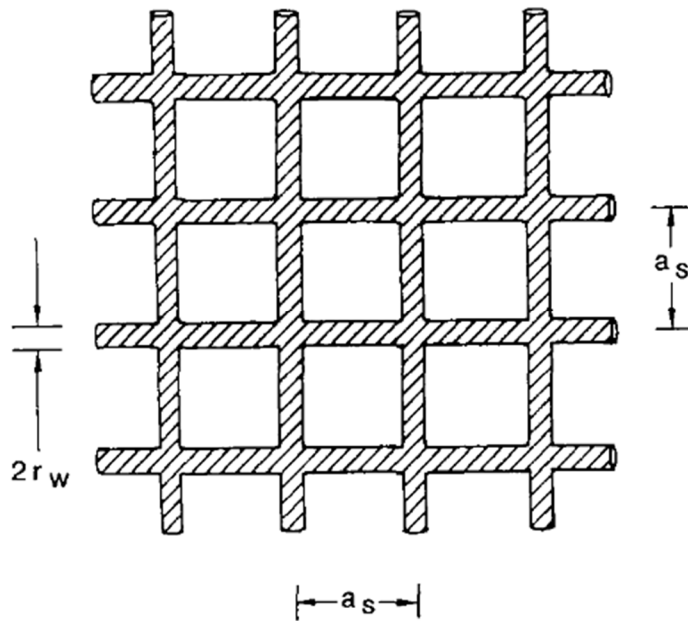


Figure 7.10. Geometry of the wire mesh. The individual meshes are square and the wire junctions are assumed to be bonded. Reproduced from Casey, K. F. (1988). *Electromagnetic Shielding Behavior of Wire-Mesh Screens*. *IEEE Transactions on Electromagnetic Compatibility*, 30(3), 298–306. <https://doi.org/10.1109/15.3309>.

7.4.2. Comparison of Different Metals

The equivalent sheet impedance was used to compare shielding effectiveness of different metals in the frequency range 10 kHz-10 GHz. In each case, a single mesh layer was modeled with the same geometry, but σ_w , the conductivity of the wire, was changed to correspond to the conductivity of each different metal, summarized in Table 7.2. The results are shown in Figure 7.12 A. For each metal, the shielding effectiveness was constant in the lower frequency range

and began to decrease around ~ 1 MHz for the higher conductivity metals (Ag, Cu, Al) and around ~ 100 MHz for the lower conductivity metals (Stainless steel-301 and Inconel-625). The decrease in SE at higher frequencies has been attributed to the mutual inductance of the open mesh geometry, which increases with increasing frequency¹⁶⁷⁻¹⁶⁹. The SE ability of each metal was correlated to the metal conductivity, with the highest conductivity metal (Ag) performing the best, and the lowest conductivity metal (Inconel-625) performing the worst. However, the benefit of using a higher conductivity metal was

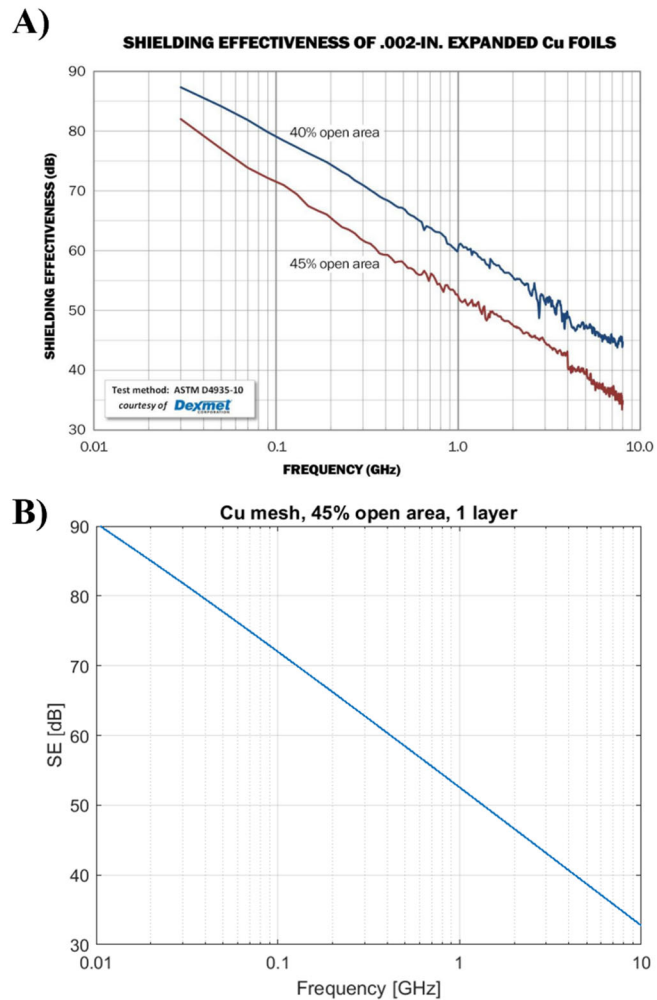


Figure 7.11. Comparison of A) SE experimentally measured by the manufacturer of the Cu mesh used in the multifunctional composite, DexMet and B) the SE of the Cu mesh calculated using the equivalent sheet impedance, indicating that the results are equivalent.

Table 7.2. Summary of the material properties and mesh geometries used in the calculation of equivalent sheet impedance for the metal wire meshes.

Material	Electrical conductivity [S/m]	μ_r	r_w [μm]	a_s [μm]
Cu	5.87×10^7	1	50	474, 250, and 125
Ag	6.3×10^7	1	50	474
Al	3.54×10^7	1	50	474
Al alloy-6061	2.7×10^7	1	50	474
Stainless steel-301	1.4×10^6	1	50	474
Inconel-625	7.7×10^5	1	50	474

decreased at higher frequency where the effects of mutual inductance reduce the shielding effectiveness.

Multifunctional composites are typically used in situations where it is desirable to minimize weight of the final structure by combining multiple functions into a single component, a design criterion that is especially important for aerospace applications⁴⁵. To consider the SE of each metal along with their weight, the SE was normalized to density, shown in Figure 7.12 B. When considering density, pure Al and AA-6061 outperformed all of the other metals tested in this frequency range due to its balance of low density and high electrical conductivity. Thus, if minimization of weight is desirable for a given application, a wire mesh of aluminum or one of its alloys would provide comparable SE to copper, but at a reduced weight.

7.4.3. Comparison of Different Mesh Dimensions

The effect of using different mesh dimensions for a single layer of copper mesh was also compared to determine the effect on SE. For comparison, the SE of a solid Cu plate with

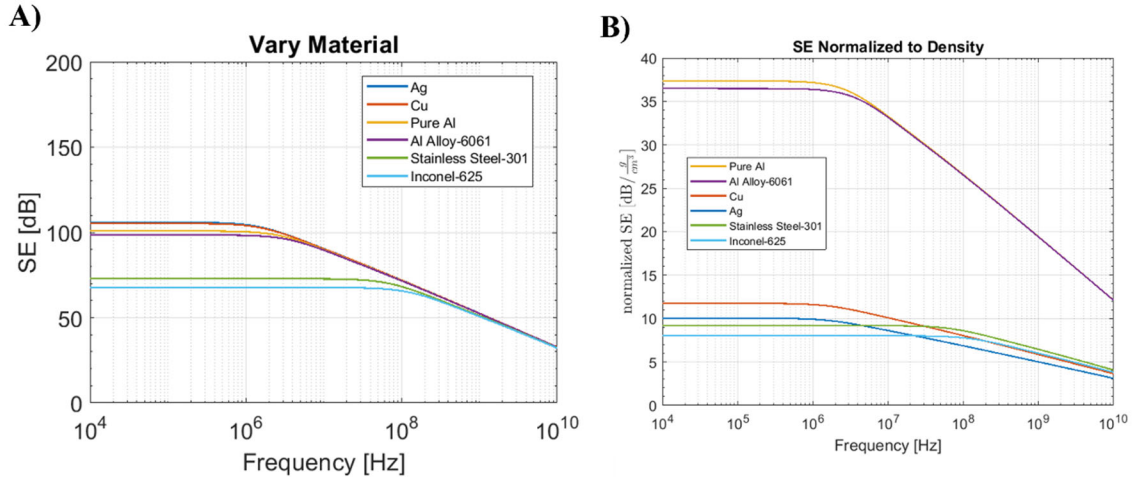


Figure 7.12.A) SE calculation using the equivalent sheet impedance approximation for different metals with different electrical conductivities and B) SE calculated for each metal normalized to density of the metal.

thickness equal to r_w , the radius of the wire (0.5 mm) was included. The SE of the solid Cu plate was calculated using the Simon Formalism, given by⁵⁶

$$SE = 50 + \log_{10}(\rho f)^{-1} + 1.7t\left(\frac{f}{\rho}\right)^{1/2} \quad (7.32)$$

where f is the frequency in MHz, t is the thickness of the shield in cm, and ρ is the resistivity in $\Omega \cdot \text{cm}$. The Simon formalism is generated by assuming a homogenous, isotropic slab of a good conductor, that is non-magnetic ($\mu_r=1$) with impedance, $\eta_s = \sqrt{\frac{j\omega\mu_0}{\sigma}}$. The first two terms give the reflection contribution, R in Equation 7.1, and the third term gives the absorption contribution, A in Equation 7.1. The equations for R and A are given in Equations 1.4 and 1.3, respectively, using the skin depth defined in Equation 1.2. The effect of internal reflections, B in Equation 7.1, is assumed to be negligible.

The shielding effectiveness for different copper mesh geometries are shown in Figure 7.13. For a finer mesh (smaller a_s , wire separation) the shielding effectiveness increases, with the highest SE given by the solid plate. The SE of the solid Cu plate is much higher than that of the mesh at higher frequencies because the absorption component is higher, and SE by absorption

increases with increasing frequency. Additionally, for finer mesh dimension the decay in SE as frequency increases beyond ~ 1 MHz due to mutual inductance appears to be smaller.

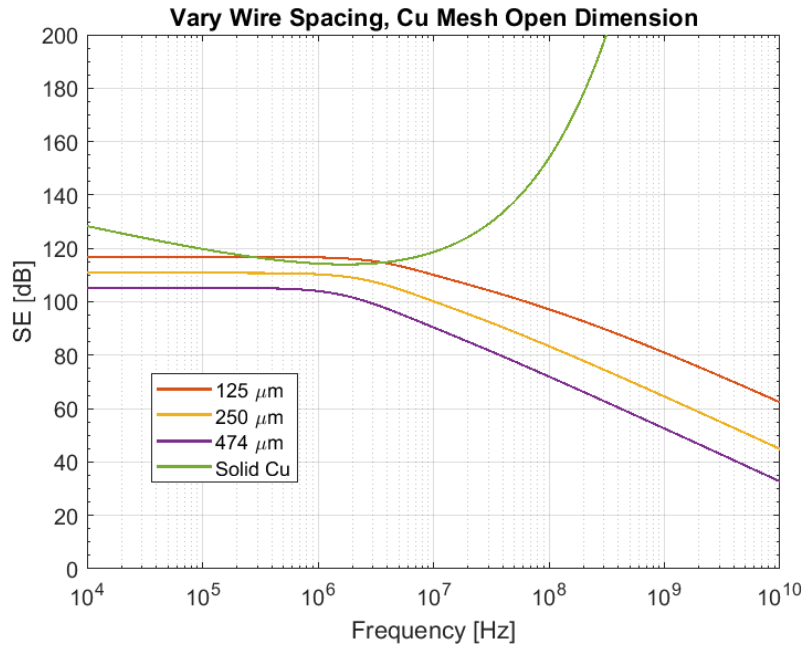


Figure 7.13. SE calculated using the equivalent sheet impedance approximation for the Cu mesh with different open mesh dimension, a_s .

Considering that the results shown in Figure 7.12.A indicated that the

difference in SE for different materials beyond 1 MHz is minimal, the SE of a metal wire mesh can be considered to consist of two regimes: (1) in the range $< \sim 1$ MHz the material properties dominate and higher SE is best achieved by selecting a higher conductivity metal, and (2) in the range $> \sim 1$ MHz the effects of geometry dominate and higher SE is best achieved by using a finer mesh. This observation is consistent with the design of electromagnetic shields discussed by Ott⁵⁵, where the lower frequency ranges are described to be material dependent, and the higher frequency range (on the order of GHz) are described as geometry dependent with a pronounced effect from apertures in the shielding material. Thus, the metal and mesh geometry used should be selected based on the desired frequency to be shielded in application.

7.5. Shielding Effectiveness of Multifunctional Composite with CFRP and Cu Mesh Layers

The effect of Cu mesh layer placement in the CFRP lay-up on the SE of the multifunctional composite laminate was tested by calculating SE for different configurations.

The base CFRP laminate was two layers with a $[90^\circ, 0^\circ]$ configuration. The baseline SE for just the CFRP laminate, and the Cu mesh layer without CFRP were tested, shown in Figure 7.14.A and 7.14.B, respectively. Three different placements of Cu mesh layer were tested: $[\text{Cu}, 90^\circ, 0^\circ]$, $[90^\circ, \text{Cu}, 0^\circ]$, and $[90^\circ, 0^\circ, \text{Cu}]$ shown in Figure 7.14.C, 7.14.D, and 7.14.E, respectively. SE was calculated in the range 50 MHz to 10 GHz. The shielding effectiveness for the baseline without Cu mesh, shown in Figure 7.14.A had lower SE than the three configurations containing a Cu mesh layer, as expected; however, there was only a small increase in SE by adding one Cu mesh layer, approximately 5-10 dB dependent on frequency. Interestingly, because the reflection contribution to SE decreases as frequency increases (discussed in Section 1.7), the SE of the Cu mesh alone (Figure 7.14.B) was lower than the SE of the CFRP without Cu mesh above ~ 500 MHz. This is due to the increased thickness of the CFRP laminate compared to the Cu mesh (0.25 mm compared to 0.05 mm) which increased the contribution from absorption, which increases with frequency. Because the Cu mesh is dominated by the reflection component of SE, it provides more benefit at lower frequencies $< \sim 500$ MHz.

For the three configurations containing Cu mesh shown in Figure 7.14. C, 7.14.D, and 7.14.E the total SE was approximately the same for each, while the relative contributions from reflection and absorption varied slightly depending on the placement of the Cu mesh layer. The reflection component was larger when the Cu mesh was the first layer upon which the EM wave was incident, shown in Figure 7.14.C; however, the effect was minimal (~ 5 dB) compared to the configurations where the EM wave first impinged upon CFRP layers in Figure 7.14.D and 7.14.E. Accordingly, the absorption component was lower by ~ 3 -5 dB when the Cu mesh layer was the first layer. This can be understood by considering that less of the EM wave travels

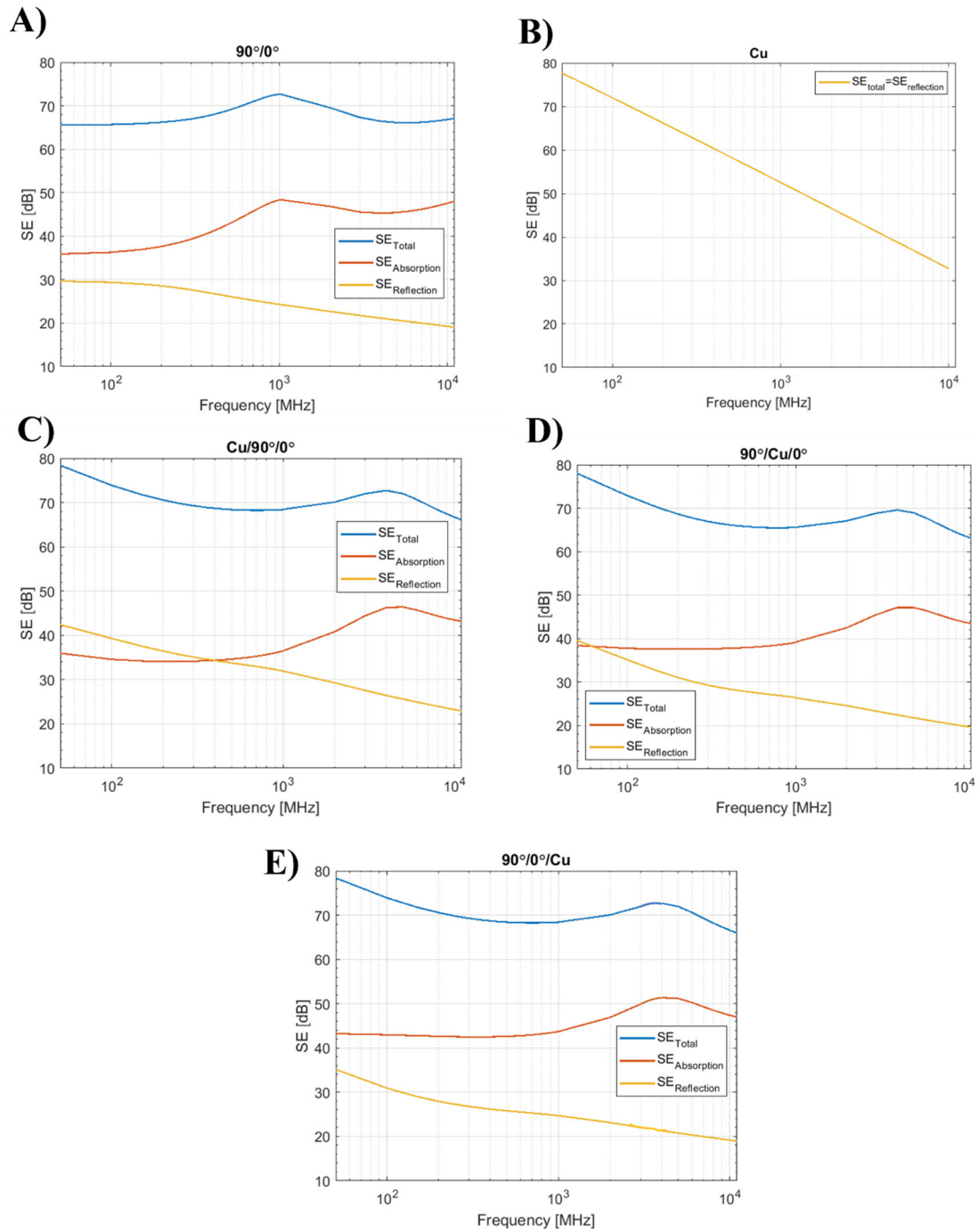


Figure 7.14. Calculated SE in the range 50 MHz-10 GHz for A) the baseline CFRP with the lay-up [90°, 0°], B) the baseline Cu mesh with $a_s=474$, C) the lay-up [Cu, 90°, 0°], D) the lay-up [90°, Cu, 0°], and E) the lay-up [90°, 0°, Cu].

through the CFRP layers, which are dominated by absorption, since a larger portion of the EM wave is reflected at the first interface that contains the Cu mesh.

These results demonstrate that the incorporation of a Cu mesh into the CFRP laminate could improve SE by adding a reflection-dominant component with high electrical conductivity that has higher SE at lower frequencies. Because SE by reflection decreases with increasing frequency, the benefit of adding a Cu mesh layer is minimal at higher frequencies $> \sim 500$ MHz. The SE by absorption increases with increasing frequency, so the overall SE of the multifunctional composite is improved over a wider frequency range by incorporating both a reflection-dominant component (the Cu mesh) and an absorption-dominant component (the CFRP). At lower frequencies, the reflection-dominant Cu mesh provides greater benefit than the absorption-dominant CFRP, while the opposite is true at higher frequencies. The results for different layer placement in the lay-up indicate that the placement of the Cu layer has minimal effect on the overall SE in the frequency range examined.

7.6. Limitations of the SE Model, Overestimation of CFRP SE

When comparing the modeled SE to the experimental measurements of SE reported by the manufacturer for the $[90^\circ, 0^\circ, +45^\circ, -45^\circ, 0^\circ, 90^\circ]_2$, the model overestimated the SE by a factor of 1.5-3x in the frequencies above ~ 1 GHz. The manufacturer reported SE of ~ 90 -100 dB in this range, while the model calculated an SE of ~ 150 -250 dB in this range. The disparity is most likely a result of an overestimation of the absorption component of SE as a consequence of the assumptions made when homogenizing the electrical properties of the CFRP.

One key limitation of the model is that the DC values of electrical conductivity are used when formulating the conductivity tensor. Kim & See¹⁷⁰ observed from a model of permittivity and conductivity that the AC longitudinal conductivity of unidirectional carbon-epoxy composites drops rapidly beyond 100 MHz due to an increased effective resistance of the material by the skin effect (discussed in Section 1.7), and can be an order of magnitude lower in

the range above 1 GHz. As the frequency increases, the skin depth decreases, and a smaller thickness of the material is capable of conducting electricity, leading to an increased resistance. As discussed in Section 7.3.3, the selection of σ_L has a pronounced effect on the calculated SE, which most likely contributed to the overestimation of SE by using the DC conductivity value in the range where the actual AC conductivity might be much lower. The transverse conductivity has been shown to increase with increasing frequency^{163,170–172}; however, the results of Section 7.3.3 indicate that the overestimation of σ_L would have a more pronounced effect on the SE calculation than the underestimation of σ_T . In order to account for the skin effect in the model, the resolution of the finite element mesh used must be a fraction of the skin depth, which in this case resulted in higher memory requirements than the computer used was capable of. Thus, the overestimation of σ_L by using the DC value is most likely what resulted in an overestimation of SE in the model.

Further, the use of AC conductivity values could improve accuracy of the model as frequency increases to properly account for the skin effect. To account for the skin effect in the model using DC conductivity, it is necessary to use a finite element size that is sufficiently small to capture the inductive effects that give rise to the skin effect by setting the minimum element size to a fraction of a skin depth. Doing so greatly increases the memory requirements of the model and is not typically practical, so the use of AC conductivity values is preferred. In Figure 7.15.A, a plot of current density through the shield in the z-direction is given. It can be seen that the skin effect is not accurately reflected by the induced current in each layer. The skin depth at 11 GHz is 20 μm ; however, there is current flow through the entire ply thickness (125 μm). The direction of the current density alternates within a single ply, however the element mesh size is too large to accurately capture the skin effect where the alternating direction of the induced

current density should result in a confinement of current flow to the surface of the material. As a result, current flows through the entire thickness of the ply. Potentially this inability of the model to capture the skin effect is the reason why the modeled SE reaches a maximum in the 1-2 GHz range, where the skin depth is on the order of the thickness of the ply, shown in Figure 7.15.B., and then has minimal further increase with increasing frequency. As the skin depth becomes smaller than the mesh element size, the model is not able to capture the increase in SE by absorption due to the skin effect.

Additionally, the homogenization assumptions used to determine a permittivity value could have contributed to the overestimation in SE for the CFRP. Holloway et al.⁹⁴ evaluated the effect of different permittivity homogenization methods on the calculated SE and found that representing the CFRP ply as a single layer with homogeneous, anisotropic permittivity resulted in an overestimation of SE for frequencies higher than 2 GHz. As discussed in Section 7.3.3, the choice for real part of the permittivity has minimal effect on the calculated SE; however, the assumption that the imaginary component consists only of a contribution from Ohmic loss could



Figure 7.15.A) Current density x, y, and z components through the shield in the z-direction at 11 GHz. The layer thickness is 0.125 mm. Current flow changes direction within a single ply, however the skin effect, where the induced current should be confined to the surface of the ply, is not accurately reflected by the model. B) Plot of skin depth vs. frequency indicating that at 11 GHz the skin depth should be smaller than the ply thickness.

be an over-simplification. Potentially polarization effects at a molecular level or interfacial polarization effects at the fiber-polymer interface could affect the SE, which is not accounted for in the model.

7.7. Conclusions and Future Work

The shielding effectiveness of a multifunctional composite containing unidirectional CFRP layers and Cu mesh layers was evaluated using a finite element model in the range 50 MHz to 10 GHz. The electrical properties of the CFRP composite were homogenized by representing each ply containing fibers in a single direction as a homogeneous, anisotropic material and layering multiple plies with different relative fiber orientations. It was found that the high longitudinal conductivity of the CFRP plies in the direction parallel to the fibers had the most pronounced effect on the SE of the CFRP without Cu mesh. The individual CFRP plies acted like a grating that were effective at attenuating the EM field in the direction parallel to the fibers, primarily through absorption by Ohmic loss. The SE of the CFRP without Cu mesh increased by incorporating multiple plies with different fiber orientations and by increasing the total thickness of the material.

The Cu mesh was represented using an equivalent sheet impedance analytical expression. The effect of using different metals as the mesh material and different mesh geometries was evaluated. It was found that higher conductivity metals result in a higher SE of the mesh, and when normalized to density aluminum provides the best balance of high electrical conductivity and low density out of the metals evaluated. The result of different mesh geometries for the Cu mesh indicates that below ~ 1 MHz the choice of metal material has a more pronounced effect on SE than the choice of dimension, whereas the opposite is true above ~ 1 MHz.

From the model of CFRP with a Cu mesh layer added, it was found that the SE was improved over a wider frequency range by incorporating a reflection-dominant component (the Cu mesh) and an absorption-dominant component (the CFRP). The SE by reflection from the Cu mesh played more of a role at frequencies below ~500 MHz, while the SE by absorption from the CFRP layers contributed more to the total SE at frequencies above ~500 MHz. The total SE of the CFRP laminate with Cu mesh was higher than that of the CFRP or Cu mesh alone, while the placement of the Cu mesh in the laminate lay-up resulted in minimal difference in SE. In future work, the model could be improved by considering the effect of AC conductivity on the calculated SE. In this work, the DC values for the CFRP were assumed which resulted in an overestimation of the absorption component of SE. Additionally, measurement of the complex permittivity in the frequency range of interest for the CFRP could help improve the model by accounting for polarization effects at the molecular level and/or at the fiber-polymer interface.

Chapter 8: Summary of Conclusions and Future Work

8.1. Chapter 3: Critical Current Density Investigation

In Chapter 3, the critical current density of the covetics process was investigated. An AA-1350 3 wt% C covetic sample was made to test the effect of local current density on the graphitic carbon structure and electrical conductivity from that area. Two areas were measured: (1) a region near the Cu-C electrode at $r=0$ cm that experienced a current density of ~ 25 A/cm² and a region at $r=1$ cm that experienced a lower current density of ~ 5 A/cm². It was found that in the high current density region near the electrode, some Raman maps showed increased graphitic carbon crystallite size of 20-30 nm; however, most areas in the high current density region showed a crystallite size of 7-10 nm, comparable to the graphitic carbon crystallite size of the activated carbon starting material. The Raman maps from the sample in the lower current density region did not show any graphitic carbon. The electrical conductivity in both the sample from the high current density region and the low current density region showed a decrease in electrical conductivity relative to the baseline sample with no carbon added. This indicated that the current density used in this experiment was insufficient to induce appreciable crystallization of the graphitic carbon and, thus, the electrical conductivity was not improved.

Future work could consist of conducting more trials at different currents and different applied times. The applied current density used in this experiment was 250 A, which was the maximum that the covetics processing system was capable of delivering. A greater increase in graphitic carbon crystallite size could potentially be achieved if a higher current density was delivered to the system. Additionally, the same analysis could be performed on a sample made with the pointed graphite electrode, which is capable of producing a higher, but more localized,

current density than the Cu-C electrode used in this experiment for the same applied current. Additionally, the maximum duration of the experiment was limited by overheating of the induction furnace. If a more advanced cooling system were added to the covetics processing system, the effect of longer current application (> 16.67 minutes) could be tested.

In Section 3.7.1, AA-1350 metallurgy was discussed as it relates to the covetics process. The effect of solute segregation was discussed where the carbon phase, which has low solubility in aluminum, could potentially be segregated towards the interior of the sample which solidifies last in the air-cooled cylindrical crucible or segregated to the grain boundaries. This example highlights the potential role of the thermodynamics and kinetics of AA-1350 solidification in the microstructure and properties of the final covetic sample. Future work could investigate the effect of crucible geometry, cooling rate, and post-processing heat treatments on the microstructure and properties of covetic samples.

8.2. Chapter 4: Micromechanics of AA-1350 3 wt% C Covetics

In Chapter 4, nanoindentation was performed in different regions of the covetic samples to understand the role of graphitic carbon as a reinforcement phase in AA-1350 3 wt% C covetics. Structural characterization by Raman, SEM, and TEM was performed and the micro-mechanical properties from regions that contained increased graphitic carbon crystallite size were investigated using nanoindentation. It was found that the graphitic carbon in covetics formed large clusters, and that there was significant porosity in the samples. The graphite clusters had lower reduced elastic modulus and hardness than the aluminum matrix and, thus, did not act as an effective reinforcement phase. K-means clustering of the nanoindentation data was performed to remove data points that were a result of indentation near voids; however, there was still not a reinforcement effect observed from the graphitic carbon structures. Future work to

improve the mechanical properties of covetics should focus on improvements to the processing method. In particular, the clustering of carbon and formation of voids needs to be prevented, which motivated the updates to the covetics processing system presented in Chapter 5.

8.3. Chapter 5: Updates to the Covetics Processing System

In Chapter 5, updates to the covetics processing system and procedure were discussed. The activated carbon starting material was de-gassed in a vacuum furnace prior to processing to minimize the introduction of oxygen and other potential contaminants that could have been adsorbed on the activated carbon surface. Additionally, a new stirrer was incorporated into the processing system which is capable of achieving higher stirring speeds (up to 2000 rpm). Finally, the stirrer shaft and impeller were modified to allow Ar flow through the stirrer and into the molten aluminum-carbon mixture to attempt to minimize porosity and void content in the final covetic samples. AA-1350 3 wt% C were made using the pointed graphite electrode in the new system varying applied current, stirring speed, and Ar flow time; however, the samples made using the new system showed neither an increase in graphitic carbon crystallite size compared to the activated carbon starting material nor an increase in electrical conductivity relative to the baseline sample with no carbon added. Additionally, porosity and voids were still present in the covetic samples made using the new system.

As discussed in Section 8.1, the thermodynamics and kinetics of the solidification process could potentially be playing a role in the microstructure and properties of the final cast covetic sample. Future work could investigate the effects of solidification rate on the microstructure and properties of the covetic samples. Potentially, post-processing heat treatments could be used to minimize the void content and to improve homogeneity of the final samples. Further, it is possible that the necessary current density and/or duration of current application is not being

achieved. The design of a new system capable of applying a higher current for longer duration could potentially improve the microstructure and properties of coevitic samples.

8.4. Chapter 6: Micromechanics of an IM7/PEEK Laminate with Added Copper Mesh Layers

In Chapter 6, the micro-mechanical properties of a multifunctional composite consisting of a CFRP laminate with additional copper mesh layers were studied by nanoindentation. The sample was annealed at 200°C for 1 hour and the mechanical properties near the C fiber-PEEK matrix were studied using nanoindentation. The reduced elastic modulus and hardness were plotted as a function of distance from the fiber edge to evaluate the fiber-PEEK interfacial strength and subsequent reinforcement ability of the carbon fiber before and after annealing. It was found that the crystallinity in the PEEK matrix, estimated by Raman, was ~41% and did not change as a result of the annealing process. The hardness in the PEEK matrix increased somewhat as a result of annealing, from 0.081 +/- 0.012 GPa to 0.103 +/- 0.014 GPa ($P=0.05$). A power law fit of the reduced elastic modulus and hardness as a function of distance from the fiber edge was used to assess the interfacial adhesion and size of the interphase region between the fiber and PEEK matrix. The rate of decay of hardness with increased distance from the fiber edge decreased after annealing, indicating enhanced interfacial adhesion and a larger interphase region as a result of the annealing procedure.

The reduced elastic modulus and hardness as a function of distance from the copper edge were also evaluated and fitted to a power law function. The trend was not well described by a power law function. Rather, the histograms of reduced elastic modulus and hardness showed two discrete clusters of values, one with higher modulus/hardness corresponding to indents on copper and one with lower modulus/hardness corresponding to indents on the PEEK matrix. This indicates that there is weak interfacial adhesion between the copper and PEEK. As a result, the

copper has limited ability to act as a reinforcement phase and the indents in the PEEK matrix near the copper edge did not show an increase in modulus or hardness.

For future work, the data analysis technique could be used to study how chemical functionalization of the Cu surface during processing could promote enhanced interfacial adhesion. By increasing the interfacial shear strength, the reinforcement capability of the copper in the multifunctional composite could be enhanced, leading to improved bulk mechanical properties. Additionally, dynamic mechanical analysis (DMA) could be used to measure the complex elastic modulus of the PEEK matrix to understand how the storage modulus (real component) and loss modulus (imaginary component) change as a result of the annealing procedure, thus giving a more in-depth understanding of the elastic properties of the material.

8.5. Chapter 7: Model of Electromagnetic Interference Shielding Effectiveness for the Multifunctional Composite Containing CFRP and Copper Mesh Layers

In Chapter 7, a finite element model was made in COMSOL and used to study the EMI SE of a multifunctional composite containing unidirectional CFRP layers and copper mesh layers in the range 50 MHz to 10 GHz. The electrical properties of an individual CFRP ply with fibers oriented in one direction were represented as a tensor describing a homogeneous, anisotropic material, and lay-ups with multiple plies containing different relative fiber orientations were represented by using rotation matrices for each ply. Varying the longitudinal conductivity in the fiber direction had the highest impact on the calculated SE compared to the change in SE from varying transverse conductivity in the direction perpendicular to the fibers or varying the relative permittivity. The individual CFRP plies acted like gratings where the EM field was effectively attenuated by Ohmic loss in the direction parallel to the longitudinal fiber direction with high electrical conductivity. The SE increased for lay-ups where multiple plies with different fiber

orientations were used. The SE of the CFRP without Cu mesh was increased by increasing the thickness of each ply and by increasing the overall thickness of the laminate by adding more plies.

An analytical expression for equivalent sheet impedance was used to represent the Cu mesh and calculate its SE. The effect of using different metal materials and different mesh geometries was evaluated. For the former, metals with higher conductivity showed increased SE. Considering that the multifunctional composite could be used in aerospace applications where weight minimization is critical, the SE was normalized to metal density, and it was shown that aluminum and AA-6061 provide a balance of high conductivity and low density. The results for different Cu mesh geometries varying the mesh open area indicates that below ~ 1 MHz the choice of metal material has a more pronounced effect on SE than the choice of dimensions, but above ~ 1 MHz the choice of open mesh dimension has more of an effect than choice of material on SE.

When modeling the multifunctional composite with both CFRP and Cu mesh layers, the SE improved over a wider frequency range by including a reflection-dominant component (Cu mesh) and an absorption dominant component (the CFRP). The SE by reflection from the Cu mesh due to high electrical conductivity improved the SE at frequencies below ~ 500 MHz, whereas the SE by absorption from the CFRP layers with increased thickness improved SE at frequencies above ~ 500 MHz. The total SE of the laminate containing CFRP layers and a Cu mesh layer did not show a strong dependence on the Cu mesh placement in the lay-up.

The main limitation of the model was the use of DC conductivity values for the CFRP and Cu mesh which could affect the accuracy of the calculated SE, especially at higher frequencies. In future work, the model could be improved by using AC, frequency dependent

conductivities that account for the reduction in conductivity as frequency increases by the skin effect. Further, measurement of the complex permittivity in the frequency range of interest could improve accuracy of the model by accounting for the potential effects of molecular-level polarization in the material and interfacial polarization between the C fibers and PEEK matrix.

8.6. Publications

Details about the covetics processing and the effect of applied current and time on electrical and mechanical properties were published in⁴⁴

Ge, X., Klingshirn, C., Morales, M., Wuttig, M., Rabin, O., Zhang, S., & Salamanca-Riba, L. G. (2021). Electrical and structural characterization of nano-carbon–aluminum composites fabricated by electro-charging-assisted process. *Carbon*, *173*, 115–125. <https://doi.org/10.1016/j.carbon.2020.10.063>

which discussed how the graphitic carbon crystallite size and graphitic carbon content increased with increased reaction time due to the applied current. Additionally, electrical conductivity was correlated with the graphitic carbon crystallite size, graphitic carbon content, applied current and duration of current application. Hardness was found to be inversely correlated to porosity in the sample, and it was noted that both aluminum oxide and voids in the covetic samples were present. This work formed the basis of Chapter 3: Critical Current Density Investigation where the local current density was related to the local graphitic carbon crystallite size and electrical conductivity in different areas of the covetic sample that experienced different current densities, Chapter 4: Micromechanics of AA-1350 3 wt% C Covetics where the micro-mechanical properties of the covetics presented in Ge et al.⁴⁴ were studied using nanoindentation, and Chapter 5: Updates to the Covetics Processing System where modifications to the covetics system were built to attempt to improve homogeneity of carbon while minimizing oxide and void formation in covetic samples.

The work presented in Chapter 6: Micromechanics of an IM7/PEEK Laminate with Added Copper Mesh Layers and Chapter 7: Model of Electromagnetic Shielding Effectiveness for the Multifunctional Composite Containing CFRP and Copper Mesh Layers are both in the process of being submitted as journal papers. For Chapter 6, the corresponding journal paper will include bulk mechanical testing of the multifunctional samples to compare to the nanoindentation data.

A paper for work that was not included in this dissertation was published in¹⁷³

Henry, T. C., Morales, M. A., Cole, D. P., Shumeyko, C. M., & Riddick, J. C. (2021). Mechanical behavior of 17-4 PH stainless steel processed by atomic diffusion additive manufacturing. *International Journal of Advanced Manufacturing Technology*, 114(7–8), 2103–2114. <https://doi.org/10.1007/S00170-021-06785-1/FIGURES/13>

where nanoindentation and EBSD were used to investigate the anisotropy in microstructure and mechanical properties of stainless steel-301 samples made by an atomic diffusion additive manufactured (ADAM) process. The anisotropy was a result of extrusion in the print direction during the ADAM process.

Additionally, a work not included in this dissertation was published studying the oxidation kinetics of SiC fibers in the presence of B₂O₃ using thermogravimetric analysis (TGA) and microstructural characterization¹⁷⁴

McFarland, B., Angelici Avincola, V., Morales, M., & Opila, E. (2020). Identification of a new oxidation/ dissolution mechanism for boria-accelerated SiC oxidation. *Journal of the American Ceramic Society*, 103(9), 5214–5231. <https://doi.org/10.1111/JACE.17188>

Another paper for work not included in this dissertation is undergoing the review process for publication, with the title “Interfacial carbon fiber-matrix interactions in thermosetting composites volumetrically cured by electromagnetic fields.” In this work, nanoindentation was

used to investigate the interfacial properties of the fiber-polymer interface in CFRP samples made using different polymer curing processes.

Bibliography

1. Weiss, N. O. *et al.* Graphene: An emerging electronic material. *Advanced Materials* vol. 24 5782–5825 Preprint at <https://doi.org/10.1002/adma.201201482> (2012).
2. Morozov, S. V *et al.* Giant intrinsic carrier mobilities in graphene and its bilayer. *Phys Rev Lett* **100**, (2008).
3. Chen, J. H., Jang, C., Xiao, S., Ishigami, M. & Fuhrer, M. S. Intrinsic and extrinsic performance limits of graphene devices on SiO₂. *Nat Nanotechnol* **3**, 206–209 (2008).
4. Lee, C., Wei, X., Kysar, J. W. & Hone, J. Measurement of the elastic properties and intrinsic strength of monolayer graphene. *Science (1979)* **321**, 385–388 (2008).
5. Popov, V. N. Carbon nanotubes: Properties and application. *Materials Science and Engineering R: Reports* vol. 43 61–102 Preprint at <https://doi.org/10.1016/j.mser.2003.10.001> (2004).
6. Nieto, A., Bisht, A., Lahiri, D., Zhang, C. & Agarwal, A. Graphene reinforced metal and ceramic matrix composites: a review. *International Materials Reviews* vol. 62 241–302 Preprint at <https://doi.org/10.1080/09506608.2016.1219481> (2017).
7. Tehrani, M. Advanced Electrical Conductors: An Overview and Prospects of Metal Nanocomposite and Nanocarbon Based Conductors. *Physica Status Solidi (A) Applications and Materials Science* **218**, (2021).
8. Forrest, D. R., Brown, C. L., Wolk, J., Joyce, P. & Zhang, J. Nanoscale Carbon in Metals for Energy Applications. in *MS&T 2011* (2011).
9. Cao, M. *et al.* Ultrahigh Electrical Conductivity of Graphene Embedded in Metals. *Adv Funct Mater* **29**, 1806792 (2019).
10. Su, X. F., Chen, H. R., Kennedy, D. & Williams, F. W. Effects of interphase strength on the damage modes and mechanical behaviour of metal-matrix composites. *Compos Part A Appl Sci Manuf* **30**, 257–266 (1999).
11. Yang, M., Liu, Y., Fan, T. & Zhang, D. Metal-graphene interfaces in epitaxial and bulk systems: A review. *Prog Mater Sci* **110**, 100652 (2020).
12. Young, R. J., Kinloch, I. A., Gong, L. & Novoselov, K. S. The mechanics of graphene nanocomposites: A review. (2012) doi:10.1016/j.compscitech.2012.05.005.
13. Mohan, V. B., Lau, K.-T., Hui, D. & Bhattacharyya, D. Graphene-based materials and their composites: A review on production, applications and product limitations. (2018) doi:10.1016/j.compositesb.2018.01.013.
14. Li, J. L. *et al.* Microstructure and tensile properties of bulk nanostructured aluminum/graphene composites prepared via cryomilling. *Materials Science and Engineering A* **626**, 400–405 (2015).
15. Li, G. & Xiong, B. Effects of graphene content on microstructures and tensile property of graphene-nanosheets / aluminum composites. *J Alloys Compd* **697**, 31–36 (2017).
16. Dutkiewicz, J. *et al.* Microstructure and properties of bulk copper matrix composites strengthened with various kinds of graphene nanoplatelets. doi:10.1016/j.msea.2015.01.018.
17. Laha, T., Agarwal, A., McKechnie, T. & Seal, S. Synthesis and characterization of plasma spray formed carbon nanotube reinforced aluminum composite. *Materials Science and Engineering A* **381**, 249–258 (2004).

18. Bartolucci, S. F. *et al.* Graphene-aluminum nanocomposites. *Materials Science and Engineering A* **528**, 7933–7937 (2011).
19. Chen, B. *et al.* Solid-state interfacial reaction and load transfer efficiency in carbon nanotubes (CNTs)-reinforced aluminum matrix composites. *Carbon N Y* **114**, 198–208 (2017).
20. Laha, T., Kuchibhatla, S., Seal, S., Li, W. & Agarwal, A. Interfacial phenomena in thermally sprayed multiwalled carbon nanotube reinforced aluminum nanocomposite. *Acta Mater* **55**, 1059–1066 (2007).
21. Zhou, W. *et al.* In situ formation of uniformly dispersed Al₄C₃ nanorods during additive manufacturing of graphene oxide/Al mixed powders. *Carbon N Y* **141**, 67–75 (2019).
22. Yu, Z. *et al.* Effect of ball milling time on graphene nanosheets reinforced Al6063 composite fabricated by pressure infiltration method. *Carbon N Y* **141**, 25–39 (2019).
23. Shin, S. E., Ko, Y. J. & Bae, D. H. Mechanical and thermal properties of nanocarbon-reinforced aluminum matrix composites at elevated temperatures. *Compos B Eng* **106**, 66–73 (2016).
24. Kwon, H., Estili, M., Takagi, K., Miyazaki, T. & Kawasaki, A. Combination of hot extrusion and spark plasma sintering for producing carbon nanotube reinforced aluminum matrix composites. *Carbon N Y* **47**, 570–577 (2009).
25. Arnaud, C. *et al.* High strength - High conductivity double-walled carbon nanotube - Copper composite wires. *Carbon* vol. 96 212–215 Preprint at <https://doi.org/10.1016/j.carbon.2015.09.061> (2016).
26. Shugart, J. v. & Scherer, R. C. Copper-Carbon Composition. (2010).
27. Shugart, J. v. & Scherer, R. C. Metal-Carbon Compositions. (2013) doi:10.1103/physics.2.30.
28. Bakir, M. & Jasiuk, I. Novel Metal-Carbon Nanomaterials: A Review On Covetics. *Adv Mater Lett* **8**, 884–890 (2017).
29. Jaim, H. M. I. *et al.* Sp² carbon embedded in Al-6061 and Al-7075 alloys in the form of crystalline graphene nanoribbons. *Carbon N Y* **107**, 56–66 (2016).
30. Salamanca-Riba, L. G. *et al.* Synthetic Crystals of Silver with Carbon: 3D Epitaxy of Carbon Nanostructures in the Silver Lattice. *Adv Funct Mater* **25**, 4768–4777 (2015).
31. Brown, L., Joyce, P., Forrest, D. & Wolk, J. Physical and mechanical characterization of a nano carbon infused aluminum-matrix composite. *International SAMPE Technical Conference* **3**, (2011).
32. Scherer, R., Shugart, J. & Lafdi, K. New class of metallic nanocomposites - NanoCarbon metals. in *MS&T 2009* vol. 3 1828–1835 (2009).
33. Lathabai, S. Additive Manufacturing of Aluminium-Based Alloys and Composites. in *Fundamentals of Aluminium Metallurgy* 47–92 (Woodhead Publishing, 2018). doi:10.1016/b978-0-08-102063-0.00002-3.
34. Salamanca-Riba, L. *Advances in Nanocarbon Metals : Fine Structure*. ARL-CR-0763 (2015).
35. Knych, T. *et al.* Characterization of nanocarbon copper composites manufactured in metallurgical synthesis process. *Metallurgical and Materials Transactions B: Process Metallurgy and Materials Processing Science* **45**, 1196–1203 (2014).
36. Knych, T. *et al.* Fabrication and cold drawing of copper Covetic nanostructured carbon composites. *Archives of Metallurgy and Materials* **59**, 1283–1286 (2014).

37. Isaacs, R. A. *et al.* Synthesis and characterization of copper-nanocarbon films with enhanced stability. *Carbon N Y* **122**, 336–343 (2017).
38. Isaacs, R. A. *et al.* Nanocarbon-copper thin film as transparent electrode. *Appl Phys Lett* **106**, 193108 (2015).
39. Ma, B., Balachandran, U., Dorris, S. E., Lee, T. H. & Rondinone, A. J. Preparation and electrical conductivity of graphitic carbon-infused copper alloys. *MRS Commun* **9**, 137–143 (2019).
40. Ma, B. *et al.* Structural hierarchy of nanocarbon in copper covectics. *Appl Phys Lett* **113**, 173102 (2018).
41. Ge, X. *et al.* Mechanism studies and fabrication for the incorporation of carbon into Al alloys by the electro-charging assisted process. *Carbon N Y* **149**, 203–212 (2019).
42. Dutkiewicz, J. *et al.* Microstructure and properties of bulk copper matrix composites strengthened with various kinds of graphene nanoplatelets. *Materials Science and Engineering A* **628**, 124–134 (2015).
43. Shumeyko, C. M., Ge, X., Klingshirn, C. J., Salamanca-Riba, L. & Cole, D. P. Tunable mechanical behavior of graphene nanoribbon-metal composites fabricated through an electrocharge-assisted process. *Materials Science and Engineering A* **800**, (2021).
44. Ge, X. *et al.* Electrical and structural characterization of nano-carbon–aluminum composites fabricated by electro-charging-assisted process. *Carbon N Y* **173**, 115–125 (2021).
45. Gibson, R. F. A review of recent research on mechanics of multifunctional composite materials and structures. (2010) doi:10.1016/j.compstruct.2010.05.003.
46. Gibson, R. F. *Principles of Composite Materials Mechanics*. (Taylor & Francis Group, 2016).
47. Sun, L., Gibson, R. F., Gordaninejad, F. & Suhr, J. Energy absorption capability of nanocomposites: A review. (2009) doi:10.1016/j.compscitech.2009.06.020.
48. Forintos, N. & Czigany, T. Multifunctional application of carbon fiber reinforced polymer composites: Electrical properties of the reinforcing carbon fibers-A short review. (2018) doi:10.1016/j.compositesb.2018.10.098.
49. Huang, Y., Chen, J., Fan, Q., Chen, M. & Fang, D. Multifunctional carbon fiber reinforced multilayered metastructure with broadband microwave absorption and effective mechanical resistance. *Polym Compos* **42**, 1846–1854 (2021).
50. Micheli, D. *et al.* Ballistic and electromagnetic shielding behaviour of multifunctional Kevlar fiber reinforced epoxy composites modified by carbon nanotubes. (2016) doi:10.1016/j.carbon.2016.03.059.
51. Pattarakunnan, K., Galos, J., Das, R. & Mouritz, A. P. Tensile properties of multifunctional composites embedded with lithium-ion polymer batteries. (2020) doi:10.1016/j.compositesa.2020.105966.
52. Narayana, J. & Gupta Burela, R. A review of recent research on multifunctional composite materials and structures with their applications. *Mater Today Proc* **5**, 5580–5590 (2018).
53. Xiao, Y., Qiao, W., Fukuda, H. & Hatta, H. The effect of embedded devices on structural integrity of composite laminates. (2016) doi:10.1016/j.compstruct.2016.06.007.
54. Schelkunoff, S. A. Transmission theory of plane electromagnetic waves. *Proceedings of the Institute of Radio Engineers* **25**, 1457–1492 (1937).

55. Ott, H. W. Shielding. in *Electromagnetic Compatibility Engineering* 238–297 (John Wiley & Sons, 2009).
56. Munalli, D., Dimitrakis, G., Chronopoulos, D., Greedy, S. & Long, A. Electromagnetic shielding effectiveness of carbon fibre reinforced composites. *Compos B Eng* **173**, (2019).
57. Mikinka, E. & Siwak, M. Recent advances in electromagnetic interference shielding properties of carbon-fibre-reinforced polymer composites—a topical review. *Journal of Materials Science: Materials in Electronics* vol. 32 24585–24643 Preprint at <https://doi.org/10.1007/s10854-021-06900-8> (2021).
58. Kraus, J. D. & Fleisch, D. A. Wave Propagation, Attenuation, Polarization, Reflection, Refraction, and Diffraction. in *Electromagnetics with Applications* 169–239 (McGraw-Hill, 1999).
59. Steer, M. *Microwave and RF Design II- Transmission Lines*. vol. 2 (2019).
60. Neruda, M. & Vojtech, L. Electromagnetic Shielding Effectiveness of Woven Fabrics with High Electrical Conductivity: Complete Derivation and Verification of Analytical Model. *Materials* 2018, Vol. 11, Page 1657 **11**, 1657 (2018).
61. Hexcel Corporation. *HexTow® IM7 Carbon Fiber Product Data Sheet*. <http://www.hexcel.com/contact> (2020).
62. Luo, X. & Chung, D. D. L. Electromagnetic interference shielding using continuous carbon-fiber carbon-matrix and polymer-matrix composites. *Compos B Eng* **30**, 227–231 (1999).
63. United States National Bureau of Standards. *IACS Copper*. (1914).
64. Wang, M. *et al.* Construction, mechanism and prospective of conductive polymer composites with multiple interfaces for electromagnetic interference shielding: A review. *Carbon N Y* **177**, 377–402 (2021).
65. Saini, P., Choudhary, V., Singh, B. P., Mathur, R. B. & Dhawan, S. K. Polyaniline–MWCNT nanocomposites for microwave absorption and EMI shielding. *Mater Chem Phys* **113**, 919–926 (2009).
66. Jana, P. B., Mallick, A. K. & De, S. K. Effects of sample thickness and fiber aspect ratio on EMI shielding effectiveness of carbon fiber filled polychloroprene composites in the X-band frequency range. *IEEE Trans Electromagn Compat* **34**, 478–481 (1992).
67. Qin, F. & Brosseau, C. A review and analysis of microwave absorption in polymer composites filled with carbonaceous particles. *J Appl Phys* **111**, 061301 (2012).
68. Biswas, S., Arief, I., Panja, S. S. & Bose, S. Absorption-dominated electromagnetic wave suppressor derived from ferrite-doped cross-linked graphene framework and conducting carbon. *ACS Appl Mater Interfaces* **9**, 3030–3039 (2017).
69. Liu, W., Tan, S., Yang, Z. & Ji, G. Enhanced Low-Frequency Electromagnetic Properties of MOF-Derived Cobalt through Interface Design. (2018) doi:10.1021/acsami.8b10685.
70. Jang, D., Choi, B. H., Yoon, H. N., Yang, B. & Lee, H. K. Improved electromagnetic wave shielding capability of carbonyl iron powder-embedded lightweight CFRP composites. *Compos Struct* 115326 (2022) doi:10.1016/j.compstruct.2022.115326.
71. D’Amore, M. & Sarto, M. S. Theoretical and experimental characterization of the EMP-interaction with composite-metallic enclosures. *IEEE Trans Electromagn Compat* **42**, 152–163 (2000).

72. Rajesh, P. S. M., Sirois, F. & Therriault, D. Damage response of composites coated with conducting materials subjected to emulated lightning strikes. *Mater Des* **139**, 45–55 (2018).
73. Jung, S. & Cho, D. Effect of fiber feeding route upon extrusion process on the electromagnetic, mechanical, and thermal properties of nickel-coated carbon fiber/polypropylene composites. *Compos B Eng* **187**, (2020).
74. Huang, C. Y. & Wu, C. C. EMI shielding effectiveness of PC/ABS/nickel-coated-carbon-fibre composites. *Eur Polym J* **36**, 2729–2737 (2000).
75. Guan, H. & Chung, D. D. L. Effect of the planar coil and linear arrangements of continuous carbon fiber tow on the electromagnetic interference shielding effectiveness, with comparison of carbon fibers with and without nickel coating. *Carbon N Y* **152**, 898–908 (2019).
76. Tugirumubano, A., Vijay, S. J., Go, S. H., Kwac, L. K. & Kim, H. G. Investigation of Mechanical and Electromagnetic Interference Shielding Properties of Nickel–CFRP Textile Composites. *J Mater Eng Perform* **27**, 2255–2262 (2018).
77. Zhu, H., Fu, K., Yang, B. & Li, Y. Nickel-coated nylon sandwich film for combination of lightning strike protection and electromagnetic interference shielding of CFRP composite. *Compos Sci Technol* **207**, 108675 (2021).
78. Shui, X. & Chung, D. D. L. Submicron diameter nickel filaments and their polymer-matrix composites. *J Mater Sci* **35**, 1773–1785 (2000).
79. Chung, D. D. L. Electromagnetic interference shielding effectiveness of carbon materials. *Carbon N Y* **39**, 279–285 (2001).
80. Wang, Y. & Jing, X. Intrinsically conducting polymers for electromagnetic interference shielding. *Polym Adv Technol* **16**, 344–351 (2005).
81. Zhao, Z. J. *et al.* MWCNT modified structure-conductive composite and its electromagnetic shielding behavior. *Compos B Eng* **130**, 21–27 (2017).
82. Gong, S. *et al.* Effect of carbon nanotubes on electromagnetic interference shielding of carbon fiber reinforced polymer composites. *Polym Compos* **39**, E655–E663 (2018).
83. Song, W. L. *et al.* Flexible graphene/polymer composite films in sandwich structures for effective electromagnetic interference shielding. *Carbon N Y* **66**, 67–76 (2014).
84. Dhakate, S. R., Subhedar, K. M. & Singh, B. P. Polymer nanocomposite foam filled with carbon nanomaterials as an efficient electromagnetic interference shielding material. *RSC Advances* vol. 5 43036–43057 Preprint at <https://doi.org/10.1039/c5ra03409d> (2015).
85. Khodadadi Yazdi, M., Noorbakhsh, B., Nazari, B. & Ranjbar, Z. Preparation and EMI shielding performance of epoxy/non-metallic conductive fillers nano-composites. *Prog Org Coat* **145**, 105674 (2020).
86. Yang, S., Lozano, K., Lomeli, A., Foltz, H. D. & Jones, R. Electromagnetic interference shielding effectiveness of carbon nanofiber/LCP composites. *Compos Part A Appl Sci Manuf* **36**, 691–697 (2005).
87. Duan, H. *et al.* Effect of carbon nanofiller dimension on synergistic EMI shielding network of epoxy/metal conductive foams. *Compos Part A Appl Sci Manuf* **118**, 41–48 (2019).
88. Rohini, R. & Bose, S. Electromagnetic interference shielding materials derived from gelation of multiwall carbon nanotubes in polystyrene/poly(methyl methacrylate) blends. *ACS Appl Mater Interfaces* **6**, 11302–11310 (2014).

89. Chen, M. *et al.* Electromagnetic interference shielding properties of silicon nitride ceramics reinforced by in situ grown carbon nanotubes. *Ceram Int* **41**, 2467–2475 (2015).
90. Hong, J., Xu, P., Xia, H., Xu, Z. & Ni, Q. Q. Electromagnetic interference shielding anisotropy enhanced by CFRP laminated structures. *Compos Sci Technol* **203**, 108616 (2021).
91. Fouladgar, J., Wasselynck, G. & Trichet, D. Shielding and Reflecting Effectiveness of Carbon Fiber Reinforced Polymer (CFRP) composites. *2013 International Symposium on Electromagnetic Theory, EMTS 2013 - Proceedings* 104–107 (2013).
92. Louis, M., Joshi, S. P. & Brockmann, W. An experimental investigation of through-thickness electrical resistivity of CFRP laminates. *Compos Sci Technol* **61**, 911–919 (2001).
93. Wang, Q., Zhou, H., Liu, M., Li, X. & Hu, Q. Study of the skin depth and defect detection in carbon fiber composites with Terahertz waves. *Optik (Stuttg)* **178**, 1035–1044 (2019).
94. Holloway, C. L., Sarto, M. S. & Johansson, M. Analyzing carbon-fiber composite materials with equivalent-layer models. *IEEE Trans Electromagn Compat* **47**, 833–844 (2005).
95. Lee, S.-E., Park, K.-Y., Oh, K.-S. & Kim, C.-G. The use of carbon/dielectric fiber woven fabrics as filters for electromagnetic radiation. (2009) doi:10.1016/j.carbon.2009.02.013.
96. Casey, K. F. Electromagnetic Shielding Behavior of Wire-Mesh Screens. *IEEE Trans Electromagn Compat* **30**, 298–306 (1988).
97. Wang, Z., Liu, X., Zhang, J. & Bian, X. Study of the reaction mechanism in the Al-C binary system through DSC and XRD.
98. Fischer-Cripps, A. C. *Nanoindentation*. (Springer, 2004).
99. Tuinstra, F. & Koenig, J. Raman Spectrum of Graphine. *Journal of Chemical Physics* **53**, 1126–1130 (1970).
100. Ferrari, A. C. Raman spectroscopy of graphene and graphite: Disorder, electron-phonon coupling, doping and nonadiabatic effects. *Solid State Commun* **143**, 47–57 (2007).
101. Ferrari, A. C. & Robertson, J. Interpretation of Raman spectra of disordered and amorphous carbon.
102. Cañado, L. G. *et al.* General equation for the determination of the crystallite size l_a of nanographite by Raman spectroscopy. *Appl Phys Lett* **88**, 163106 (2006).
103. O’Haver, T. C. peakfit.m. Preprint at (2021).
104. Turkevich, V., Garan, A., Kulik, O. & Petrusha, I. Phase Diagram and Diamond Synthesis in the Aluminum—Carbon System at a Pressure of 8 GPa. *Innovative Superhard Materials and Sustainable Coatings for Advanced Manufacturing* 335–343 (2005) doi:10.1007/1-4020-3471-7_26.
105. Smallman, R. E. & Ngan, A. H. W. Modern Physical Metallurgy: Eighth Edition. in *Modern Physical Metallurgy: Eighth Edition* 93–119 (2013). doi:10.1016/C2011-0-05565-5.
106. Welch, B. *Light Metals. Light Metals 2016* (Wiley, 2016). doi:10.1002/9781119274780.
107. David, M. & Connétable, D. Diffusion of interstitials in metallic systems, illustration of a complex study case: aluminum. *Journal of Physics: Condensed Matter* **29**, 455703 (2017).
108. Hofmann, S. & Lej, P. Solute Segregation at Grain Boundaries. *INTERFACE SCIENCE* **3**, 241–267 (1996).

109. Groover, M. P. *Fundamentals of Modern Manufacturing: Materials, Processes, and Systems, Enhanced eText, 7th Edition* | Wiley. 816 (2019).
110. Bier, M. *Electrophoresis: Theory, Methods, and Applications*. vol. 2 (Academic Press, 1967).
111. Turcu, I. & Lucaciu, C. M. Dielectrophoresis: a spherical shell model. *J Phys A Math Gen* **22**, 985–993 (1989).
112. Lumsdon, S. O. & Scott, D. M. Assembly of colloidal particles into microwires using an alternating electric field. *Langmuir* **21**, 4874–4880 (2005).
113. Gierhart, B. C., Howitt, D. G., Chen, S. J., Smith, R. L. & Collins, S. D. Frequency dependence of gold nanoparticle superassembly by dielectrophoresis. *Langmuir* **23**, 12450–12456 (2007).
114. Hermanson, K. D., Lumsdon, S. O., Williams, J. P., Kaler, E. W. & Velev, O. D. Dielectrophoretic assembly of electrically functional microwires from nanoparticle suspensions. *Science (1979)* **294**, 1082–1086 (2001).
115. Parthasarathy, M. & Klingenberg, D. J. Electrorheology: mechanisms and models. *Materials Science and Engineering* **7**, 57–103 (1996).
116. Oliveira, L. *et al.* *Directed-assembly of carbon structures in a nonpolar dielectric liquid under the influence of DC-generated electric fields*. <http://www.elsevier.com/open-access/userlicense/1.0/> (2015).
117. Davis, J. R. Alloying: Understanding the Basics. in 351–416 (ASM International, 2001). doi:10.1361/autb2001p351.
118. Varnell, J. A. *et al.* Understanding the influence of carbon addition on the corrosion behavior and mechanical properties of Al alloy “covetics”. *J Mater Sci* **54**, 2668–2679 (2019).
119. Gouldstone, A. *et al.* Indentation across size scales and disciplines: Recent developments in experimentation and modeling. *Acta Mater* **55**, 4015–4039 (2007).
120. Oliver, W. C. & Pharr, G. M. An improved technique for determining hardness and elastic modulus using load and displacement sensing indentation experiments. *J Mater Res* **7**, 1564–1583 (1992).
121. Oliver, W. C. & Pharr, G. M. Measurement of hardness and elastic modulus by instrumented indentation: Advances in understanding and refinements to methodology. *J Mater Res* **19**, 3–20 (2004).
122. Telling, R. H. & Heggie, M. I. Stacking fault and dislocation glide on the basal plane of graphite. <https://doi-org.proxy-um.researchport.umd.edu/10.1080/0950083031000137839> **83**, 411–421 (2010).
123. Koumoulos, E., Konstantopoulos, G. & Charitidis, C. Applying machine learning to nanoindentation data of (nano-) enhanced composites. *Fibers* **8**, 3 (2020).
124. Konstantopoulos, G., Koumoulos, E. P. & Charitidis, C. A. Classification of mechanism of reinforcement in the fiber-matrix interface: Application of Machine Learning on nanoindentation data. *Mater Des* **192**, (2020).
125. Bansal, R. C. & Goyal, M. Activated Carbon Adsorption. in 1–60 (2005).
126. Puga, H., Barbosa, J., Seabra, E., Ribeiro, S. & Prokic, M. New Trends in Aluminium Degassing-A Comparative Study. in *Fourth International Conference on Advances and Trends in Engineering Materials and Their Applications* (2009).

127. Gibson, R. F. A review of recent research on nanoindentation of polymer composites and their constituents. (2014) doi:10.1016/j.compscitech.2014.09.016.
128. DiFrancia, C., Ward, T. C. & Claus, R. O. The single-fibre pull-out test. 1: Review and interpretation. *Compos Part A Appl Sci Manuf* **27**, 597–612 (1996).
129. Cole, D. P., Henry, T. C., Gardea, F. & Haynes, R. A. Interphase mechanical behavior of carbon fiber reinforced polymer exposed to cyclic loading. *Compos Sci Technol* **151**, 202–210 (2017).
130. Konstantopoulos, G., Semitekolos, D., Koumoulos, E. P. & Charitidis, C. Carbon fiber reinforced composites: Study of modification effect on weathering-induced ageing via nanoindentation and deep learning. *Nanomaterials* **11**, 2631 (2021).
131. Gu, Y., Li, M., Wang, J. & Zhang, Z. Characterization of the interphase in carbon fiber/polymer composites using a nanoscale dynamic mechanical imaging technique. (2010) doi:10.1016/j.carbon.2010.05.008.
132. Niu, Y. F., Yang, Y. & Wang, X. R. Investigation of the interphase structures and properties of carbon fiber reinforced polymer composites exposed to hydrothermal treatments using peak force quantitative nanomechanics technique. *Polym Compos* **39**, E791–E796 (2018).
133. Ureñ, A., Rams, J. & Sánchez, M. Characterization of interfacial mechanical properties in carbon fiber/aluminium matrix composites by the nanoindentation technique. *Compos Sci Technol* (2005) doi:10.1016/j.compscitech.2005.04.013.
134. Zhu, J., Lang, F. C., Wang, S. Y., Li, Z. & Xing, Y. M. Determination of the interfacial properties of carbon fiber reinforced polymers using nanoindentation. *Journal of Reinforced Plastics and Composites* **41**, 509–516 (2022).
135. Kavouras, P., Dragatogiannis, D. A., Batsouli, D. I. & Charitidis, C. A. Effect of local microstructure on the indentation induced damage of a fiber reinforced composite. (2017) doi:10.1016/j.polymertesting.2017.05.023.
136. Malito, L. G. *et al.* Material properties of ultra-high molecular weight polyethylene: Comparison of tension, compression, nanomechanics and microstructure across clinical formulations. *J Mech Behav Biomed Mater* **83**, 9–19 (2018).
137. Rae, P. J., Brown, E. N. & Orler, E. B. The mechanical properties of poly(ether-etherketone) (PEEK) with emphasis on the large compressive strain response. *Polymer (Guildf)* **48**, 598–615 (2007).
138. Sarasua, J. R., Remiro, P. M. & Pouyet, J. Effects of thermal history on mechanical behavior of PEEK and its short-fiber composites. *Polym Compos* **17**, 468–477 (1996).
139. Arevalo, S. E. & Pruitt, L. A. Nanomechanical analysis of medical grade PEEK and carbon fiber-reinforced PEEK composites. *J Mech Behav Biomed Mater* **111**, (2020).
140. Khan, A. A., Al-Kheraif, A. A., Al-Shehri, A. M., Säilynoja, E. & Vallittu, P. K. Polymer matrix of fiber-reinforced composites: Changes in the semi-interpenetrating polymer network during the shelf life. *J Mech Behav Biomed Mater* **78**, 414–419 (2018).
141. Godara, A., Raabe, D. & Green, S. The influence of sterilization processes on the micromechanical properties of carbon fiber-reinforced PEEK composites for bone implant applications. *Acta Biomater* **3**, 209–220 (2007).
142. Regis, M., Zanetti, M., Pressacco, M. & Bracco, P. Opposite role of different carbon fiber reinforcements on the non-isothermal crystallization behavior of poly(etheretherketone). *Mater Chem Phys* **179**, 223–231 (2016).

143. Yang, C. *et al.* Influence of thermal processing conditions in 3D printing on the crystallinity and mechanical properties of PEEK material. *J Mater Process Technol* **248**, 1–7 (2017).
144. Doumeng, M. *et al.* A comparative study of the crystallinity of polyetheretherketone by using density, DSC, XRD, and Raman spectroscopy techniques. *Polym Test* **93**, 106878 (2021).
145. Jin, L., Ball, J., Bremner, T. & Sue, H. J. Crystallization behavior and morphological characterization of poly(ether ether ketone). *Polymer (Guildf)* **55**, 5255–5265 (2014).
146. Voyiadjis, G. Z. & Malekmotiei, L. Variation of the strain rate during CSM nanoindentation of glassy polymers and its implication on indentation size effect. *J Polym Sci B Polym Phys* **54**, 2179–2187 (2016).
147. Iqbal, T., Briscoe, B. J., Yasin, S. & Luckham, P. F. Nanoindentation response of poly(ether ether ketone) surfaces—A semicrystalline bimodal behavior. *J Appl Polym Sci* **130**, 4401–4409 (2013).
148. Kim, S., Lee, K. J. & Seo, Y. Polyetheretherketone (PEEK) Surface Functionalization by Low-Energy Ion-Beam Irradiation under a Reactive O₂ Environment and Its Effect on the PEEK/Copper Adhesives. *Langmuir* **20**, 157–163 (2004).
149. Koledintseva, M. Y., Drewniak, J., DuBroff, R., Rozanov, K. & Archambeault, B. Modeling of Shielding Composite Materials and Structures for Microwave Frequencies. *Progress In Electromagnetics Research B* **15**, 197–215 (2009).
150. Šafářová, V., Tunák, M. & Militký, J. Prediction of hybrid woven fabric electromagnetic shielding effectiveness: <https://doi.org/10.1177/0040517514555802> **85**, 673–686 (2014).
151. Rea, S., Linton, D., Orr, E. & McConnell, J. Electromagnetic Shielding Properties of Carbon Fibre Composites in Avionic Systems. (2005).
152. Jou, W. S. A novel structure of woven continuous-carbon fiber composites with high electromagnetic shielding. *Journal of Electronic Materials* **2004 33:3** **33**, 162–170 (2004).
153. Greco, S., Tamburrano, A., D’Aloia, A., Mufatti, R. & Sarto, M. S. Shielding effectiveness properties of carbon-fiber reinforced composite for HIRF applications. *IEEE International Symposium on Electromagnetic Compatibility* (2012) doi:10.1109/EMCEUROPE.2012.6396702.
154. Lin, M. S. & Chen, C. H. Plane-Wave Shielding Characteristics of Anisotropic Laminated Composites. *IEEE Trans Electromagn Compat* **35**, 21–27 (1993).
155. COMSOL. *RF Module User’s Guide*. www.comsol.com/blogs (2017).
156. Jin, J. Basic Electromagnetic Theory. in *The Finite Element Method in Electromagnetics* 1–17 (John Wiley & Sons, 2002).
157. Zhao, Q. *et al.* Review on the electrical resistance/conductivity of carbon fiber reinforced polymer. *Applied Sciences* **9**, (2019).
158. Wasselynck, G., Trichet, D. & Fouladgar, J. Determination of the electrical conductivity tensor of a CFRP composite using a 3-D percolation model. *IEEE Trans Magn* **49**, 1825–1828 (2013).
159. Todoroki, A., Tanaka, M. & Shimamura, Y. Measurement of orthotropic electric conductance of CFRP laminates and analysis of the effect on delamination monitoring with an electric resistance change method. *Compos Sci Technol* **62**, 619–628 (2002).

160. Haider, M. F., Majumdar, P. K., Angeloni, S. & Reifsnider, K. L. Nonlinear anisotropic electrical response of carbon fiber-reinforced polymer composites. *J Compos Mater* **52**, 1017–1032 (2018).
161. Pratap, S. B. & Weldon, W. F. Eddy currents in anisotropic composites applied to pulsed machinery. *IEEE Trans Magn* **32**, 437–444 (1996).
162. Todoroki, A. & Yoshida, J. Electrical resistance change of unidirectional CFRP due to applied load. *JSME International Journal, Series A: Solid Mechanics and Material Engineering* **47**, 357–364 (2004).
163. Wasselynck, G., Trichet, D., Ramdane, B. & Fouldagar, J. Microscopic and macroscopic electromagnetic and thermal modeling of carbon fiber reinforced polymer composites. in *IEEE Transactions on Magnetics* vol. 47 1114–1117 (2011).
164. Wasselynck, G., Trichet, D., Ramdane, B. & Fouldagar, J. Interaction between electromagnetic field and CFRP materials: A new multiscale homogenization approach. in *IEEE Transactions on Magnetics* vol. 46 3277–3280 (2010).
165. Bui, H. K. *et al.* Characterization of Electrical Conductivity of Anisotropic CFRP Materials by Means of Induction Thermography Technique. *IEEE Trans Magn* **54**, (2018).
166. ThePlasticShop. Peek 1000 Technical Properties Data Sheet. **4300**, 4300.
167. Casey, K. F. Electromagnetic Shielding Behavior of Wire-Mesh Screens. *IEEE Trans Electromagn Compat* **30**, 298–306 (1988).
168. Bozzetti, M., Pisu, L., Sarto, M. S. & Greco, S. *Shielding Performance of an Expanded Copper Foil over a Wide Frequency Range*. (2011).
169. Dharma Raj, C., Ramyasree, M. V. S. L. & Sravan Kumar, V. Analysis of wire mesh screen for shielding effectiveness in different frequency ranges. *2011 International Conference on Computer, Communication and Electrical Technology, ICCET 2011* 198–203 (2011) doi:10.1109/ICCET.2011.5762467.
170. Kim, H. C. & See, S. K. Electrical properties of unidirectional carbon-epoxy composites in wide frequency band. *Journal of Physics D: Applied Physics J. Phys. D: Appl. Phys* **23**, 916–921 (1990).
171. Cheng, J. *et al.* Application of low frequency ECT method in noncontact detection and visualization of CFRP material. *Compos B Eng* **110**, 141–152 (2017).
172. Hirano, Y., Yamane, T. & Todoroki, A. Through-thickness electric conductivity of toughened carbon-fibre-reinforced polymer laminates with resin-rich layers. *Compos Sci Technol* **122**, 67–72 (2016).
173. Henry, T. C., Morales, M. A., Cole, D. P., Shumeyko, C. M. & Riddick, J. C. Mechanical behavior of 17-4 PH stainless steel processed by atomic diffusion additive manufacturing. *International Journal of Advanced Manufacturing Technology* **114**, 2103–2114 (2021).
174. McFarland, B., Angelici Avincola, V., Morales, M. & Opila, E. Identification of a new oxidation/ dissolution mechanism for boron-accelerated SiC oxidation. *Journal of the American Ceramic Society* **103**, 5214–5231 (2020).